Development of Analytical Models for Evaluating the Mechanical and Electrochemical Response of Flexible and Stretchable Lithium Ion Battery Materials

A Dissertation

Presented to

the Faculty of the Materials Science and Engineering Program

University of Houston

In Partial Fulfillment

of the Requirements for the Degree

Doctor of Philosophy

in Materials Science and Engineering

by

Sean Berg

December 2016

Development of Analytical Models for Evaluating the Mechanical and Electrochemical Response of Flexible and Stretchable Lithium Ion Battery Materials

_____

Sean Berg

Approved:

_____

Chair of the Committee
Haleh Ardebili, Associate Professor,
Mechanical Engineering

Committee Members:

_____

Jae-Hyun Ryou, Assistant Professor,
Mechanical Engineering

_____

Cunjiang Yu, Assistant Professor,
Mechanical Engineering

_____

Pradeep Sharma, Professor,
Mechanical Engineering

_____

Yashashree Kulkarni, Associate Professor,
Mechanical Engineering

_____

Suresh K. Khator, Associate Dean,
Cullen College of Engineering

_____

Pradeep Sharma, Professor and Director
of the Materials Science and Engineering
Program

Acknowledgements

There are many people I would like to thank and acknowledge for their involvement and support while completing my doctoral degree at the University of Houston. This has been a personal dream of mine for many years, and it has been a challenging endeavor, but their intellectual contributions, and financial and emotional support have kept me going, and helped to make this possible.

I would like to thank my doctoral research advisor, Dr. Haleh Ardebili, for supporting my research efforts, and for guiding me down a path to completing my degree in a timely manner. She has been especially understanding and patient of the fact that I have been employed full-time as a mechanical/materials engineer while pursuing this degree, which has made this especially difficult. I am appreciative of the fact that she helped me select a research topic and continuously develop it to result in the body of work presented in this dissertation. As someone who has a background in Oil & Gas, she introduced me to a new and exciting area, which I believe will play a big role in the future of energy. While I was initially trying to figure out what I could pursue in this area, she helped me utilize my strengths in analytical and numerical work to make important research contributions. Having pursued this area of research, I now have a new interest in continuing research in this field beyond the doctoral degree, and I am hopeful that it will become a new career path for me. For that, I am very thankful to her.

I would next like to thank my committee members, Dr. Jae-Hyun Ryou, Dr. Yashashree Kulkarni, Dr. Cunjiang Yu, and Dr. Pradeep Sharma, for their time and participation in my committee, and for their review of my dissertation. I greatly appreciate all of the comments, critiques, and constructive criticisms of my work, which helped me to produce this dissertation.

I would also like to thank the faculty with whom I took courses, including Dr. Haleh Ardebili, Dr. Li Sun, Dr. Yashashree Kulkarni, Dr. Gila Stein, and Dr. Pradeep Sharma. I am especially thankful to Dr. Pradeep Sharma for introducing me to new analytical methods and techniques that were very insightful and that helped me to further my research, particularly in the development of mathematical and physical materials models.

I would also like to thank the members of my research group, including Mejdi Kammoun, Taylor Kelly, Bahar Moradi, William Walker, Mengying Yuan, Ahmet Akturk, and Sarah Aderyani. Mejdi and Taylor were especially helpful in introducing me to flexible and stretchable battery designs created by our research group, and I appreciate them for allowing me to collaborate with them on journal papers to provide analytical and computational verification to their experimental results.

I am most thankful to my wife, who has provided me so much love, emotional support, patience, caring, and understanding during this endeavor. She has provided so much encouragement during difficult times, especially during periods when I was not sure I could succeed in the completing this degree. She kept me going through

the program, despite the many nights when I was busy working on my research and coursework. I love her very much for all she has done to help me through this.

Finally, I would also like to thank NSF and TcSUH for providing financial support for completing the research that forms the basis of this dissertation. This financial support helped to make it possible to complete my degree.

Development of Analytical Models for Evaluating the Mechanical and Electrochemical Response of Flexible and Stretchable Lithium Ion Battery Materials

An Abstract

of a

Dissertation

Presented to

the Faculty of the Materials Science and Engineering Program

University of Houston

In Partial Fulfillment

of the Requirements for the Degree

Doctor of Philosophy

in Materials Science and Engineering

by

Sean Berg

December 2016

Abstract

Flexible and stretchable batteries have become a highly active area of research in recent years due to a new demand for mechanically compliant energy storage devices for a wide range of flexible applications including wearable and implantable electronics, touch-screens, and smart technology. Lithium ion batteries are leading candidates for flexible and stretchable energy storage devices due to their high energy density and efficiency. Considerable research has been related to developing flexible and stretchable materials, and solid polymer electrolyte lithium ion batteries show promise, offering many mechanical and safety advantages. While much experimental work has been in the development of these batteries, considerably less analytical modeling and numerical work has been a part of the development, which would elucidate experimental observations and provide enhanced understanding of the materials behavior in these new batteries.

The work presented in this dissertation includes results of computational modeling and simulation of the mechanical and electrochemical behavior of flexible and stretchable battery materials under normal operating conditions and applied deformations resulting from mechanical loads. Additionally, analytical multiphysics models in the form of series of differential equations were derived to explain experimental observations of changes in battery performance and material properties due to applied loads and deformations. These models can be used to predict materials behavior and to relate key design parameters of flexible and

stretchable batteries. The battery materials and designs that are assessed in this work were developed in our lab. Objectives of this work include understanding relationships between mechanical loading and certain key controllable fabrication parameters such as layer interface contact properties to predict the influence on flexible battery performance, and exploring how deformation occurring in the polymer electrolyte due to an applied mechanical load influences electrochemical performance. The effect of loading on other performance parameters, including battery impedance, is further studied, and all analytical work is compared to experimental data.

An important aspect of this development is the consideration of nonlinearity in the models. Novel approaches are taken to include and address nonlinearity within the systems considered. While these models can be simplified through linearization, limitations of linear solutions are also discussed.

Table of Contents

List of Figures

List of Tables

Chapter I Introduction

1. Motivation and objectives

Considerable advancement in technology in recent years has created a growing demand for safe, reliable, and robust energy solutions that are small, lightweight, and portable. From medical devices, to consumer products, to the latest imaginative creation from the tech industry, the demand for new and innovative energy storage devices that are optimized for these applications, and that minimize environmental impact, has grown and led to new design and materials selection challenges [1-7]. This is particularly true now with a trend towards "smart" electronics that are designed specifically to withstand increased mechanical and thermal loading due to greater user interactivity and interfacing. It is driven by a requirement of the energy storage device to conform and contour to the shape of certain electronic devices as they are twisted, stretched, rolled, or bent. This has prompted increased interest in energy storage device materials that have enhanced mechanical flexibility and stretchability while maintaining desirable electrochemical properties, and has spawned a new and emerging area of research to address the problems that these new applications pose. Development of new materials and design concepts for energy storage devices for these applications include thin-film, lightweight, small, flexible and stretchable batteries. Extensive theoretical, analytical, and experimental work is currently in progress in these areas that includes materials selection, conceptual design and development of energy storage devices, and testing. Since the

applications themselves present a challenge, these new types of batteries, particularly flexible and stretchable batteries, are not yet well understood.

One such suitable candidate for these new technological applications are lithium ion batteries because they offer many advantages that will be discussed later in this dissertation, and are currently widely used in many electronics devices [8]. The challenge is that conventional LIBs are not optimized for many of the newer applications where more mechanically compliant and load resistant energy storage devices are desired [9-11]. Currently much experimental research is in-progress to study and develop new flexible and stretchable battery designs, fabrication and testing methods, and materials. As a result of this work new battery concepts have been developed, and important observations have been made with regard to identifying performance limitations and materials phenomena [11-12]. In review of the literature in this area, less work has been in analytical modeling of flexible and stretchable energy storage devices and associated materials behavior. The focus of this research is on analytical and computational modeling of flexible and stretchable LIBs to provide enhanced understanding of certain key aspects of battery performance, which includes developing a relationship between various battery design parameters and material properties. An important aspect of this research is modeling the materials response and behavior in flexible and stretchable LIBs under normal operation and in application, and modeling materials phenomena observed in experiment, with the objective of understanding physical mechanisms that may influence battery performance.

2. Energy economy

The industrial revolution began a considerable change in energy consumption trends that progressed throughout the twentieth century and into the twenty-first century. The rise of mass production, the development of internal infrastructures, and the coming of new modes of transportation allowed many consumer products to be made available to many people around the world. This changed the market place considerably. However, with increasing populations, increasing product demands, globalization, and a desire for ever increasing modern conveniences, often facilitated by technology, the energy demand has skyrocketed at an alarming rate. While conventional forms of energy, such as fossil fuels, and even traditional batteries, have been sufficient to meet the global energy demand, they have had an adverse environmental impact that has sparked the desire for development of new energy options. Additionally, the advancement of technology has increased the demand for energy storage devices, and the limitations of conventional energy options for newer technological applications have been exposed. A more in-depth look into various energy options, and their advantages and disadvantages, is discussed in the following.

2.1 Fossil fuels

Fossil fuels have been in use in one form or another for centuries. The most widely used are natural gas, gasoline, diesel, kerosene, and coal, which have all been used for heating, production of electricity, and to power vehicles such as cars, airplanes, and trains. Fossil fuels have been a reliable energy source due to high

energy density and high power density. Particularly what makes them especially attractive is that the cost of the energy is cheaper than many other options in the market place [13]. Fossil fuels have comprised a large percentage of energy consumption worldwide, and have been capable of sustaining global energy demands. However, many studies have shown that fossil fuels come with a cost: negative environmental impact [14-15]. This is due in part to drilling and production methods, particularly those for extracting shale gas, which includes fracking. Combustion products from the heavy use of fossil fuels contribute to greenhouse gas production, including high CO_2, NO_x, SO_x, and particulate emissions. Though the environmental impact due to fossil fuel extraction and usage is not the number one factor in climate change, policy decisions are currently being discussed to draw down the usage of this energy form over the next coming decades.

Fossil fuels may be well suited to meet the demands of industrial applications, but they are limited in their ability to serve directly as energy sources in some of the latest medical, tech, and consumer product applications. In other words, an internal combustion engine is not an ideal power source for a smart phone. However, petroleum products are often suitable for creating some energy storage materials, specifically polymers for use in solid polymer electrolyte batteries, which will be discussed in later sections.

2.2 Renewable energy

In order to offset some of the environmental impacts of fossil fuels, and to supplement the global energy demand, so-called “renewable” forms of energy are in

use, and current development is progressing to make them more efficient, more cost effective, and to maximize potential power production. These forms of energy include solar, wind, geothermal, and ocean energy [16]. The primary challenge to using renewables is that, while the energy input typically takes advantage of natural phenomena, including wind and wave energy, heat from the earth, and heat from the sun, they are generally less reliable than fossil fuels. As a result, the consumer cost for these forms of energy is considerably higher than that of fossil fuels, and the infrastructure does not yet exist to make them more cost effective [17]. Renewable energy is an active area of research.

As potential energy solutions for some of the new electronics applications previously discussed herein, of all of the current renewable energy options, solar is the primary form that could be a potential candidate. However, presently there are a number of limitations, including energy density and power density, and availability of solar energy. These hurdles make solar a less viable option than other energy storage devices, such as batteries.

2.3 Fuel cells

Fuel cells have been sought after over conventional internal combustion engines and gas turbines since their combustion products contain water vapor and fewer greenhouse gases. Fuel cells operate as an electrochemical device and are very similar to batteries. The fuel used in these devices contains hydrogen, often from natural gas, such as methane. The fuel cells contain electrodes, and a separator or electrolyte, where hydrogen ions permeate the electrolyte, and the excess electrons

flow through an external circuit. Hydrogen from the fuel reacts with oxygen at an air intake, which drives a formation chemical reaction that facilitates energy production [18].

Fuel cells are typically capable of generating large-scale power (on the order of MW), and are better suited for use in small power plant applications. Fuel cells have even been considered for automobiles, such as Toyota's Murai; however, for use as small, portable energy devices, they are too large of scale, and are not suitable for such applications.

2.4 Batteries

Batteries are an excellent candidate for many electronics applications where small size and portability are desired. Batteries are classified as an electrochemical source of energy, with a similar configuration to that of a fuel cell, from which electrical energy can be extracted from an energetically favorable chemical reaction. During the intercalation process, ion transport is driven by a difference in chemical potential between the electrodes. The electrolyte selectively allows positive ions to diffuse through its medium during intercalation. As the reactant species ionizes and diffuses through the electrolyte to complete the chemical reaction, electrons flow through an external circuit, which is how the electrical energy is extracted from the battery.

There are different types of batteries including primary batteries, which are batteries that are not rechargeable, and secondary batteries, which are batteries

that are rechargeable. In the secondary (rechargeable) battery the chemical reaction is reversed by the addition of external energy, which is often in the form of electrical energy from a charger or outlet. Some of the various types of common batteries include the alkaline battery, such as the Zn-MnO_2 battery, which is a primary battery, and some secondary batteries, which include lead acid batteries, and Ni-Cd batteries [19]. There are also some less common batteries such as the lithium iodine battery, which is useful in pacemakers since it has a long life, and makes it well-suited for that particular application.

The selection of a particular type of battery is directly related to some of the performance capabilities of that particular battery. Some important features to consider include energy density, power density, voltage, charge and discharge rate, cyclic performance, safety, and whether the battery is rechargeable [20]. The word density in this context refers to the energy or power available per unit volume of battery, as size restrictions are an important feature in many applications. Therefore, in selecting an appropriate battery, in the case of the pacemaker, the lithium iodine battery has a high energy density, but the application does not require a high power demand. Lead acid batteries are desirable for automobiles since they are capable of high discharge rates and high power density, but the energy density is relatively low. For consumer electronics, and other applications discussed previously, these types of batteries may not be optimal. Lithium ion batteries have been found to be a good option for many electronics applications, given a reasonable balance between energy density and power density, and the fact

that they are secondary (rechargeable) batteries. These types of batteries are the focus of this research, and will be discussed in greater detail in later sections.

2.5 Other portable energy storage devices

There are many other forms of energy storage that span various types of energy. Figure 1 depicts the various types of energy by category. Other energy storage types include mechanical devices, such as flywheels, springs, hydraulics and pneumatics; thermal energy storage, including molten salt and processes that take advantage of phase transformation and latent energy; and chemical energy, including hydrogen, natural gas, and biofuels.

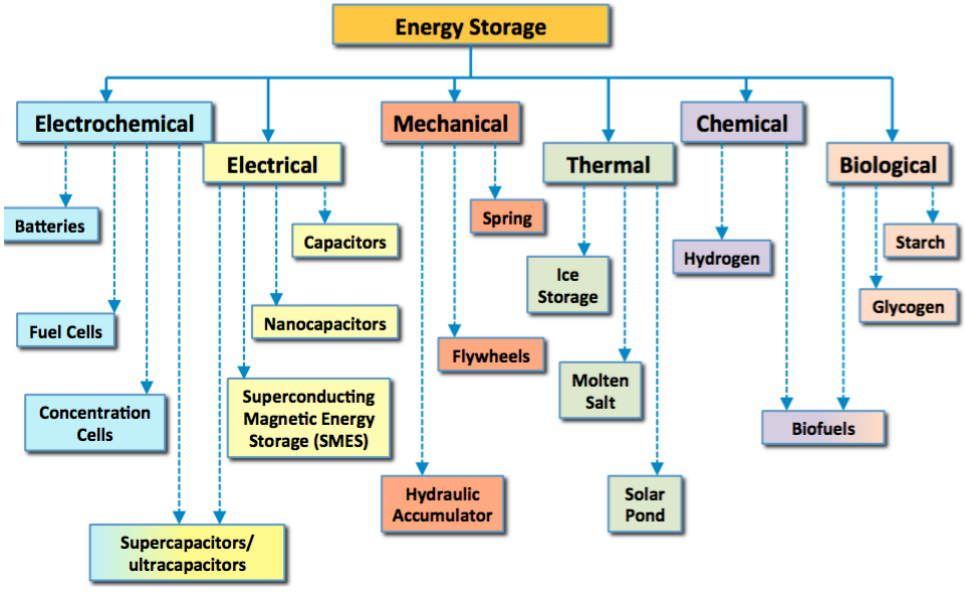

Figure 1: Categories of various energy storage mediums by energy type (courtesy of H. Ardebili).

As it relates to this work, electrical energy storage devices are particularly important [21]. A widely used electrical energy storage device is a capacitor. A

capacitor is a passive component consisting of two parallel plates separated by a dielectric, where charge is stored in an electric field, and the charge is proportional to voltage. The current, and subsequently voltage, across a capacitor can be modeled using a combination of Kirchhoff's Law and Ohm's Law as shown in the following:

$$RC\frac{di(t)}{dt} + i(t) = 0, \quad (1)$$

$$i(t) = i_o e^{-\frac{t}{RC}}, \quad (2)$$

$$i = \frac{V}{R}, \text{ and} \quad (3)$$

$$V(t) = V_o\left(1 - e^{-\frac{t}{RC}}\right), \quad (4)$$

where i is the current response, V is the voltage response, R is the resistance of the resistor, and C is the capacitance. An important design feature of a capacitor is the fact that the capacitance is governed by

$$C = \frac{\varepsilon A}{d}, \quad (5)$$

where capacitance is dictated by the plate cross-sectional area, A, and the plate separation distance, d [22]. This inverse proportionality between plate separation and capacitance drives an area of research and development related to supercapacitors and nanocapacitors. Supercapacitors and nanocapacitors are designed to yield a substantial increase in capacitance, as well as high power density and fast discharge rates. While materials advancements have led to enhanced performance, these devices typically have very low energy density, which makes

them not well suited as a primary power supply for many modern electronics devices [23-26].

3. Lithium ion batteries

In comparing the energy densities and power densities of various energy storage options, it can be seen that lithium ion batteries (LIBs) possess a good balance between these two characteristics, as shown in the Ragone plot in Figure 2, when compared with other types of batteries. This makes them an attractive candidate for development into thin-film, lightweight, flexible and stretchable batteries for next generation electronics devices [27]. In order to develop this technology into flexible and stretchable batteries, both design and materials challenges exist. These topics have been of great interest in scientific research in recent years [28-34]. Because of the nature of these types of applications, specifically the demand for these batteries to perform under mechanical and thermal loads, this may require addressing both the design and materials challenges simultaneously. Considerable progress has been made in these areas in recent years [35].

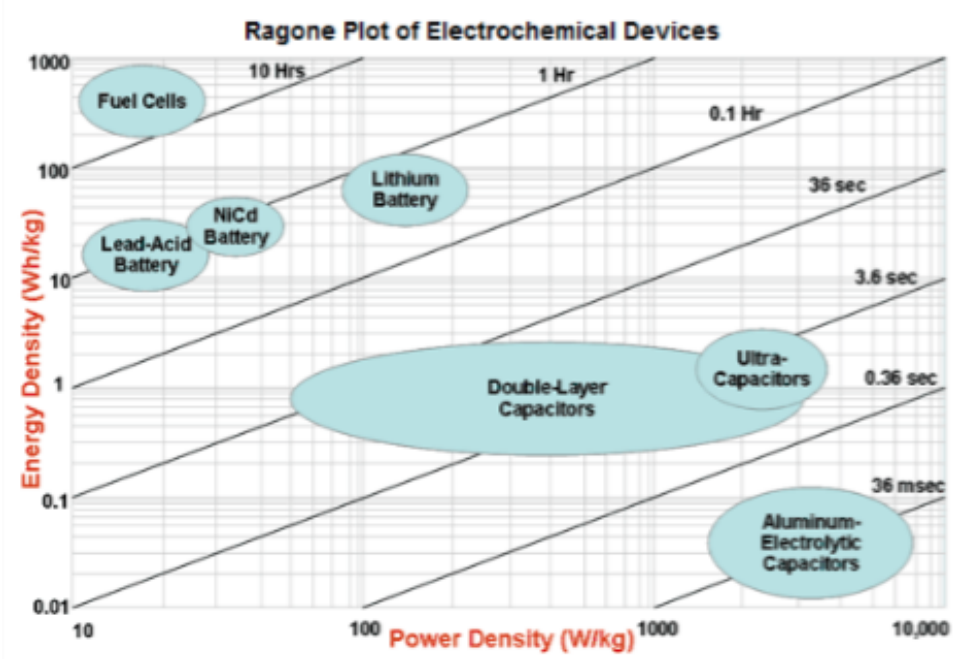

Figure 2: Ragone plot comparing the energy densities and power densities of various electrochemical energy storage devices (Source: US Defense Logistics Agency, 2011).

3.1 Potential applications for flexible and stretchable LIBs

Many of the new applications that make flexible and stretchable LIBs appealing include implantable medical devices, flexible touch-screens, wearable "smart" clothes that measure vitals, and wearable personal protective equipment (PPE), which is desired in industrial applications such as manufacturing and Oil & Gas. The common denominator between these applications is the potential for the electronic devices to be subjected to mechanical and thermal loads. Therefore creating power sources capable of withstanding these loads without degraded performance is desirable. Since the trend in new electronics is towards smaller and more compact devices, conventional batteries, including alkaline batteries and even coin cell

batteries are not optimized to operate in these applications due to their size, weight, and rigidity.

In order to provide suitable batteries to meet the latest market demand to serve as power sources in these applications, many new flexible and stretchable lithium ion batteries are currently being conceptualized, prototyped, and tested. These various batteries concepts employ a number of new and novel materials, fabrication methods, and unique designs. For the purposes of this work, there is a distinction made between flexible and stretchable battery designs. In this context, stretchable batteries are designed to accommodate loading generally due to uniaxial tension, which would cause elongation or stretching of the battery. Flexible batteries are designed to withstand bending and torsional loads. The challenges and development of these types of batteries are outlined in the following.

3.2 Design of flexible and stretchable batteries

In order to address the challenges these applications present, a number of battery designs have been conceptualized. A number of thin-film flexible battery concepts have been designed, fabricated and tested [10, 28, 36-51]. Min Koo et al. created a flexible, solid-state battery using an approach that allows for the development of a wide range of flexible batteries regardless of electrode material; their battery was successfully tested by powering a LED while under bending, and was further studied using finite element modeling [28]. In our laboratory we developed a flexible solid polymer electrolyte LIB that was able to withstand large bending loads, and was capable of powering a LED for multiple charge/discharge

cycles [11]. Likewise several concepts for stretchable batteries have been developed [6, 39, 40, 42, 45-47, 52-70]. A stretchable battery with self-serpentine interconnects was developed and tested for stretchable electronics by Xu and associates [45]. The style and configuration of a flexible battery may be unique in order to accommodate specific loading for the application of interest, so that it deforms easily with the electronic device it is powering. While some batteries are better designed to accommodate bending and twisting, others may be optimized for tensile or extension loads. The objective in the design is to ensure continuous function of the battery, meaning no delamination of the contacting battery layers. Accordingly, the materials selected must also meet the demands of the application.

3.3 Battery materials

Mechanically compliant materials are often desired for these applications [47, 56]. A balance between materials that offer mechanical advantages under loading, and that facilitate good electrochemical performance, are targeted. This has resulted in the development of new and novel materials and fabrication techniques [1, 9, 36, 71-74]. A typical lithium ion battery consists of electrodes: an anode (negative terminal), and a cathode (positive terminal). It also contains an electrical insulator between them called an electrolyte. Other components of the battery may include current collectors and current conductors, and outer encapsulation or outer packaging [75-76].

Development of electrode materials in flexible and stretchable LIBs is currently a highly active area of research. Some common materials for the cathode include

lithium salts deposited onto the current collector, such as $LiCoO_2$ and $LiFePO_4$ [77-78]. The cathode is the source of lithium in a LIB, and it is important that the cathode material be both electrically and ionically conductive, stable during flexing and stretching, and incur little to no degradation during cycling [79].

In LIBs the anode has a long and varied history of different materials. Initially the use of lithium metal seemed to offer many advantages since it has a high energy density, and it is the most electropositive and lightest weight metal [80-81]. However, there are many disadvantages to use of lithium metal including instability, which presents greater safety concerns, and the fact that dendritic growth leads to diminished performance after multiple cycles. Therefore alternatives were sought after, and carbon has become a very widely used anode material [82]. Since the intercalation process may result in straining or swelling of the anode matrix, interest in the development of materials capable of handling high strain without fracture are targeted, which has led to use of carbon nanotubes [83-85], nanowire [86-88], and graphene [10, 89-90].

The battery capacity is mainly controlled by the electrode material and structure, and enhancing battery capacity will help to improve battery performance. However, issues associated with the formation of a solid electrolyte interface (SEI) layer at the anode during charge-discharge cycles can result in a degradation of capacity [91]. The capacity can also be improved by selection of different anode materials, including silicon and lead. Use of silicon may serve to substantially

increase the capacity of the battery, but due to high volume change during intercalation, high stress and susceptibility to fracture presents an obstacle [92-94].

The electrolyte acts as an electrical insulator only allowing the Li ions to pass through it. Preferred properties in an electrolyte include good ionic conductivity, low electrical conductivity, and for flexible and stretchable battery applications, mechanical properties that allow for high deformation [95]. The electrolyte can take the form of liquids, including organic and inorganic liquids [6, 96-100], gels [101-105], and solids such as ceramics [106-113] and polymers [114-121]. Liquid electrolytes offer relatively high ionic conductivity among the electrolytes, but the risk of leakage, safety problems, and incompressibility of the liquid make them less optimal for flexible and stretchable battery applications. Gel electrolytes offer very good ionic conductivity; however, they are composed of a liquid phase that can be highly flammable and therefore, come with an increased safety risk. Ceramics can offer very high ionic conductivity, but due to their bonding, their mechanical properties make them considerably more rigid and brittle when compared with other materials options. Specifically, in flexible and stretchable battery applications, ceramic ion conductors make poor candidates for the electrolyte because they are susceptible to brittle fracture, and have a low strain-to-failure ratio. Polymers are possibly the best candidates for flexible and stretchable batteries since they are highly deformable and mechanically compliant, they suppress the development of the SEI layer, and they are more chemically stable. However, they have the lowest ionic conductivity of all of the current available options. The addition of plasticizers and nano-fillers has shown to improve the ionic conductivity of the solid-state

polymer electrolyte. In the case of plasticizers, the ion conductivity can be greatly enhanced; however the mechanical properties are often compromised. Nanofillers have been demonstrated to enhance both the ion conductivity and mechanical properties of the polymer electrolyte [122-135]. The improved ion conductivity in nanocomposite electrolytes is thought to be due to the fact that the addition of nanofillers, such as graphene-oxide, may disrupt the crystalline grain growth within the polymer, as shown in Figure 3 [11] leading to higher conductivity amorphous (non-crystalline) regions in the polymer. With many different options for electrolyte materials, performance specifications, such as higher voltage requirements, may limit the availability of optimal materials for flexible and stretchable LIBs [136].

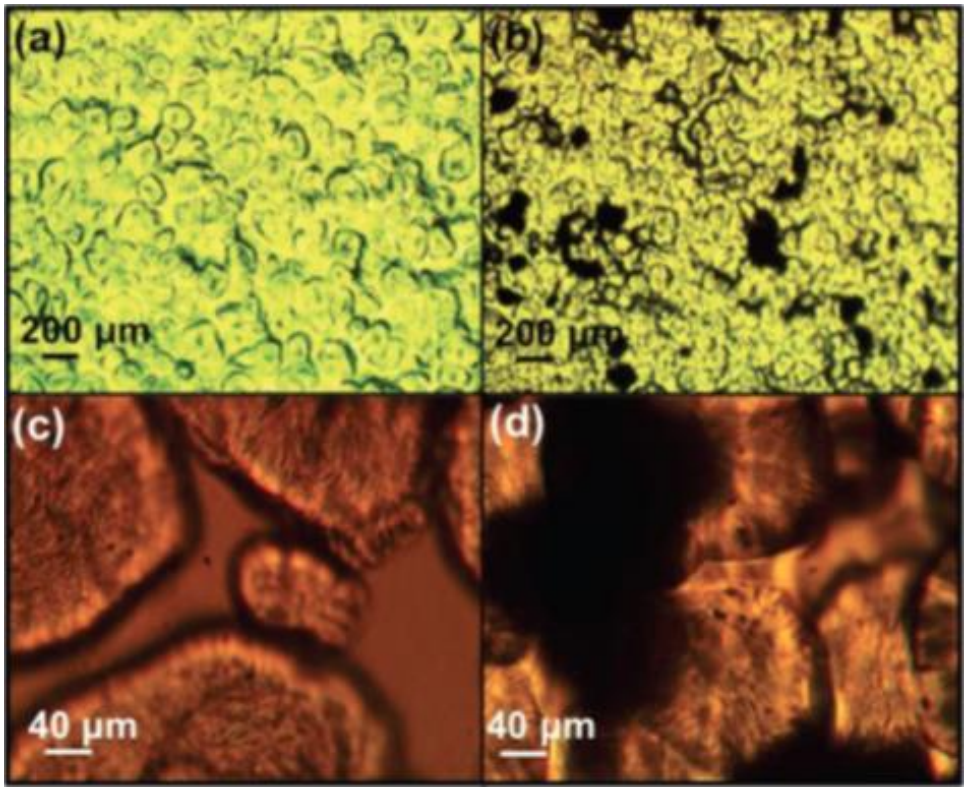

Figure 3: Polarization light microscopy (PLM) of (a), (c) pure PEO and (b), (d) PEO with 1 wt% GO (provided courtesy of [11]).

4. Selection of analytical methods

The process of optimizing the battery design is enhanced by the development of analytical models, methods, and techniques, which are useful for modeling the materials behavior in the battery, and relating the various performance parameters of the battery. These parameters can be in the form of geometric dimensions, contacts and interactions, and electrochemical and mechanical response including stresses and strains, and ionic conductivity, in order to understand the overall physics of the flexible battery. An important goal in the analytical modeling is to predict the materials behavior under operating conditions in application. Depending on the type of modeling techniques used, materials behavior and response such as stresses, strains, fracture, thermal expansion, chemical reactions, bonding and atomic forces, and electronic properties can be quantified and evaluated. The method and sophistication of the modeling technique will dictate which quantities can be calculated. Modeling materials behavior analytically and computationally has been a very active areas of research, and three widely used analytical modeling methods include continuum modeling, molecular dynamics modeling, and quantum mechanics modeling [137-184]. The various modeling methods for evaluating materials behavior will be discussed in the following.

4.1 Continuum modeling

The development of any fundamental analytical physics model begins with the application of known laws, such as conservation of energy, conservation of mass, or

laws of motion. In this context a model is meant to describe an ordinary or partial differential equation, or system of ordinary or partial differential equations, which can be used to better understand the governing physics within a given system. A principal difference between various modeling methods is the way in which the matter under consideration is treated; that is, whether the interactions between atoms or subatomic particles are considered.

In continuum modeling the matter under consideration is often modeled assuming "bulk" or macroscopic behavior, and the influence as a result of interactions between atoms, and quantum effects, is generally ignored. For example, it is often convenient to quantify the average atomic kinetic energy and interatomic forces of an ideal gas using quantities such as temperature and pressure. These quantities can be calculated by applying thermodynamic laws to the system of interest, which can then be used to obtain equations of state. For example, in an ideal gas it is assumed that the effects of molecular interaction are negligible by assuming a low gas density. Considering a small quantity of the gas, or control mass, in a closed system, the 1st law energy balance results in

$$dE = \delta Q - \delta W, \qquad (6)$$

where E is the internal energy of the gas, and Q and W represent the heat transfer and work crossing or done by the boundary of the control mass. The internal energy can be expressed as a function E=f (S, V, N), where S is the entropy, V is the volume of the control mass, and N is the number of moles of a particular gas species. For a

system that progresses between states quasi-statically, the differential internal energy can be rewritten as

$$dE = \frac{\partial E}{\partial S}\Big|_{V,N} dS + \frac{\partial E}{\partial V}\Big|_{S,N} dV + \sum_i \frac{\partial E}{\partial N_i}\Big|_{V,S} dN_i \text{ and} \quad (7)$$

$$dE = TdS - PdV + \sum_i \mu dN_i, \quad (8)$$

where the variables of pressure, P, temperature, T, and chemical potential, μ, can be substituted for the partial differential terms. These equations represent a continuum model that can be used to determine the relationship between various system parameters, which is useful for understanding and predicting changes in said system. In the case of an ideal gas, the variables of pressure, temperature, volume, and moles of species can be represented in a state equation of the form

$$PV = NRT, \quad (9)$$

which is widely known as the ideal gas equation, where R is the Universal Gas constant. It can predict changes in pressure, temperature, and volume between states. It is convenient to obtain a continuum equation in terms of parameters that are experimentally measureable, such as pressure, temperature, and volume.

Another example of a continuum model is the Navier-Stokes equations for fluid flow, which are a set of partial differential equations based on conservation of mass and momentum. These equations are key to modeling the velocity field of a fluid through a control volume of interest, and can be given by

$$\frac{\partial \rho}{\partial t} + \frac{\partial (\rho u)}{\partial x} + \frac{\partial (\rho v)}{\partial y} + \frac{\partial (\rho w)}{\partial z} = 0, \tag{10}$$

$$\frac{\partial (\rho u)}{\partial t} + \frac{\partial \left(\rho u^2\right)}{\partial x} + \frac{\partial (\rho uv)}{\partial y} + \frac{\partial (\rho uw)}{\partial z} = -\frac{\partial P}{\partial x} + \frac{\mu}{Re}\left[\frac{\partial^2 u}{\partial x^2} + \frac{\partial^2 u}{\partial y^2} + \frac{\partial^2 u}{\partial z^2}\right], \tag{11}$$

$$\frac{\partial (\rho v)}{\partial t} + \frac{\partial (\rho vu)}{\partial x} + \frac{\partial \left(\rho v^2\right)}{\partial y} + \frac{\partial (\rho vw)}{\partial z} = -\frac{\partial P}{\partial y} + \frac{\mu}{Re}\left[\frac{\partial^2 v}{\partial x^2} + \frac{\partial^2 v}{\partial y^2} + \frac{\partial^2 v}{\partial z^2}\right], \text{ and} \tag{12}$$

$$\frac{\partial (\rho w)}{\partial t} + \frac{\partial (\rho wu)}{\partial x} + \frac{\partial (\rho vw)}{\partial y} + \frac{\partial \left(\rho w^2\right)}{\partial z} = -\frac{\partial P}{\partial z} + \frac{\mu}{Re}\left[\frac{\partial^2 w}{\partial x^2} + \frac{\partial^2 w}{\partial y^2} + \frac{\partial^2 w}{\partial z^2}\right], \tag{13}$$

where Re is the Reynold's number of the flowing fluid, and u, v, and w represent the directional velocities in a Cartesian coordinate system.

In solid bodies, important quantities that are helpful for predicting materials behavior include the stress and the strain. The behavior of a deformable body subjected to external forces can be modeled by consideration of an infinitesimal region within the body. If the body elastically and uniaxially deforms, the relationship between the stress in the body and the strain can be represented by Hooke's law as

$$\sigma = E\varepsilon, \tag{14}$$

where σ is the stress, ε is the strain, and E is the elastic modulus. The deformation in a body can be approximated linear elastically using this continuum-based relationship in the region of interest if inelastic deformation is negligible. These are particularly import quantities that provide a basis for understanding the material behavior within flexible and stretchable batteries, since the applications of interest generally result in loading that will deform the batteries. The stresses and strains in a region of a body are represented by tensors, since the stress and strain acting on a

3D region of interest, as shown in Figure 4, act with respect to a direction on each face.

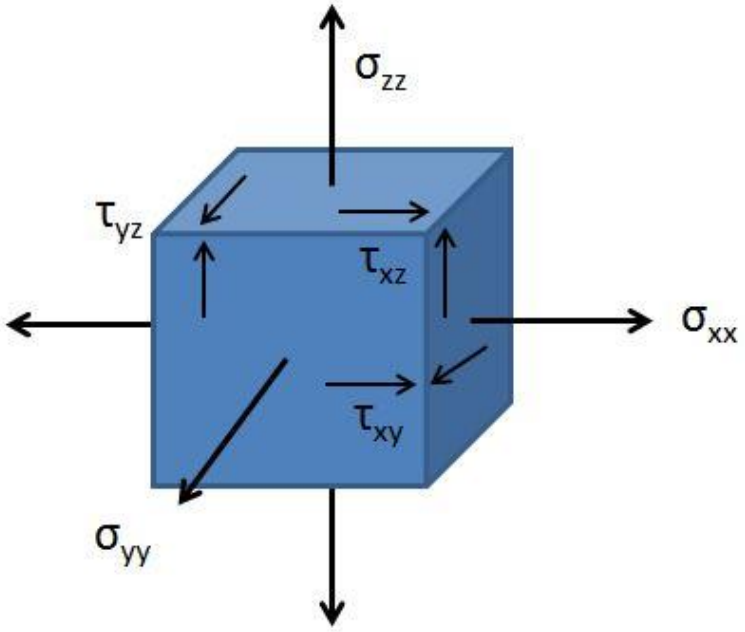

Figure 4: Element representing a region within a body under applied stress.

The strain is reflective of a displacement change that occurs in the body, and is represented by

$$\nabla u = \begin{vmatrix} \varepsilon_{11} & \varepsilon_{12} & \varepsilon_{13} \\ \varepsilon_{21} & \varepsilon_{22} & \varepsilon_{23} \\ \varepsilon_{31} & \varepsilon_{32} & \varepsilon_{33} \end{vmatrix}, \qquad (15)$$

where u is the local displacement in a body, and the components, ε_{ij}, of the tensor represent the directional strains.

Multiple studies have been focused on modeling battery behavior using continuum methods [171-174]. Baker and colleagues used a continuum approach

and thermodynamics laws to model the strain behavior due to diffusion in a lithium ion battery considering small deformation assumptions [174]. In addition to modeling the stress/strain response, understanding the material limits is also an important part of the battery design. In this context, fracture is a materials failure mode that is limiting to the design. Flexible and stretchable battery electrodes are also susceptible to fracture, and this mode of failure can result in a battery ceasing to function properly. Fracture due to applied loading often occurs due to cyclic loading, which results in an alternating stress. In ductile materials, substantial plastic deformation can occur at fracture, and alternating strain may be considered. Continuum-based modeling methods have been developed to model fracture in battery materials using linear and nonlinear methods [175-176].

An important material property used for predicting fracture in a material is the fracture toughness, which is a material resistance to fracture. In continuum-based modeling, this property is an input often obtained from materials testing. In other forms of modeling, to be discussed later, it is possible to quantify fracture resistance by understanding the material on the atomic level through bonding and dislocation motion, as well as consideration of quantum effects. Continuum models can predict crack propagation. One example of a model used to predict the crack stress field and strain energy release rate is an energy-based solution called the J-integral method, which models the system as shown in Figure 5, and is given by

$$J = -\frac{dU}{da} = \int_{\Gamma} \left[W dy - T \frac{du}{dx} ds \right], \qquad (16)$$

where J represents the partial derivative of internal energy with respect to the crack size, W is the work or the strain energy release rate, and T is the traction vector. The J integral is performed on a path around the crack tip, and can be compared directly with a J_{Ic} value of fracture toughness for the material, which is obtained through materials testing. It is common to numerically integrate this quantity, since a closed-form solution is often difficult to obtain.

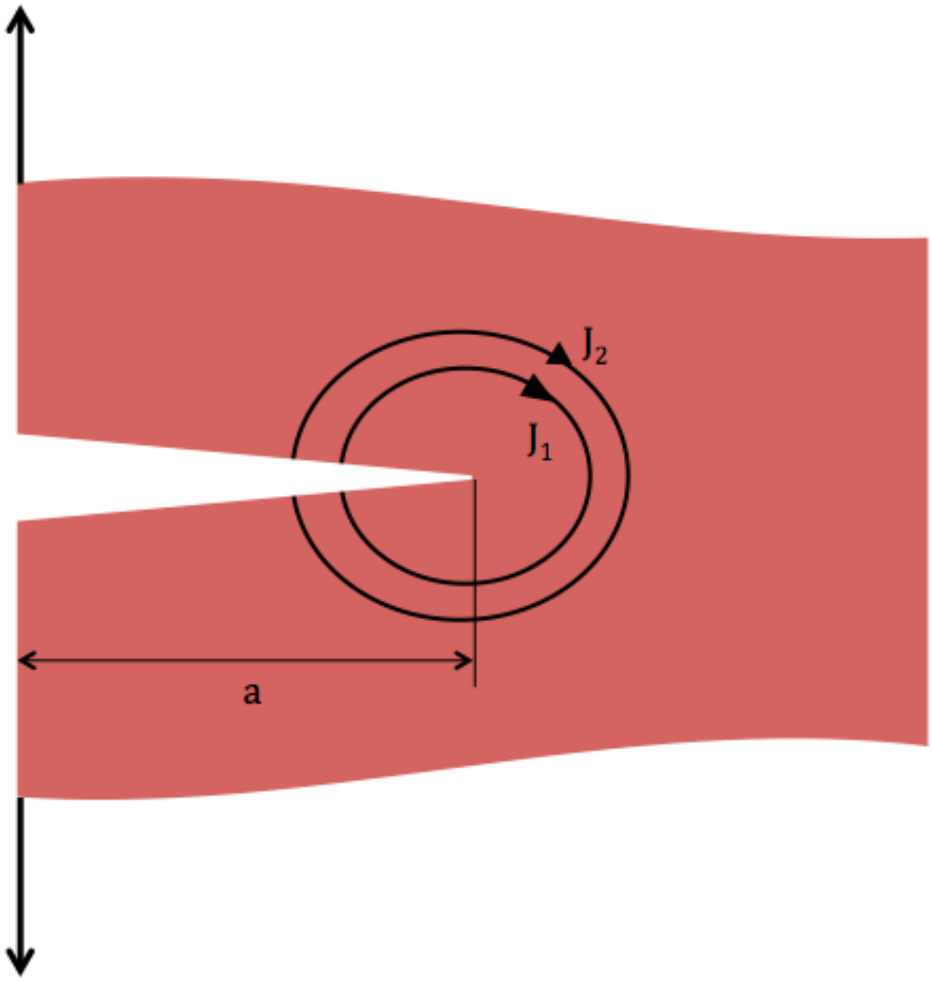

Figure 5: Crack configuration used as basis for the J integral method.

4.2 Molecular dynamics

Another area of modeling materials behavior is molecular dynamics (MD). This is an active area of research, and has been applied to modeling battery materials [177-182]. The purpose of molecular dynamics is to model the interaction of atoms at the atomic level, by capturing the kinetic and potential energy of each atom. Atomic motion in a crystalline lattice, for example, consists of translations, rotations, and vibrations, which contribute to the energy of each atom. The average kinetic energy of the atoms in a sample is an indication of the temperature of the sample.

The potential energy is a quantity of particular interest because this is directly related to the interatomic forces through its derivative. An active area of research is to characterize the potential energy function of an atom for various materials of interest as a function of separation distance, r. The Lennard-Jones potential is a common and simple potential, where the potential energy and force are given by

$$V = 4\zeta\left[\left(\frac{\eta}{r}\right)^{12} - \left(\frac{\eta}{r}\right)^{6}\right] \text{ and} \tag{17}$$

$$F = \frac{dV}{dr} = 24\zeta\left[\left(\frac{\eta}{r}\right)^{7} - 2\left(\frac{\eta}{r}\right)^{13}\right], \tag{18}$$

where V is the potential energy, F is the interatomic force between adjacent atoms, and in this case, ζ and η are an empirical constants. The importance of deriving useful potentials is that the material properties, including thermal conductivity and elastic modulus, can be predicted. The effect of material defects such as vacancies, impurities, and line defects including dislocations and dislocation motion, can be

used to model material response under external loading, and this has been done extensively.

Currently the challenge in MD simulations is that equations modeling multiple degrees of freedom for every individual atom within a material of interest must be developed. For a sample of interest that contains 1 mol of species, this can be approximately on the order of 10^{23} equations. This requires considerable computing resources to simultaneously solve this system of equations. Simplifications can be used for MD modeling, including use of periodic boundary conditions. However, care must be taken to ensure that appropriate boundary conditions are used to obtain results that accurately reflect the behavior of the materials.

4.3 Quantum mechanics

Use of quantum mechanical modeling is also a very powerful means of predicting and understanding materials behavior. While classical molecular dynamics can be insightful into atomic interaction, it is based on Newtonian motion, which is not capable of capturing quantum effects. Specifically this is true in relation to capturing the electronic interactions within an atom. Quantum mechanical modeling considers the energy of electrons and is capable of predicting materials behavior under conditions where measurement of material properties may be difficult, such as at extreme temperatures and pressures. Advantages to using quantum mechanics is that it is possible to model materials behavior more completely without materials testing; however, due to the complexity and the computational requirements to

obtain solutions, fewer quantum mechanics-based studies have been conducted on batteries [183-184].

5. Linear and nonlinear modeling

5.1 Simple linear models

The focus of this work is on continuum-based modeling, and the consideration of nonlinearity in the development of solutions. Nonlinearity is inherent in many real systems in the world. However, some simple systems can be modeled sufficiently using linear solutions. For example, in a Lagrangian system, for an arbitrary body under consideration, the kinematics and kinetics of said body, including rigid body motions, can be captured using kinematic and force balance equations. Therefore, the motion of a simple mass-spring-dampener system as shown in Figure 6 can be modeled by

$$\sum_i F_i = m\frac{d^2x}{dt^2} = -\mu\frac{dx}{dt} - kx, \qquad (19)$$

where m is the mass of the object under consideration, μ is the dampening coefficient of the dampener, and k is the spring stiffness. Likewise, in an Eulerian system, a control volume can be defined and application of energy and mass balances can result in state equations for the system.

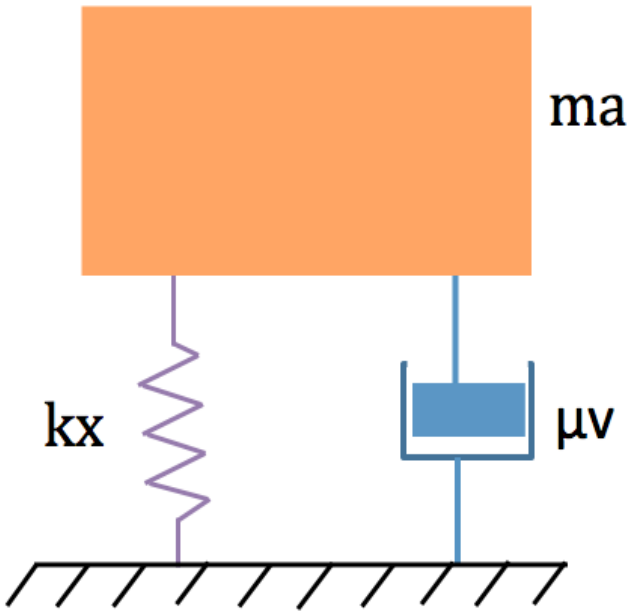

Figure 6: Illustration of a common mass-spring-dampener system.

The previous models are important and are very common physical models; however, they are considered to be linear systems, and many more realistic systems in the world include some form of nonlinearity. An example that includes nonlinearity is the Bessel function, which is shown as

$$x^2 \frac{d^2y}{dx^2} + x \frac{dy}{dx} + (x^2 - \alpha^2)y = 0, \qquad (20)$$

where α is a real constant, and x is an independent variable that typically describes spatial location within a body of interest. The Bessel function has many applications, and usually arises as a result of system geometry, such as consideration of spherical or cylindrical coordinate systems.

5.2 Forms of nonlinearity

Nonlinearity can exist in a number of forms. If the mechanics of a body under deformation are to be considered, which is the basis of much of the work in this dissertation, the principal nonlinear effects can be broken down into three general categories: geometric, material, and contact nonlinearity. Geometric nonlinearity may consider a result with respect to a volume change or significant shape change that occurs in a body of interest. In elasticity theory, such geometric nonlinearity results in higher order terms, which may be used to calculate true stress in a deformed body under an applied traction. Methods often require consideration of reference state and current state configurations, and mapping between these states can be carried out via the volume change term, or the Jacobian [185].

Material nonlinearity generally considers material deformation behavior beyond the elastic limit. There are a number of materials models that are used to predict the inelastic behavior of ductile, crystalline materials, and the viscoelastic and viscoplastic response in polymers, including semi-crystalline polymers, from which the batteries developed in our lab are made. For example, common techniques for modeling plastic deformation in ductile materials are to consider isotropic and kinematic hardening models. For an elastic-plastic material, an isotropic hardening model may be useful in applications where a body made of ductile material exceeds its yield point due to a non-reversing or non-cyclic load [186]. It may be included to predict global plastic collapse in a thick-wall cylindrical pressure vessel due to an applied uniformly increasing pressure load. The limitation of the isotropic

hardening is that it does not consider that tensile strain hardening can be accompanied by compressive softening, associated with the Bauschinger effect. In such a case it would not be able to properly model the material response due to a reversing bending load, for example, where a region in a body would be subjected to an alternating tensile and compressive stress. A kinematic hardening model is more effective for modeling this phenomenon since it is more capable of accurately accounting for the stress-strain hysteresis response [187].

Contact nonlinearity exists when the mechanical response of a body under deformation is influenced by contact with another boundary. For example, consider hyperelastic concentric cylindrical shells subjected to an internal pressure. If the inner shell radially and elastically deforms enough to contact the outer shell, the stiffness of the inner shell, and subsequently the radial deflection of the inner shell-outer shell composite changes at that point of contact. Thus, the sudden change is nonlinear and attributed to this contact.

5.3 Limitations of linear methods and comparison with nonlinear solutions

For a variety of applications, closed-form solutions obtained using linear methods may be adequate for predicting how a system responds. This is demonstrated in certain linear dynamics problems, including the mass-spring-dampener system previously mentioned, and in simple heat transfer problems involving conduction through simple geometries. However, in many structural applications, geometric nonlinearity, inelastic materials deformation, and contact between adjacent parts in an assembly is important to consider in design problems

since linear methods may fail to predict certain key behaviors, or they may fail to fully optimize a design [188]. Due to computing limitations, historically, a number of applications have been simplified or have approximated solutions based on linear methods. Recent advances in computing technology have allowed for more sophisticated computational models to be developed, and the finite element method has been used to further considerable advances in a variety of areas: for example, dental materials [189]. Nonlinear analysis and the finite element method have allowed engineers to consider new and more efficient designs in multiple industries [190-191]. In space applications, the consideration of nonlinear effects can be critical, and numerical models have additionally served to aid in design optimization [192].

One area that highlights the limitations of linear solutions is in the design of bolted flange connections. Bolted pipe flange connections are widely used in the Oil & Gas and Nuclear industries as a means of transporting fluids, often at elevated pressures, i.e., 10 MPa – 100 MPa, and elevated temperatures, i.e. 100 ˚C - 400 ˚C. The flange bodies and bolts are generally low alloy steel, and the gaskets are often stainless steel of grade 316 (SS316). These flanged connections may be subjected to external axial loading in addition to loading due to the transport fluid. Predicting the load carrying capacity of these flanges has been a topic of interest for many years in the energy industry, and predicting leak in a flange connection has led to multiple interpretations and methods [193-213]. API 6AF attempts to predict the additional axial tension and bending load capacities of API flanges, and provides accompanying capacity charts [214]. However, the methodology followed in API 6AF is based on a

linear finite element analysis, which is used to obtain these load capacity charts. The API 6AF methodology only considers a solution based on linear superposition of combined loading effects, and fails to consider the nonlinearity associated with such effects as material plasticity as a result of gasket deformation, and component contact interactions. It also makes a number of conservative assumptions that result in predicting unrealistically low flange capabilities. With the Oil & Gas industry trending towards completing wells in harsher environments with a potential for greater loading, it is important to develop a more efficient methodology for predicting pipe flange capacities [191].

As an additional sensitivity study in this dissertation to further illustrate the limitations of linear methods, a comparison of the methods prescribed in API 6AF, and nonlinear methods that consider a closer approximation of the true materials behavior in a bolted flange, is completed and discussed in Appendix A. The purpose of this work is to highlight the limitations of linear analytical methods by comparing them with nonlinear models, which more accurately and realistically predict the system behavior. From this work a new solution framework can be developed from this alternative approach. The model discussed in Appendix A considers an elastic-plastic constitutive materials response with isotropic strain hardening to assess the sealing integrity in the bolted flange.

6. Outline of dissertation

The purpose of this dissertation is to analytically and computationally model the physics and materials behavior, specifically the mechanical and electrochemical response, of flexible and stretchable lithium ion battery materials considering deformation and the influence of mechanical loads. The models serve as a basis for understanding the various parameters within flexible and stretchable LIBs to evaluate how normal operation and the applications impact the battery performance and materials behavior. The effects of nonlinearity are included in the modeling efforts, with comparison to linear methods. The results of the modeling efforts are compared to published experimental data from testing conducted in our laboratory.

Chapter I provides a discussion of the motivations of this research, and discusses the primary objectives of this work. Relevant background into the energy sector, including a discussion of various energy storage devices, is presented. A background of analytical methods and techniques is included in order to provide a basis for the models developed in this work, and an important discussion is provided on the importance of considering nonlinearity, and the limitations of linear solutions. Each section of this discussion was accompanied with a detailed literature review to elucidate the state of art of energy storage, materials selection, modeling methods, and battery technology.

Chapter II discusses the numerical methods used to evaluate the mechanical response of a solid polymer electrolyte flexible lithium ion battery that was developed and tested in our laboratory, and notes some key observations related to battery performance. The focus in this chapter is on the finite element modeling that was initially completed to capture the stress and deflection in this particular battery. This model was used to simulate some of the initial experimental work, which included the cycle and performance testing of the battery.

Chapter III expands on observations made from previous experimental and numerical work, and proposes an analytical model that builds on the previous understanding of the battery mechanical response. The proposed analytical model establishes a key relationship between input loading and layer interfacial contact properties, which are design parameters that are found to directly influence battery performance. The analytical model is solved with numerical methods, and using the finite element model previously discussed, several battery interfacial conditions are compared. The results obtained from the numerical work are correlated with experimental data to demonstrate a relationship between input loading, layer contact pressure, and impedance.

Chapter IV presents the results of numerical work that was completed to model the mechanical response of a unique stretchable battery concept that was developed in our laboratory. The special geometry of this particular battery was further studied, and an analytical model was derived to relate various geometric characteristics of the battery to the stress and deflection profile of the battery. This

model is useful for predicting the relationship between design variables, and to estimate material limits of the battery, which is useful in assessing battery performance.

Chapter V begins a new discussion to enhance the understanding of how material properties and characteristics such as bonding chemistry and microstructure of the lithium ion battery electrolyte affect battery performance. Since the electrolyte used in many of the battery designs considered is a solid-state, semi-crystalline polymer, the relationship between the electrolyte deformation, specifically the states and the mechanisms of deformation, and the ionic conductivity of the electrolyte, are qualitatively evaluated.

Chapter VI expands on the concepts presented in previous chapters to propose a series of multiphysics models based on the laws of thermodynamics and continuum mechanics to relate ion concentration and ionic conductivity with materials deformation. An important relation is used to relate mass concentration to ionic conductivity, which establishes a link between the ionic conductivity and strain. The model is in the form of a system of partial differential equations that couple mass diffusion and material strain. The approach to arrive at these equations assumes a generalized control volume, with mass and energy balances, but requires the assumption of an expression for internal energy density. The solution considers the effect of nonlinear geometry. A series of assumptions are made, and boundary conditions are defined, in order to model an experiment conducted in our lab that measures change in ionic conductivity with applied uniaxial strain. The equations

simplify to obtain a closed-form solution, which is then plotted graphically, and is compared against published experimental results. The analytical model is then applied to the flexible battery design previously considered. Boundary conditions are modified accordingly, and the equations are solved numerically. A plot of the spatially varying ionic conductivity in the polymer electrolyte as a function of the local strain field is generated for various degrees of loading, and this solution is correlated with published experimental data.

Chapter VII summarizes the overall findings and results from this dissertation work, along with detailed discussion of the implications. The limitations of this work are discussed, and recommended future work is proposed in order to further advancement in this area.

Chapter II Modeling the Mechanical Response of a Flexible SPE LIB

1. Flexible battery design and fabrication

A flexible solid polymer electrolyte (SPE) LIB was fabricated in our laboratory and subjected to testing to evaluate the performance under an applied bending load. The design of the flexible battery utilized stacking of the battery components into layers. The layers included the electrodes (anode and cathode), electrolyte, current collectors, and current conductors. Aluminum foil coated with $LiCoO_2$ (cathode) and copper foil coated with graphite (anode) both with approximately 0.1 mm total thickness were purchased from MTI Corporation [12]. The current collectors were made of lightweight copper tape thin films and were used for both the anode and cathode. These were bonded onto the battery electrode materials using the adhesive face of the copper. Two electrolytes were fabricated for the design using a polyethylene oxide (PEO) 100,000 Mw matrix, a semi-crystalline polymer, comprised of a combination of amorpohous and crystalline grains. One of the electrolytes contained additional 1 wt% graphene oxide (GO) to the solvent matrix, and the other contained no additional fillers to the PEO matrix. The total area of the battery was approximately 20x20 mm^2. Droplets of plasticizer, an aqueous solution of 1 M $LiPF_6$ in ethylene carbonate and dimethyl carbonate, were added to the polymer electrolyte surface to enhance interfacial contact and ionic conductivity. The flexible battery was then encapsulated between lamination sheets to hold the

layers in place. The encapsulation process included taking the battery layers of the flexible LIB and stacking them onto two plastic sheets of Scotch thermal laminating polyester. The lamination process was carried out inside a glove box. Figure 7 shows the layered configuration of the battery that was fabricated, and illustrates the battery successfully powering an LED under a bending load, provided courtesy of [11].

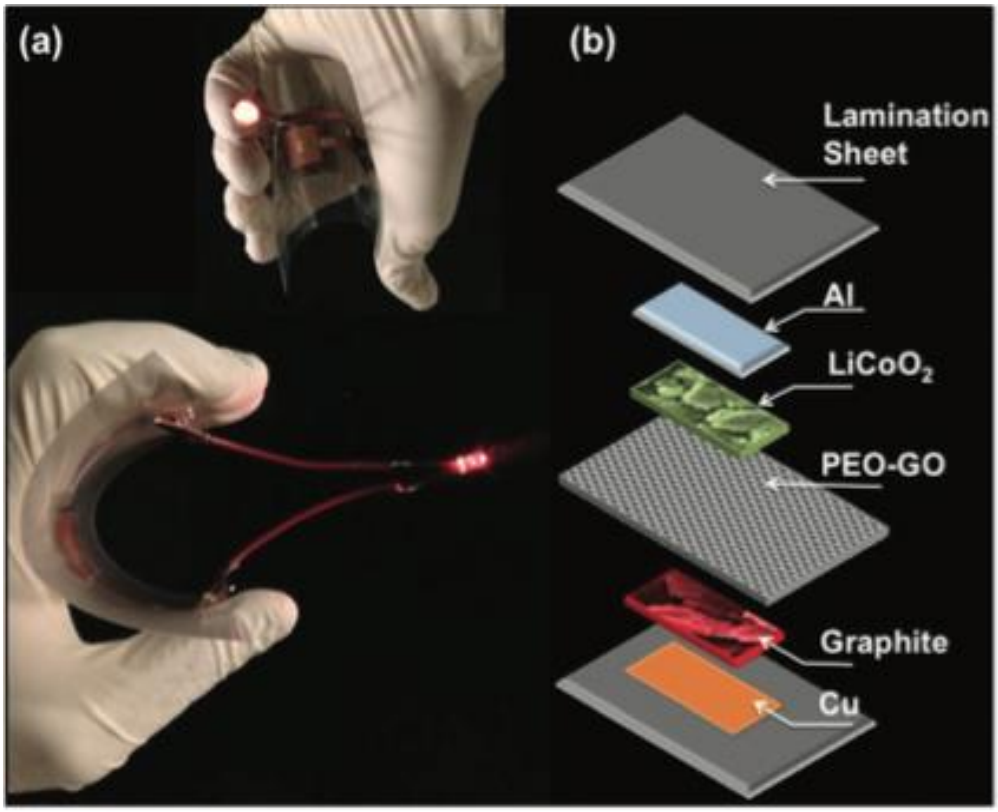

Figure 7: Images of a) a flexible Li ion battery based on solid PEO/1%GO electrolyte powering an LED, and (b) schematics of the flexible LIB materials and configuration (provided courtesy of [11]).

After fabrication, the battery performance under loading was assessed by bending the battery. The flexible battery was placed into an apparatus with ends

clamped, and an end displacement was applied to bend the battery to produce a center radius of curvature of 17 mm. The bending applied was displacement controlled and was analogous to column buckling. Figure 8 shows the bending experiment, and the bending states of the battery during the performance evaluation, provided courtesy of [11].

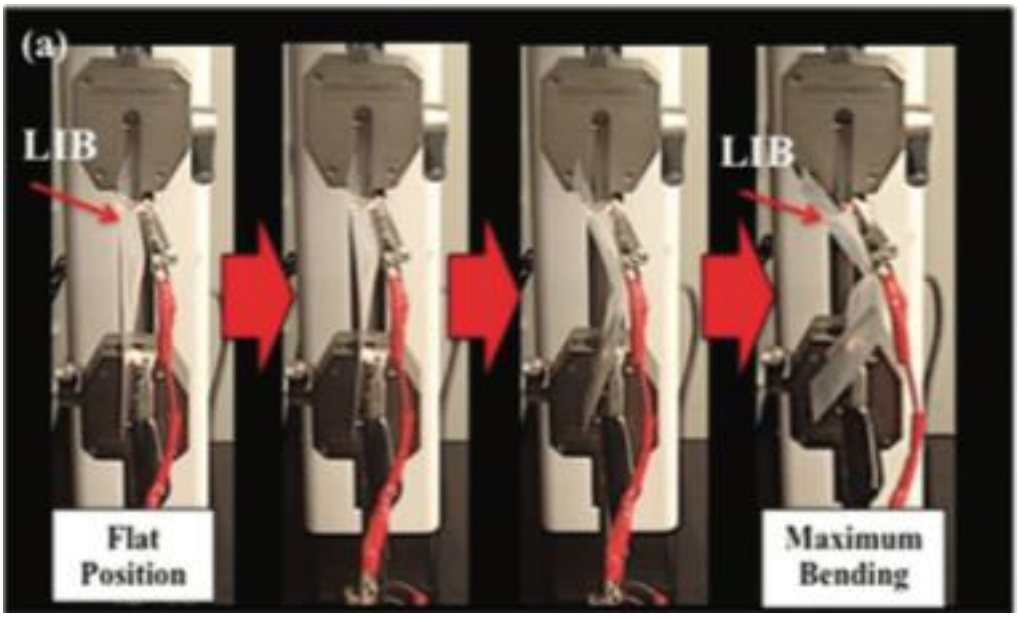

Figure 8: Flexible LIB (based on PEO/1 wt% GO electrolyte) subject to cyclic bending and in situ voltage measurements (provided courtesy of [11]).

Of particular interest in the evaluation of the battery performance is the mechanical and stress response of the battery under various states of loading. This is due to the fact that a key feature of the battery is that it is designed specifically to be subjected to mechanical loading, which will result in a state of stress in the battery. Additionally, the loading state can influence battery performance, e.g., delamination of the layers, and contact stress between the layers. The encapsulation process also induces a residual state of compression.

In addition to the experimental evaluation of the battery that was conducted, a simulation of the battery subjected to the state of bending as described in the experiment was completed. This was to conduct a more detailed evaluation of the material response of the battery, in order to evaluate parameters such as stress, strain, displacement, and contact pressure. The following sections provide the details of the analysis procedures, and a discussion of the results and the implications on battery performance.

2. Numerical analysis

The numerical simulation and analysis of the flexible battery was completed using the finite element method, in order to model the bending of the battery. Dassault Systemmes Abaqus Version 6.14 commercially available finite element software was used to evaluate the battery bending response. The following sections outline the details of the numerical analysis completed, including a description of the geometry, mesh, materials, contacts, loads, and boundary conditions.

2.1 Geometry and mesh

The geometry of the battery was modeled using the Abaqus CAE drafting capabilities. Each layer of the battery was modeled as a separate part instance, with each layer stacked initially in contact and modeled as a 20x20 mm^2 area section as shown in the configuration in Figure 7 to closely resemble the flexible battery. The thicknesses of each battery layer used in the experiment were measured and

provided as inputs. The measured thicknesses of each layer are listed below in Table 1.

Table 1: Measured thicknesses of each layer in the flexible battery used in the numerical analysis.

	Component	Type	Quantity	Thickness(mm) measured
1	Anode	Graphite	1	0.122
2	Current collector (anode)	Copper (Cu)	1	0.018
3	Cathode	$LiCoO_2$	1	0.098
4	Current collector (cathode)	Aluminum (Al)	1	0.038
5	Electrolyte 1	PEO	1	0.389
6	Electrolyte 2	PEO+1%GO	1	0.437
7	Encapsulant	Plastic seal" Scotch thermal laminating polyester sheet"	4	0.069 each layer

The geometry was meshed using a part instance dependent mesh scheme. Each layer was meshed with plane stress elements. The plane stress elements assume that the internal forces that result from applied loading or body forces are non-zero in the in-plane direction, and out-of-plane forces are assumed zero. For an isotropic material undergoing linear elastic constitutive response with zero body forces, i.e., negligible gravity forces, in a Cartesian global coordinate system, the resulting equations are as follows:

$$\begin{bmatrix} \boldsymbol{\varepsilon_{xx}} \\ \boldsymbol{\varepsilon_{yy}} \\ \boldsymbol{\varepsilon_{xy}} \end{bmatrix} = \begin{bmatrix} \frac{\boldsymbol{\partial}}{\boldsymbol{\partial x}} & \mathbf{0} \\ \mathbf{0} & \frac{\boldsymbol{\partial}}{\boldsymbol{\partial y}} \\ \frac{\boldsymbol{\partial}}{\boldsymbol{\partial y}} & \frac{\boldsymbol{\partial}}{\boldsymbol{\partial x}} \end{bmatrix} \begin{bmatrix} \boldsymbol{u_x} \\ \boldsymbol{u_y} \end{bmatrix}, \tag{21}$$

$$\begin{bmatrix} \boldsymbol{\sigma_{xx}} \\ \boldsymbol{\sigma_{yy}} \\ \boldsymbol{\sigma_{xy}} \end{bmatrix} = \frac{\boldsymbol{E}}{\mathbf{1}-\boldsymbol{\nu}^2} \begin{bmatrix} \mathbf{1} & \boldsymbol{\nu} & \mathbf{0} \\ \boldsymbol{\nu} & \mathbf{1} & \mathbf{0} \\ \mathbf{0} & \mathbf{0} & \frac{\mathbf{1}-\boldsymbol{\nu}}{\mathbf{2}} \end{bmatrix} \begin{bmatrix} \boldsymbol{\varepsilon_{xx}} \\ \boldsymbol{\varepsilon_{yy}} \\ \mathbf{2}\boldsymbol{\varepsilon_{xy}} \end{bmatrix}, \text{ and} \tag{22}$$

$$\begin{bmatrix} \frac{\partial}{\partial x} & 0 & \frac{\partial}{\partial y} \\ 0 & \frac{\partial}{\partial y} & \frac{\partial}{\partial x} \end{bmatrix} \begin{bmatrix} \sigma_{xx} \\ \sigma_{yy} \\ \sigma_{xy} \end{bmatrix} = \begin{bmatrix} 0 \\ 0 \end{bmatrix}, \quad (23)$$

where σ_{ij} is a component of stress (i=j for normal stress, i≠j for shear stress), ε_{ij} is a component of strain (i=j for normal strain, i≠j for shear strain), ν is the Poisson's ratio, and E is the modulus of elasticity. Plane stress elements were appropriate for this particular analysis since the loading was assumed to act to result in negligible out-of-plane stress in the battery. Furthermore, the plane stress elements were chosen over plane strain due to the fact that plane strain elements assume a cross-section of infinite out-of-plane thickness. Plane stress elements initially assume a zero thickness cross-section; however in this case, in order to properly model the stiffness and resulting displacement response, each layer was assigned a section with a thickness of 20 mm.

All layers except for the electrolyte were meshed with CPS4I solid continuum elements. These elements are 4 node bilinear elements with 3 degrees of freedom that are capable of evaluating displacement, stress, strain, interfacial and contact pressure, internal forces, and internal moments. Linear, full-integration elements were chosen to reduce the simulation runtime. The full-integration formulation utilizes 4 internal integration points. However, due to the lack of midside nodes, linear, full-integration elements are susceptible to shear locking without sufficient mesh refinement or the use of additional shape functions in problems involving pure bending. Shear locking is an inability of the element to model the kinematics of bending curvature to properly resolve the tension and compression sides of bending

in the element into normal stress. Rather, the result is the development of parasitic shear stress terms at the integration points. Reduced integration formulations effectively result in zero strain gradient across the element in these types of load cases. Figure 9 illustrates graphically the resulting issues of first order elements.

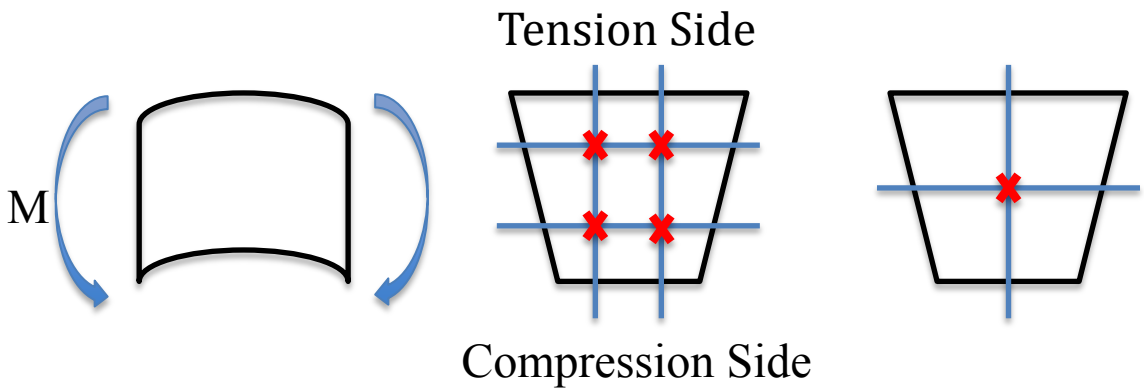

Figure 9: Graphical representation of the shape change of a) a section of beam (exact solution), b) a linear full integration formulation element resulting in shear locking, and c) a linear reduced integration formulation element.

Incompatible mode elements are full-integration elements that include additional shape functions, which eliminate the parasitic shear stresses, and result in a linear strain gradient across the element for normal strain, rather than a zero gradient across the vertical direction. The normal stresses are then interpolated across the element accordingly to the nodes.

The electrolyte was initially modeled using linear elements, but due to high compression strains that resulted from the encapsulation step in the simulation (to be discussed later), higher order quadratic elements were used instead. This was because initially the high compressive strain resulted in element distortion due to

hour-glassing of the elements, and inaccuracies in the model stiffness matrix. CPS8 elements, which are quadratic, full integration elements, were used to mesh the electrolyte, which provided the most accurate resolution of the electrolyte strain field.

2.2 Material models

Two different solid polymer electrolytes were modeled separately in two different geometric models for each PEO and PEO with 1% GO. The following assumptions were made with regard to the simulation:

- The mechanical response of the battery could be modeled using linear elastic material constitutive models, i.e., no plasticity or yielding is assumed to occur during the loading considered.
- Large deformation modeling was assumed, with deformation tensors calculated with respect to current configuration (true stress), i.e., effects due to nonlinear geometry are considered.

Material property inputs for the analysis included the modulus of elasticity and Poisson's ratio for each material. Data not available in the literature, or specific to this particular fabrication process, was obtained via mechanical testing, in this case tensile testing in the lab. Modulus of elasticity was obtained for the PEO and PEO with 1% GO by measuring the slope of the stress vs. strain curve in the elastic response region (prior to yielding). Figure 10 shows the tensile test data for PEO,

and illustrates the fit procedure used to obtain the modulus of elasticity. Table 2 lists the material inputs to the analysis for all materials in the battery.

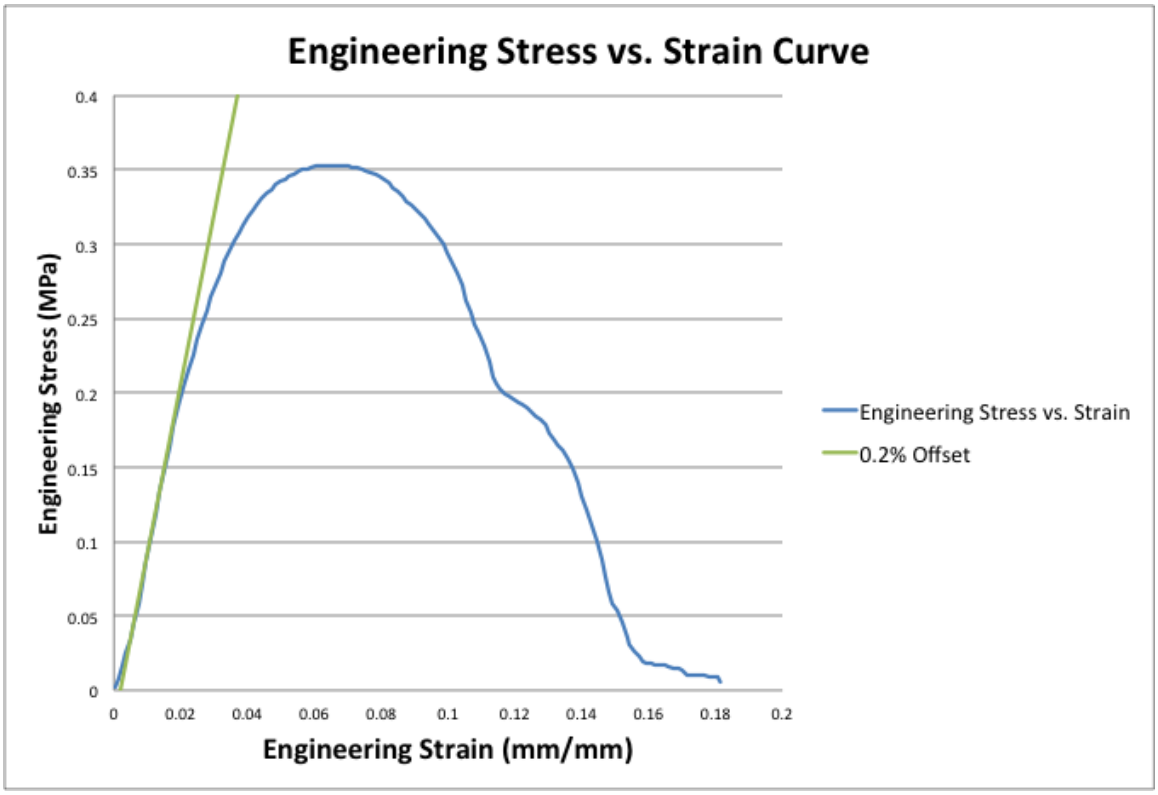

Figure 10: Plot of engineering stress vs. engineering strain, obtained from tensile testing, for polyethylene oxide (PEO), in the lab.

Table 2: Material property inputs for the finite element battery model [11].

	Component	Modulus of Elasticity (MPa)	Poisson's Ratio
1	Anode	14665	0.236
2	Current collector (anode)	117211	0.355
3	Cathode	135800	0.306
4	Current collector (cathode)	68947.6	0.334
5	Electrolyte 1	10.3	0.300
6	Electrolyte 2	33.45	0.300
7	Encapsulant	4895.3	0.380

2.3 Contact properties and layer interactions

Since each layer was modeled as a separate, individual part mating together in a stack, contact properties were defined in the model. Due to the battery fabrication, each layer was assumed in hard contact, and all layers were assumed to be held together with adhesive, except for the interfaces between the electrodes and the electrolyte. This is consistent with the fact that the electrodes are deposited onto the current collectors and the battery is thermally encapsulated. However, the electrolyte/electrode properties were assumed to be in frictionless contact. This simulates an "unbounded" interface with free slip, e.g., very low friction, and is one possible contact property that could result during the battery function. Other interfacial properties were considered in a different battery model, which will be discussed in Chapter III.

In order to simulate the adhesive condition, multipoint constraints, or "tie" constraints, were defined at each layer interface. The interface between the electrolyte and the electrodes were modeled with a frictionless contact definition utilizing a node-to-surface contact formulation. Initially a surface-to-surface contact formulation was considered for the electrolyte/electrode contact interface; however, this resulted in a condition where the slave surfaces penetrated too far into master surfaces, adversely influencing the contact pressure and stress measured at these interfaces. This is thought to have occurred because of how the contact stress changes along the length of the battery during bending, and the fact that surface-to-surface formulation tends to have an averaging effect over the local nodal contact stresses. This averaging affects how the contact normals are defined and maintained as the load is incrementally increased. Since the layer deflections are coupled to one another, if too much penetration occurs, there is an error in the layer deflections. Consequently the contact pressure and stress that is measured along the length of the battery loses accuracy. Since the node-to-surface formulation results in individual nodes identifying contact normals with a target surface (slave surface), the local contact pressure, and subsequently the kinematics of the problem, can be more accurately represented with this formulation. This is important since the initial lamination process results in an initial state of high compression and a large geometry change, which is more accurately captured by the consideration of nonlinear geometry. Figure 11 illustrates the interfaces that were considered in the analysis, defined as either multipoint constraints/ties, or contact pairs.

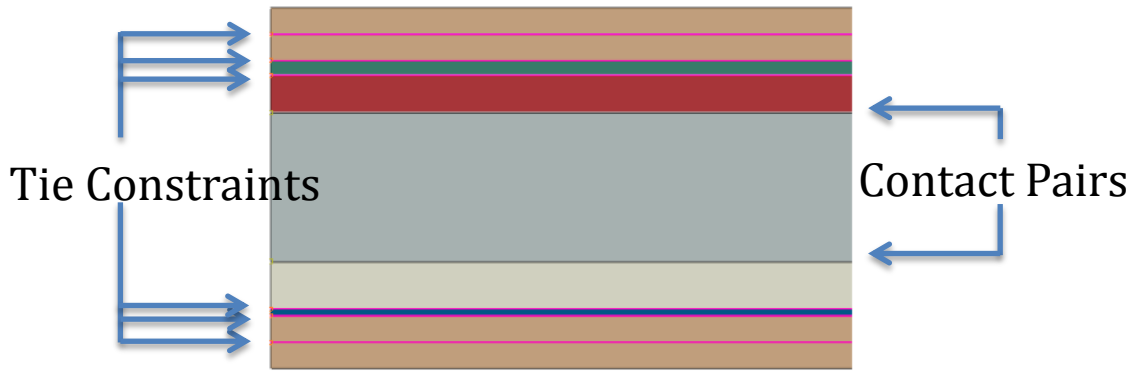

Figure 11: Layer contact definitions that show layers modeled with tie constraints, and with contact pairs.

2.4 Loads and boundary conditions

The simulation separates the various loads out by modeling each load individually in different steps. In a linear-elastic stress analysis, by modeling the loads sequentially in steps, the full stress state can be accounted for in the simulation via superposition of stress. The simulation starts by modeling the lamination/encapsulation process, which is followed by bending, and is outlined in detail in the following paragraphs.

As stated, the lamination/encapsulation of the battery results in a state where initial compressive stresses are present in the battery layers. After the lamination process of the battery, the final thickness of the battery regardless of electrolyte was measured to be 0.75 mm due to the type of laminator used. In the finite element analysis, the encapsulation is modeled using multiple steps where the battery is compressed in the initial steps of the analysis using a combination of displacement and surface pressure to a final thickness in the battery of 0.75 mm. Following the

displacement compression step, the contact force between the electrode and electrolyte layers was measured in the model, and the contact pressure required to produce this force was calculated based on the cross-sectional area of the battery. A surface pressure was applied corresponding to this condition, in order to maintain the battery thickness, since a fixed displacement boundary condition in the model would not allow for proper simulation of the bending. Following the application of surface pressure to maintain the thickness of 0.75 mm, the thickness was measured to verify that the lamination process results in the correct final compression state of the battery.

The bending of the battery was carried out following the encapsulation process in order to account for the real effects associated with the lamination compression. In the same manner as the experiment, bending was applied as a “column” load; that is, a displacement was applied axially to the battery and parallel to the orientation of the layers to cause the battery to deflect in a buckling manner. The column displacement was such to produce a bending radius of 17 mm at the center of the battery at the neutral axis of the electrolyte, to match the experiment. The bending radius was measured locally in the model by approximating the local nodal displacements and slopes as shown in Figure 12.

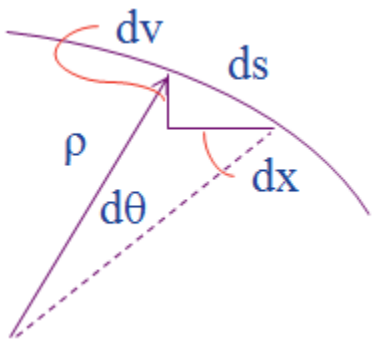

Figure 12: Geometric representation of the flexible battery undergoing large deflections.

Taking measurements locally from the center of the model, the bending curvature, κ, which is the inverse of the radius of curvature, ρ, was calculated as

$$\boldsymbol{\kappa} = \frac{\mathbf{1}}{\boldsymbol{\rho}} = \frac{\Delta\left[\tan^{-1}\left(\frac{\Delta v}{\Delta x}\right)\right]}{\Delta s}. \qquad (24)$$

The boundary conditions applied to the model were such to simulate a simply support beam, since the battery under bending loads in this case resembles that of a simply supported beam. At one end opposite to the bending displacement, the node at the bottom end of the battery was fixed in all degrees of freedom. At the opposite end, where the bending displacement was applied, only the vertical degree of freedom was constrained, to allow free movement of the end during buckling displacement.

3. Results and discussion

The bending of the battery was simulated using Abaqus 6.14 Standard solver, which is a robust solver capable of accurately solving implicit static mechanics problems, which is how the battery bending problem was analyzed. Both flexible batteries (each containing the different electrolytes) that were simulated were analyzed for the same load case, which included the following steps:

1. Lamination displacement to produce final battery thickness of 0.75 mm.
2. Lamination pressure to maintain final battery thickness of 0.75 mm.
3. Apply end displacement to bend battery until a center curvature of 17 mm is reached.

Figure 13 and Figure 14 show a plot of the stress distribution associated with the encapsulation process for the PEO and PEO with 1% GO, respectively. Figure 15 and Figure 16 plot the contact pressure between the electrolyte/anode and electrolyte/cathode layers along the length of the battery for the PEO and PEO with 1% GO electrolytes, respectively. The contact pressure and contact stress is higher for the PEO with 1% GO, since the electrolyte is stiffer and requires greater force to compress the battery to a final thickness of 0.75 mm.

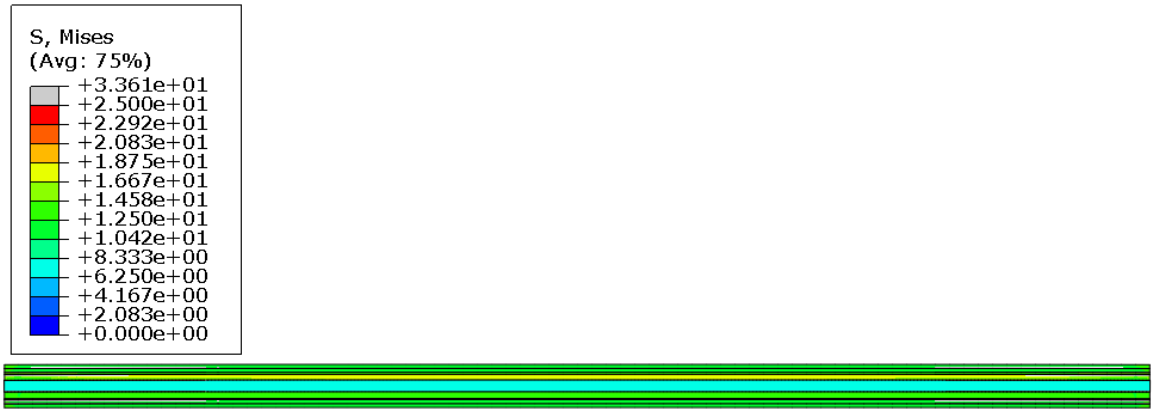

Figure 13: Stress plot of the battery after encapsulation with the PEO electrolyte.

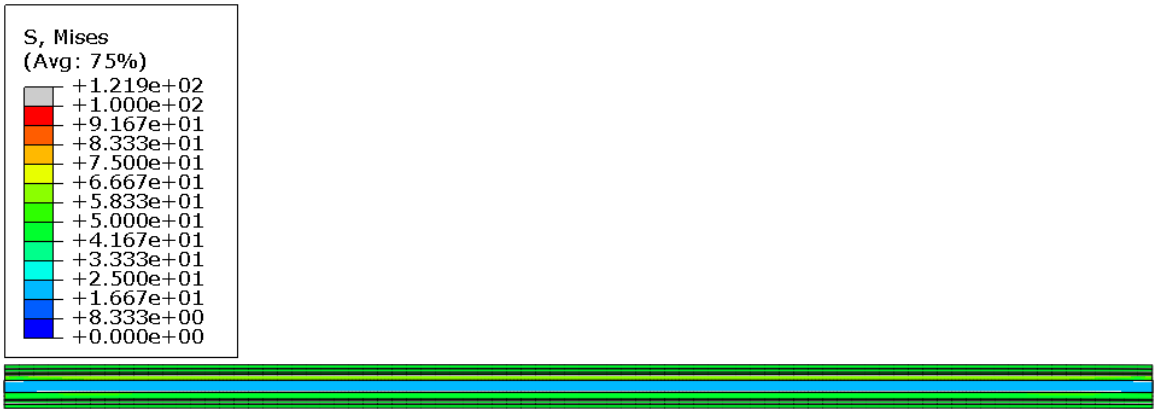

Figure 14: Stress plot of the battery after encapsulation with the PEO+1%GO electrolyte.

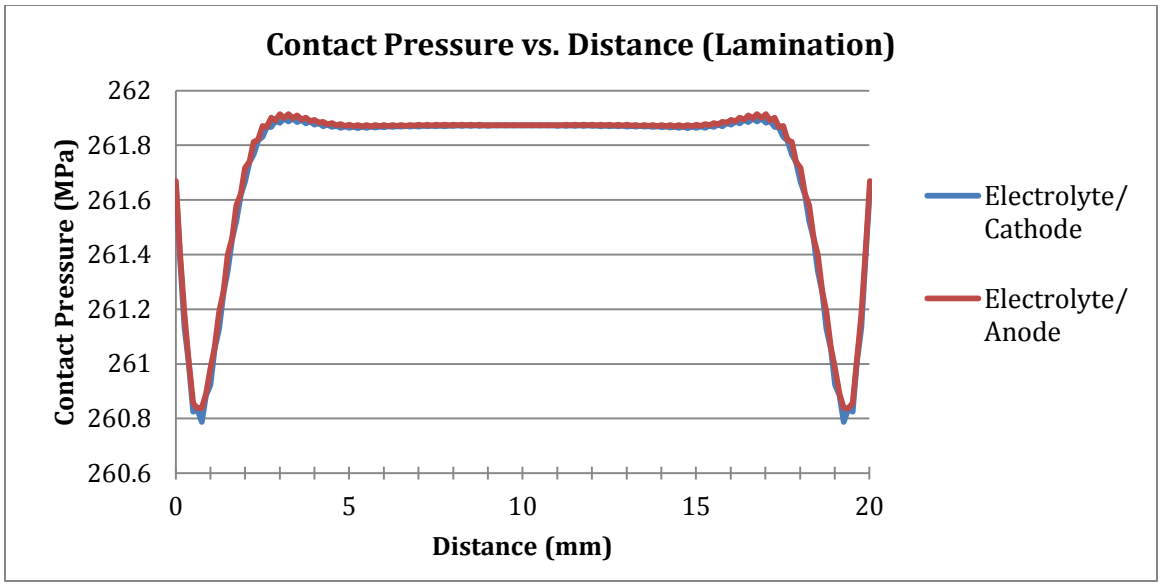

Figure 15: Plot of contact pressure (MPa) vs. position distance (mm) between the electrolyte/cathode and electrolyte/anode after encapsulation for the battery with the PEO electrolyte.

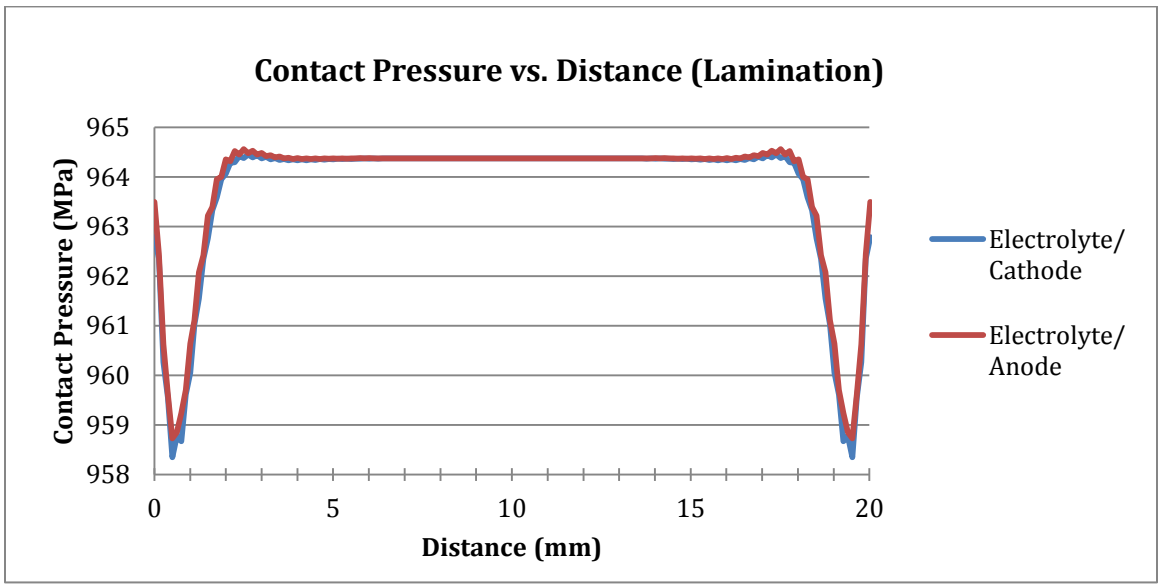

Figure 16: Plot of contact pressure (MPa) vs. position distance (mm) between the electrolyte/cathode and electrolyte/anode after encapsulation for the battery with the PEO with 1%GO electrolyte.

Figure 17 provides a visual for the limit criteria envelope used to describe the von Mises stress, along with the Tresca limit criteria. Stress plots of the battery bending that additionally illustrate the curvature of the battery are shown in Figure 18 and Figure 19 [11]. Figure 18 shows the von Mises equivalent stress in the battery, which is a scalar value and is a deviatoric stress based on the second invariant of the stress deviator tensor. This value is associated with the distortion energy theory, a failure theory used to predict the onset of yielding in engineering materials. The von Mises stress is given by

$$\boldsymbol{\sigma_{VME}} = \sqrt{\frac{(\sigma_{11}-\sigma_{22})^2+(\sigma_{22}-\sigma_{33})^2+(\sigma_{11}-\sigma_{33})^2+6(\sigma_{12}{}^2+\sigma_{23}{}^2+\sigma_{13}{}^2)}{2}}. \tag{25}$$

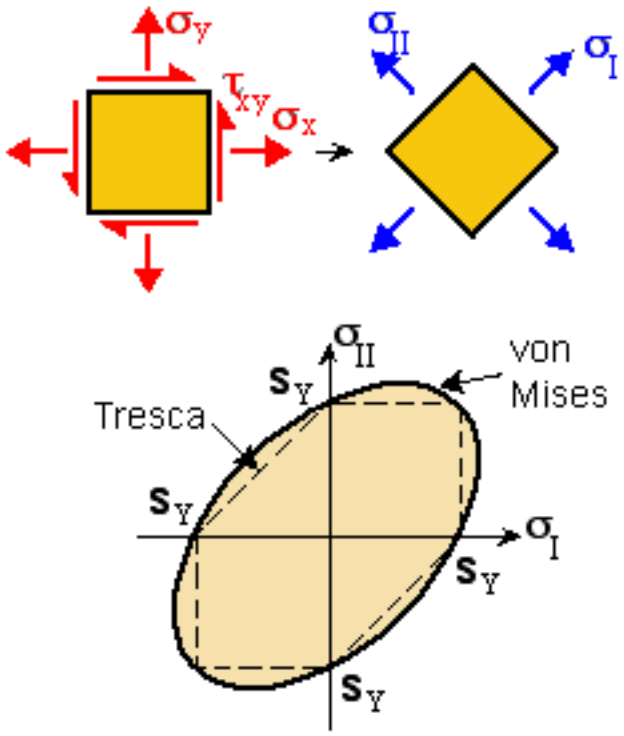

Figure 17: von Mises failure ellipse as a plot of in-plane stress (courtesy of A. Hancock College).

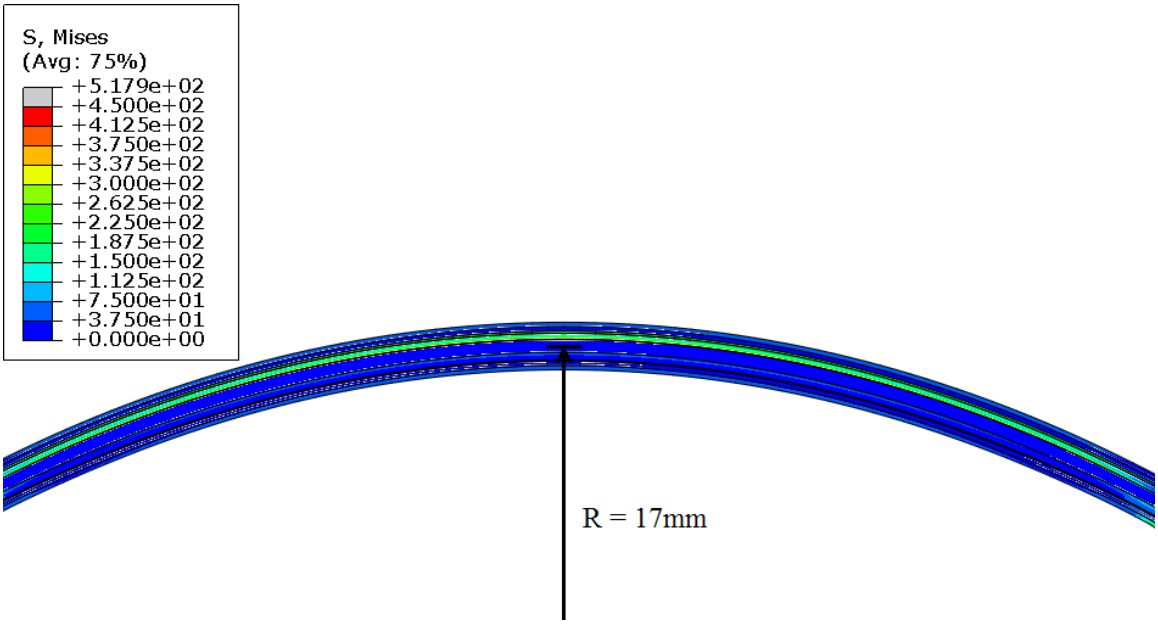

Figure 18: Plot of the bending radius curvature modeled in the battery finite element model [11].

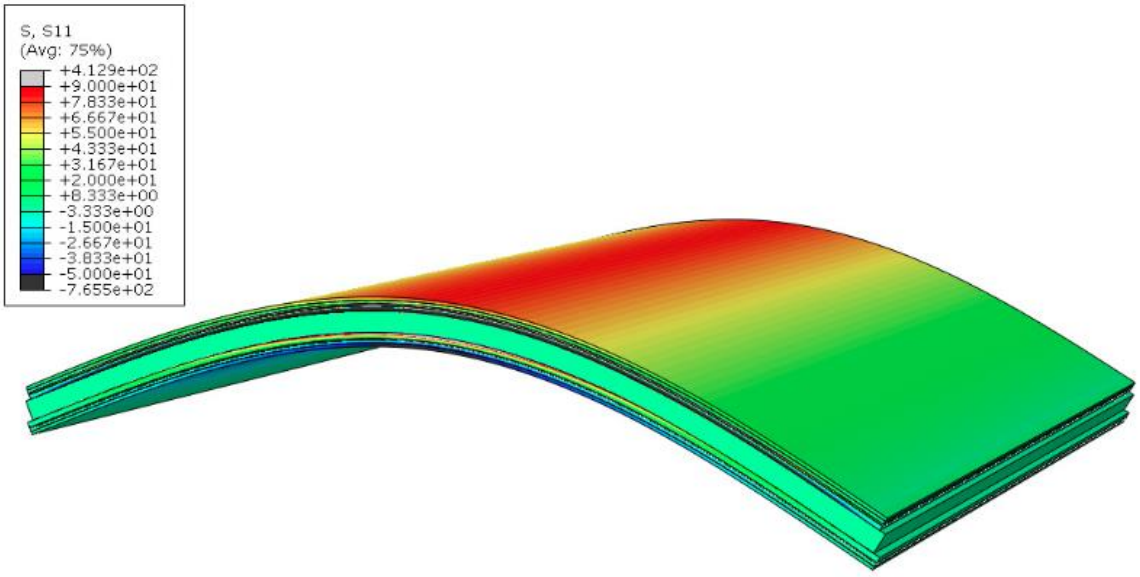

Figure 19: Contour plot of the stress distribution of the battery during bending: longitudinal component of stress plotted to illustrate bending stress [11].

Plots of the contact pressure between the electrolyte/cathode and electrolyte/ anode are shown for the in Figure 20 and Figure 21 for the PEO and PEO+1%GO electrolytes, respectively. As observed experimentally, the contact pressure is predicted to increase as bending is applied to the battery. Furthermore, no delamination is predicted to occur for a bending radius of 17 mm.

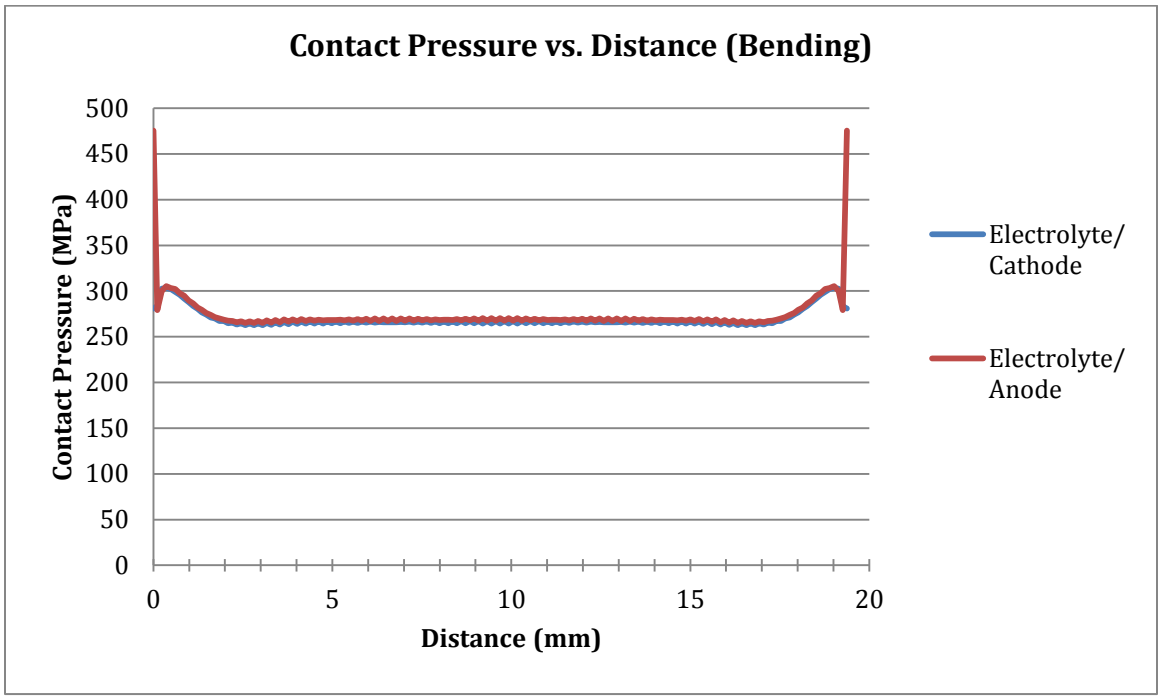

Figure 20: Plot of contact pressure (MPa) vs. position distance (mm) between the electrolyte/cathode and electrolyte/anode after encapsulation and bending for the battery with the PEO electrolyte.

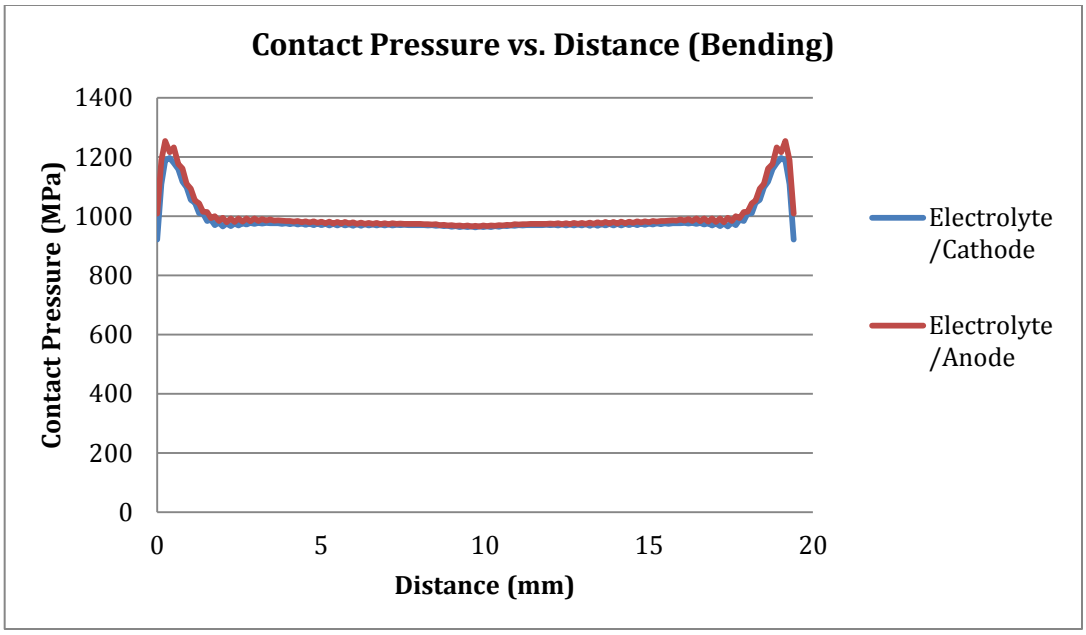

Figure 21: Plot of contact pressure (MPa) vs. position distance (mm) between the electrolyte/cathode and electrolyte/anode after encapsulation and bending for the battery with the PEO+1%GO electrolyte.

In addition to evaluating the contact pressure at a single bending curvature, the contact pressure was evaluated for multiple radii of curvature. The average of the contact pressure was calculated for multiple curvatures and plotted in Figure 22 [11]. It is important to note that the end effects, which produce higher contact pressures locally than throughout the rest of the battery length due to end stress concentration effects, were neglected in the averaging calculation. As can be seen from the plot, the contact pressure increases and follows an exponential trend.

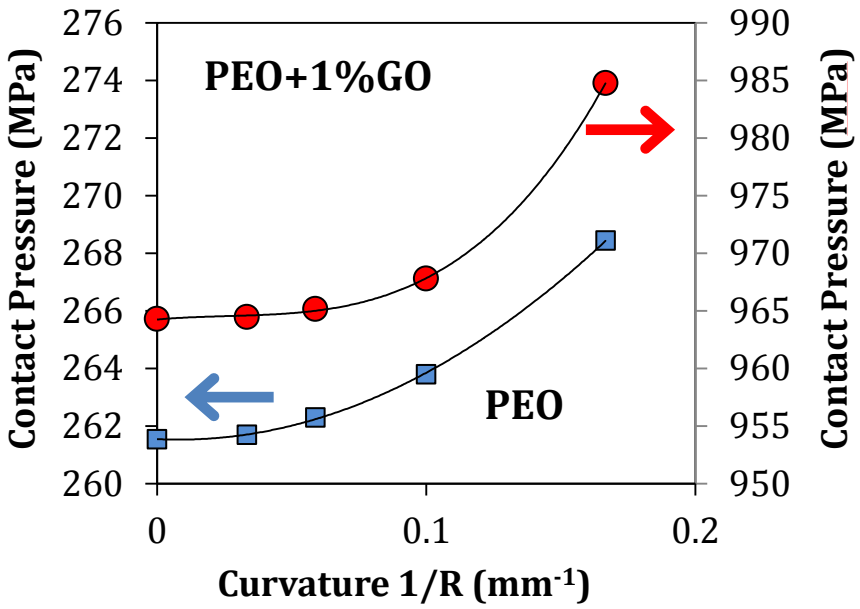

Figure 22: Average contact pressure between electrode/electrolyte layers for various bending curvatures [11].

It was observed during the bending experiment that battery performance improved, specifically that the impedance decreased, for larger curvature and smaller radius of bending. This is an important find and thought to be due to the fact that as bending increases, contact pressure between the electrolyte and the electrodes increases, which is confirmed numerically. This results in improved contact conductance, and a decrease in impedance, which will be discussed in greater detail in Chapter III.

The following chapter goes deeper into the relationship between bending and contact pressure to determine a direct modeling relationship between the two quantities. The influence of additional parameters on this relationship, including

interfacial contact properties between the electrolyte and the electrodes, the manner of bending, and the connection to impedance, are further evaluated.

Chapter III Models Relating Contact Pressure and Mechanical Response to Predict Performance in a Flexible SPE LIB

1. Continuation of previous modeling with enhancement

In this chapter, the previous modeling efforts are expanded upon by exploring more deeply the relationship between contact pressure, bending, and the influence of the contact properties at the interfaces between the electrodes and the electrolyte. An analytical framework is developed to model the mechanical response of the multilayer flexible battery structure by first considering a linear approach, and then applying a more novel approach to address nonlinearity due to large bending deflections. These are both addressed by considering small displacement and large displacement assumptions, which will be discussed in more detail. The battery was treated as a hypothetical multilayer simply supported beam comprised of n layers subjected to an applied external load. The influences of interfacial contact properties and loading are accounted for in the closed-form solutions of the system to ultimately obtain the contact pressure between the layers. The equations from the analytical model were solved numerically, and further evaluation was completed using the previously developed finite element model, which included a few enhancements. The contact pressure between the electrode/electrolyte layers was obtained for a series of varied inputs, including bonding between layers, friction,

and method of bending, and each iteration was plotted as a function of bending curvature. After the modeling efforts were completed, the flexible SPE LIB was fabricated and tested in a bending application in our lab, and the change in battery impedance with increased bending was measured. This data was compared with the contact pressure calculations obtained numerically. Both data sets follow a similar exponential trend and show good agreement.

2. Analytical development

As previously described a common design for many flexible batteries, including the one developed in our laboratory and discussed in the previous chapter, resembles a multilayer composite beam. Therefore, the mechanical response of these types of batteries under loading mimics a simply supported composite beam subjected to mechanical loading. Bending of the flexible battery was found to affect battery performance, specifically impedance, with increased bending. This was hypothesized to be the result of increased contact pressure between the battery layers due to the input loading, specifically between the electrode and electrolyte layers. Therefore, of particular interest in the development of this analytical framework was the relationship between the battery mechanical response and the contact pressure between the electrode/electrolyte layers. By understanding this mathematically relationship, battery performance can be predicted and anticipated, which would be an important understanding in design for various applications.

In evaluating the mechanical response of the flexible battery, since the battery is specifically designed to take large bending deflections, nonlinearity associated with this condition needs to be addressed. Multiple approaches can be taken to develop a model that governs the mechanical stress and deflection response of the battery. The first approach considered, termed the small displacement approach, assumes that the deflection and curvature in the battery, treated as a structural beam, are so small that their changes are visually unnoticeable to an observer. This simplifies the equations of motion, and is a common assumption for more rigid structures such as steel I-beams in buildings, and reinforced concrete bridges [215]. This generally results in a linear fourth order differential equation, where the solution results in a closed-form deflection equation that takes the form of a polynomial. The second method, termed the large displacement approach, removes the "small" deflection assumption, which results in more complex equations that require numerical methods in order to obtain solutions [216]. The latter method is of particular interest for the present study of flexible battery mechanical response since SPE flexible batteries are designed to experience high bending displacements. This is because the SPE is a polymer capable of large displacement response under bending due to polymer chain motion and extension of amorphous grains, and therefore accounting for large displacement response may be necessary. In this framework, a more novel approach is taken to model the system as a system of nonlinear differential equations in terms of the angle of beam deflection, rather than the vertical beam deflection.

The mechanical response of beam structures under applied loading is well known, and previous studies have evaluated deflections of multilayer beam structures [217-219]. While multilayer structures have been studied, the main focus has been on applications related to more rigid structures applying the "small displacement" approach. This is because in structural materials such as concrete and steel, which are widely used, the mechanical response because of their material properties is limited to small elastic deformations. Far fewer studies have focused on evaluating large deflections of beams and nonlinearity. Jasem showed the nonlinear effect of layer thickness and material stiffness on composite beam deflection [220]. Additionally, early attempts at understanding the contact pressure between simple unbonded layers focused on stiff elastic structures; however, these studies assumed small displacements between stiffer yet deformable bodies against rigid surfaces [221-223]. Dempsey and Li studied frictionless contact between a Timoshenko beam and a thick elastic surface [224]. Belendez et al considered small and large deflections for cantilever beams, identifying a key nonlinear relation; however, this study focused only on single beams and not multilayer beam loading problems. [225]. To the best of our knowledge, no studies have been found that combine large displacement beams behavior to evaluate contact pressure between layers of a multilayer structure that are well-suited to evaluate the battery problem.

2.1 Conceptual model of multilayer structure

In order to start the modeling efforts, the flexible battery is first assumed to be a multilayer beam made up of n layers, each with a prismatic cross-section as shown

in Figure 23 [226]. This resembles the flexible SPE LIB that was designed in our laboratory. The prismatic cross-section contains parameters of t, A, E, and I, which represent the thickness, cross-sectional area, modulus of elasticity, and geometric moment of inertia. These are all important parameters that play into the kinetics of the bending problem. This multilayer structure is held together with a lamination surface pressure, p_0, applied on the top and bottom layers of the structure. This is intended to prevent delamination of the layers under mechanical loading.

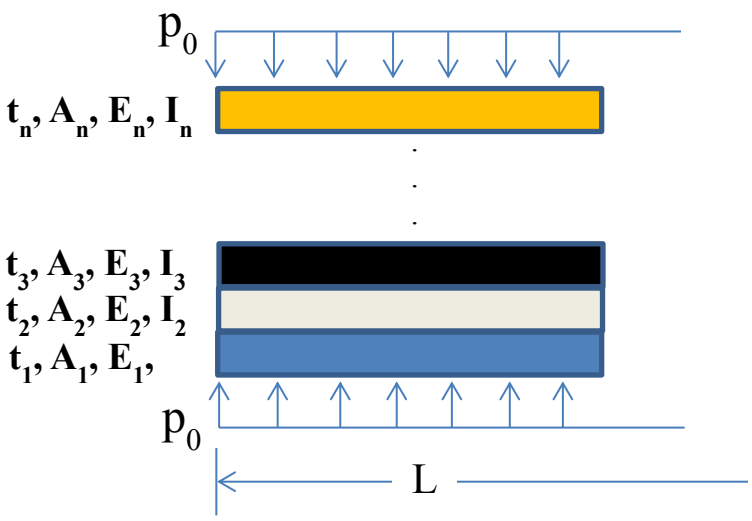

Figure 23: Conceptual multilayered structure illustrating n layers [226].

The multilayer structure is assumed to be constrained in the same manner as shown in Figure 24 [226], with a transverse shear force applied at the midpoint of the beam, vertical reaction forces at either end of the beam as shown, and a horizontal reaction force at the center of the beam. The problem is slightly modified from a simply supported beam to this condition, and symmetry of the beam is assumed with the horizontal force at the beam center. This condition is reflected in the finite

element modeling to be discussed in this chapter. The transverse shear force is assumed to act along the length of the beam as an impulse function, δ(s-L), where s is any point along the length of the beam, L. The contact pressure profile between each layer is represented by an arbitrary function, $p_i(s)$.

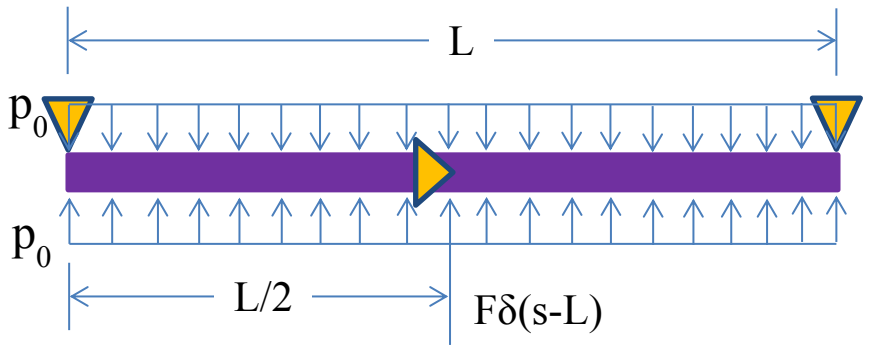

Figure 24: Free body diagram of the composite beam structure [226].

2.2 Interfacial contact properties

Regarding the mechanical response of the SPE flexible battery, it is important to consider the properties at each layer interface. In other words, bonding or adhesion strength, if any, at interfaces can cause sticking, sliding/slipping, or delamination behavior between the battery layers. Typically the fabrication process of a flexible battery can result in bonding or adhesion between the layers, which can affect the battery deflection profile under bending as well as the force balance and stress in each layer. The resulting contact pressure is highly dependent on the contact pressure between the layers within the composite multilayer structure. The interfacial properties in the multilayer flexible battery can be considered to be one of the following:

- A strongly bonded condition, which is a sticking condition where no delamination is permitted.
- An imperfectly bonded condition, where some slip between the layers can occur.
- An unbonded condition, where layers are free to slide and delaminate.

Figure 25 illustrates the nature of each interfacial condition [226]. The fabrication process for the battery in our lab results in a lamination pressure that holds the layers together during operation. Therefore the assumption is that sufficient lamination pressure is provided to prevent delamination. The strongly bonded and the unbonded cases are considered for this study. The fabrication process also results in some bonding between the battery layers, and the unbonded case typically occurs when the bond between adjacent layers is broken due to excessive shear. The impact of the tangential properties (sticking vs. sliding) directly impacts the contact pressure.

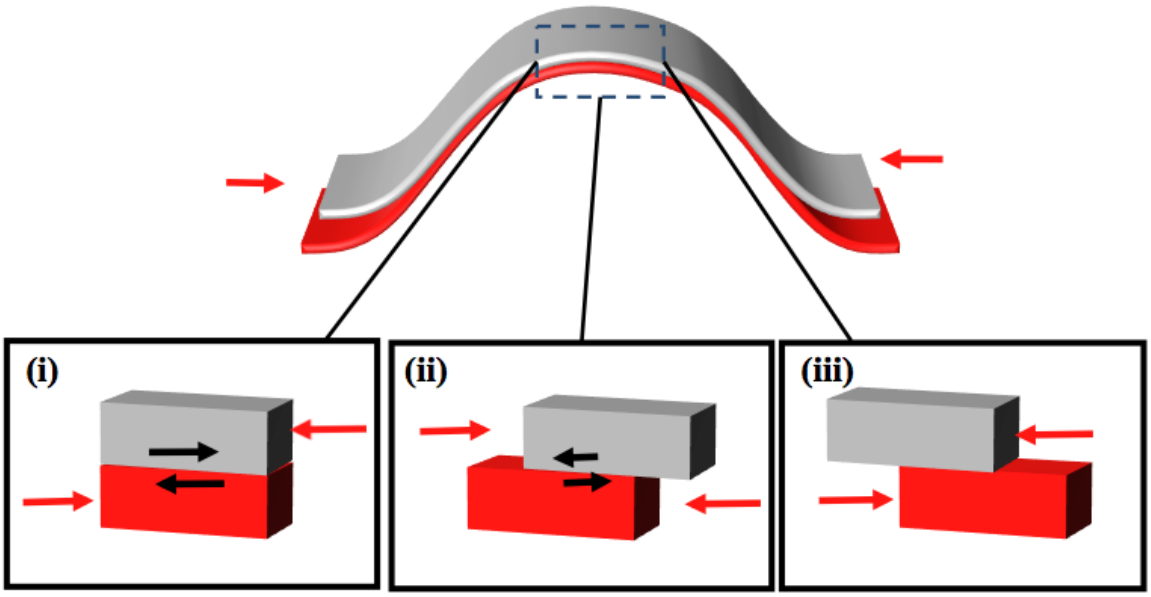

Figure 25: Interfacial properties illustrating i) a strongly bonded, ii) an imperfectly or "weak" bonded, and iii) an unbounded [226].

2.3 Small displacement development

Referring to the conventions in Figure 12, applying the small displacement assumption results in the approximation that $s \approx x$ since $\tan(\theta) \approx 0$, where θ is the angle of beam deflection. This assumption is convenient because s is interchangeable for x, simplifying the calculation of curvature to terms of x and v only. In order to determine the vertical displacement of the beam section, an infinitesimal section of the layered structure is considered as shown in Figure 26 [226]. The resulting contact pressure and interface traction functions, $p_i(x)$ and $\gamma_i(x)$, are assumed arbitrary as shown in Figure 27 [226].

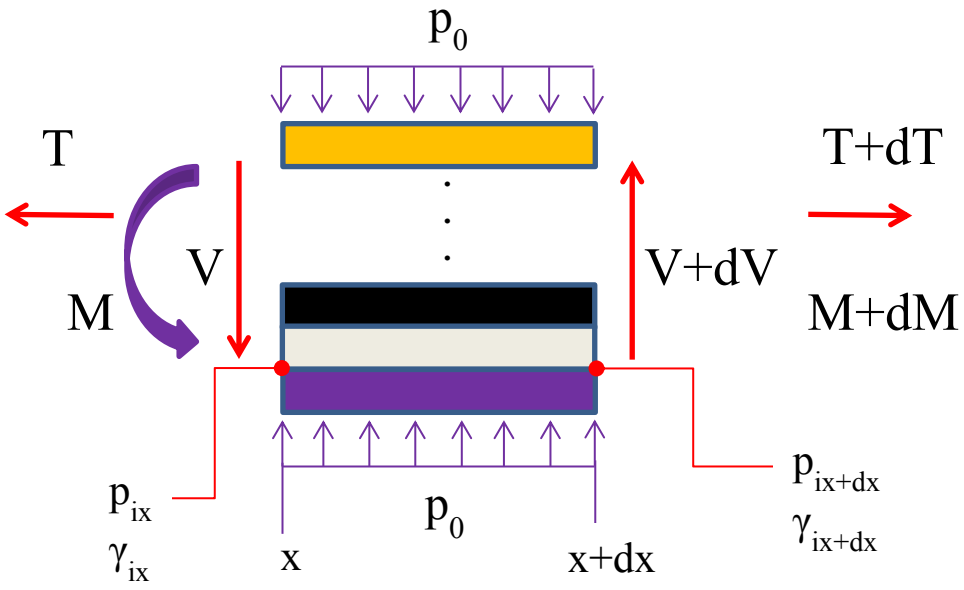

Figure 26: An infinitesimal section of the multilayer beam [226].

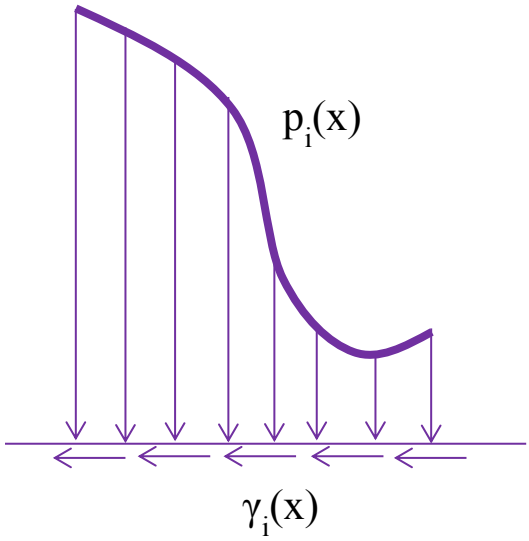

Figure 27: An assumed resulting contact pressure and interface traction functions, $p_i(x)$ and $\gamma_i(x)$ [226].

Applying force balances on the structure and individual layers yields the following:

$$\frac{dV}{dx} = \boldsymbol{F\delta(x - L)} \text{ and} \qquad (28)$$

$$\frac{dT_i}{dx} = \gamma_i(x) + \gamma_{i-1}(x). \quad (27)$$

The input force, F, in this case is represented as an impulse, which is multiplied by the Dirac delta function, V is the shear force in the beam, and T is the horizontal force in each layer. The interface traction, $\gamma_i(x)$, at each layer interface is dependent on the contact properties between the layers. The tangential conditions for sticking (strongly bonded) vs. slipping (unbonded) are given by

$$\gamma_i(x) = \begin{cases} \gamma_i(x, \varepsilon_A) \leq \gamma_c; & \textbf{Sticking} \\ \mu p_i(x); & \textbf{Slipping}. \end{cases} \quad (28)$$

In the slipping case, the resulting interface traction is due to friction, dependent on coefficient of friction, μ, and contact pressure between the layers. In the strongly bonded case the resulting traction load is related to the amount of strain, ε_A, that is arrested by constraint of the adjacent layer. A detailed stress-based analysis would be required to determine the relationship to force, and is of interest in a future study. The unbonded case occurs when the bonding between the layers is broken due to excessive shear.

The following equations show the constitutive relations for each parameter in the multilayer battery structure:

$$V = \frac{dM}{dx}, \quad (29)$$

$$M_i = E_i I_i \frac{d^2 w_i}{dx^2}, \quad (30)$$

$$M = \left(\sum_{i=1}^{n} E_i I_i\right) \frac{d^2 w}{dx^2} + \sum_{i=1}^{n} (t_i/2)[\gamma_i(x) + \gamma_{i-1}(x)], \quad (31)$$

$$\frac{d^2}{dx^2}\left[\left(\sum_{i=1}^{n} E_i I_i\right)\frac{d^2w}{dx^2} + \sum_{i=1}^{n}(t_i/2)[\gamma_i(x) + \gamma_{i-1}(x)]\right] = F\delta(x - L), \text{ and} \quad (32)$$

$$w(x) = \psi G_v(x). \quad (33)$$

The total moment, M, in the beam at any point is the sum of each layer's net bending moment, which includes the layer curvature and the interfacial properties that generate forces in the layer a distance of t/2 from the neutral axis at the top and bottom of the layer. Furthermore, the vertical deflection of all beams is equal, and for this loading can be assumed to follow a Green's function. In order to obtain an expression that directly includes the contact pressure between the layers, we consider the deflection in the bottom layer given by

$$\frac{d^2}{dx^2}\left[(E_1 I_1)\frac{d^2 w_1}{dx^2} + (t_1/2)\gamma_1(x)\right] - F\delta(x - L) = p_0 - p_1(x). \quad (34)$$

Equation 34 shows a direct relationship between the vertical deflection, input load, interface properties and the contact pressure function. In order to determine the contact pressure functions for the remaining layers, we apply a force balance to each of the remaining layers, as given by

$$\int_0^L [p_{i+1}(x) - p_i(x)]dx = 0; \quad 2 \le i \le n - 1 \text{ and} \quad (35)$$

$$\int_0^L x[p_{i+1}(x) - p_i(x)]dx = 0; \quad 2 \le i \le n - 1. \quad (36)$$

The resulting system of equations for the multilayer beam can now be solved using numerical methods to determine the mechanical response of the system under loading that would produce small displacements in the beam. Using this model, the contact pressure can be calculated at any layer interface in the composite. While the

contact pressure in each layer interface may vary slightly due to differences in contact pressure area, the average contact pressure for all layer interfaces remains equal, assuming the same contact properties exist at each layer interface. This is true since the force balance at any layer must be satisfied [226].

2.4 Large displacement development

For flexible batteries, the expected applications would produce large displacements rather than small displacements, since the battery materials are typically selected to allow the battery to withstand large displacements during operation, as discussed previously. In order to capture the full spectrum of loading within the composite structure, which includes the large displacements experienced by flexible batteries, these equations must be modified to account for nonlinearity. We must assume s to be the true value along the length of each beam layer, and remove the small angle assumption. The constitutive equations, the basis from which they are derived from the small displacement approach, are shown as

$$\boldsymbol{\rho d\theta = ds} \text{ and} \tag{37}$$

$$\boldsymbol{M_i = E_i I_i \frac{d\theta_i}{ds}}. \tag{38}$$

Considering the same loading as for the small displacement development, we evaluate the resulting deflection at a particular point of interest in the beam. By reorienting the coordinate system locally to make the variable, s, the horizontal, and plugging in the new constitutive equations, we can transform to the following:

$$\frac{d^2}{ds^2}\left[\left(\sum_{i=1}^{n} E_i I_i\right)\frac{d\theta}{ds} + \sum_{i=1}^{n}(t_i/2)[\gamma_i(s) + \gamma_{i-1}(s)]\sin(\theta)\right] - F\delta(s-L)\cos(\theta) = 0 \text{ and} \quad (39)$$

$$\frac{d^2}{ds^2}\left[(E_1 I_1)\frac{d\theta_1}{ds} + (t_1/2)\gamma_1(s)\sin(\theta_1)\right] - [F\delta(s-L) - p_0 + p_1(s)]\cos(\theta_1) = 0. \quad (40)$$

It is important to note that the resulting third order differential equations in the large displacement system have a nonlinear dependence on the dependent variable, θ, and require numerical methods to obtain a solution. Similar equations can be developed for each type of bending problem, and a relationship between the input load, contact pressure, interface properties, and deflection profile can be obtained.

3. Numerical modeling

The finite element model that was created previously, discussed in Chapter II, was again used to simulate the flexible battery in various bending states, with modified interfacial conditions. In this model, only the PEO electrolyte was considered for the materials model, and material properties for PEO were defined accordingly. Figure 28 illustrates the layers in the finite element model [226].

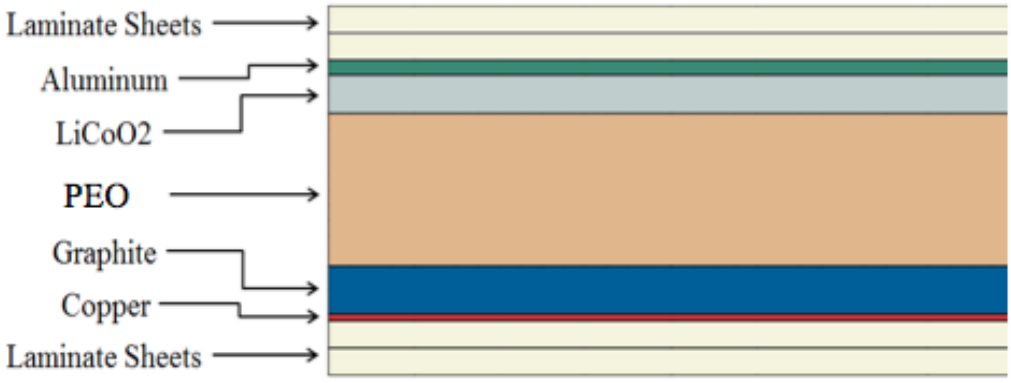

Figure 28: Layer sequence defined in analytical and numerical models [226].

3.1 Comparison of interfacial contact properties

A single method of bending was used as a basis for comparing the influence of the interfacial properties in the analytical framework, as previously discussed. Three different interface properties between the electrode/electrolyte layers were defined and evaluated for the input shear load: a sticking condition corresponding to a strong bond, and unbonded contact with friction and frictionless conditions. The remaining layers were assumed to have a strong bond at their interfaces. As modeled previously, the strongly bonded condition was modeled with multipoint constraints, or "tie" constraints, that were defined at each layer interface. For the unbonded interfacial cases, contact pairs were defined between the electrolyte and the electrodes, which were modeled with a contact definition utilizing a node-to-surface contact formulation. The frictionless case was simply defined with a "frictionless" definition, while the frictional case was modeled using the penalty method and an assumed friction coefficient of 0.3.

A shear force was applied at the midpoint of the battery to displace it a vertical distance of 0.3 mm and 3 mm at the center. Figures 29 and 30 [226] show the resulting contact pressure profiles along the normalized length of the battery, away from the influence of end effects, at the cathode/electrolyte interface. Additionally, the equations from the large displacement analytical framework were numerically solved to obtain the contact pressure profile at the cathode/electrolyte interface for the frictionless unbonded interface condition at 0.3 mm displacement. The contact

pressure function obtained from solution of the differential equations shows good agreement with the finite element simulation in Figure 31 [226].

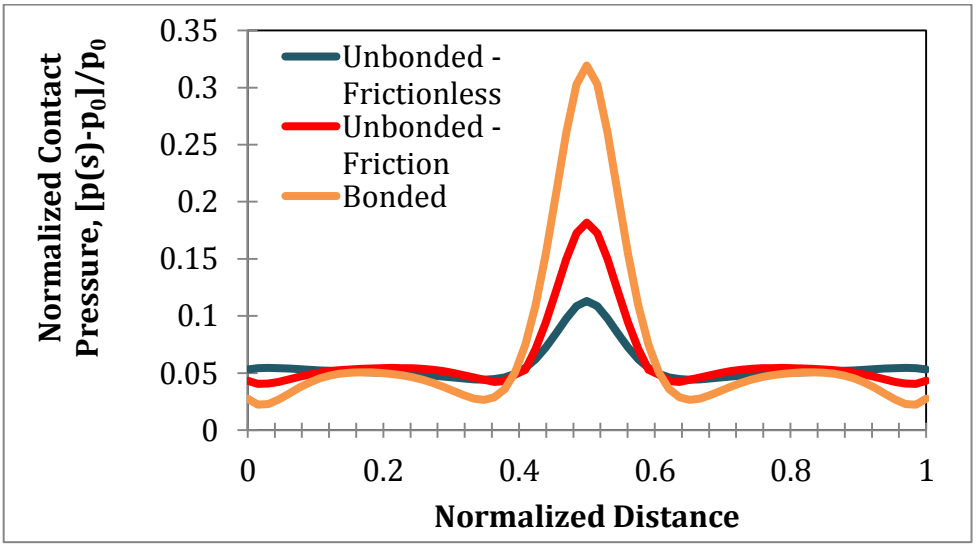

Figure 29: Resulting contact pressure profiles from simulation of three different interface properties with center displacement of 0.3 mm [226].

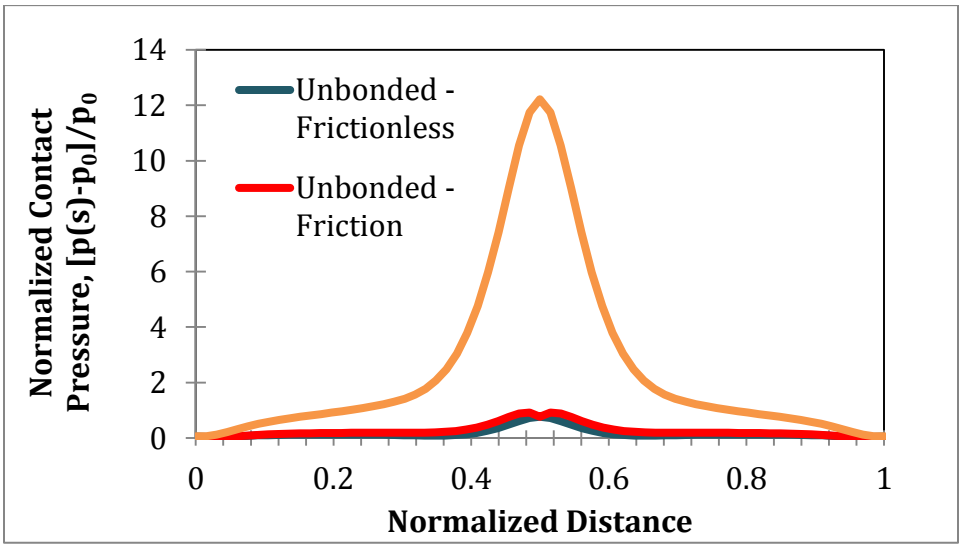

Figure 30: Resulting contact pressure profiles from simulation of three different interface properties with center displacement of 3 mm [226].

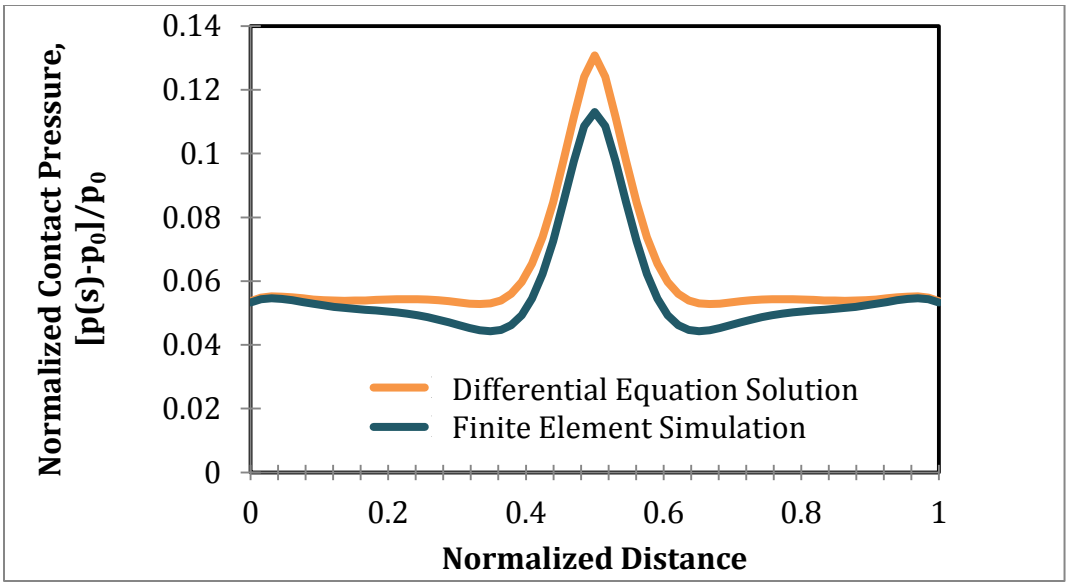

Figure 31: Comparison of contact pressure profile at cathode/electrolyte interface from numerical solution of the differential equations in Section 2 and the finite element simulation [226].

3.2 Comparison of bending methods

The effect of the method of bending on the contact pressure was compared for a set interface condition. Four states of bending were simulated in the finite element model, and include the following:

- A transverse shear force applied at the beam midpoint,
- Coupled bending moments applied at the end of the beam,
- Shear load per unit length of the beam, and
- End buckling.

Figure 32 illustrates the methods of bending that were considered in the analysis [226].

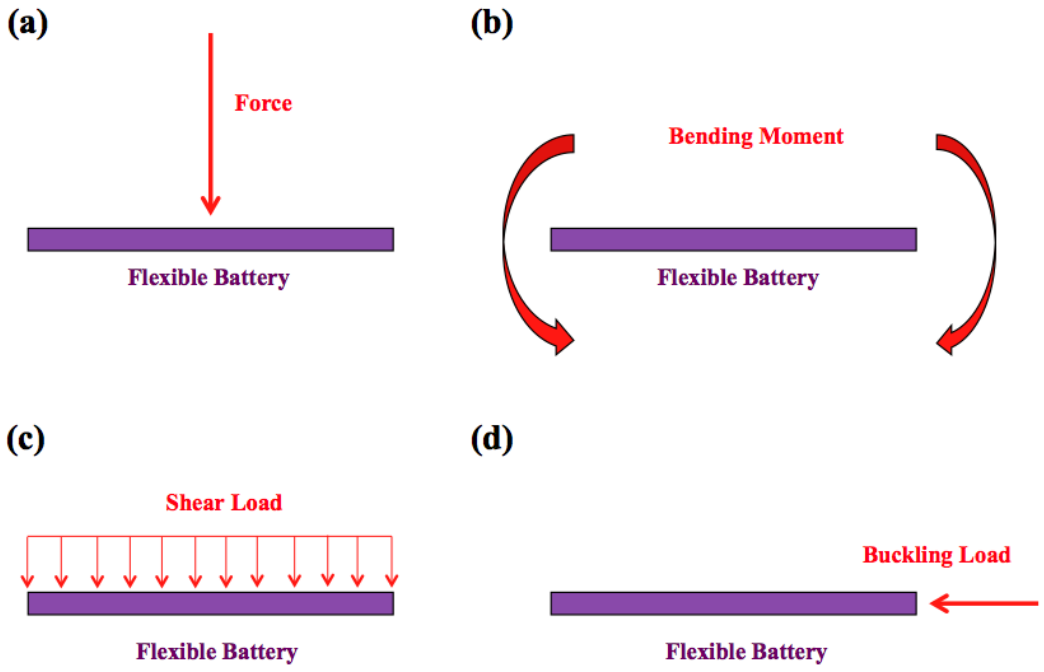

Figure 32: Four states of bending – a) a force applied at the beam midpoint; b) bending moments applied at the end of the beam; c) shear load per unit length; d) end buckling [226].

In these cases, all beams were treated as simply supported, where one end was constrained in the horizontal and vertical direction, while the other end was constrained in the vertical only. This allowed for any horizontal end displacement, including shape change in the buckling case. The contact pressure profiles were obtained at the cathode/electrolyte interface for each bending case assuming an unbounded, frictionless interface. The profile between the electrolyte and the anode was checked, and found to be very similar. Figure 33 shows a plot of the resulting contact pressure profiles for each bending method along the normalized length, away from the influence of end effects, for a bending radius of approximately 17 mm measured at the center of the battery. An important observation is that each contact

pressure function resembles the nature of the input function, which is well illustrated in the Midpoint Shear Force case resembling that of an impulse function.

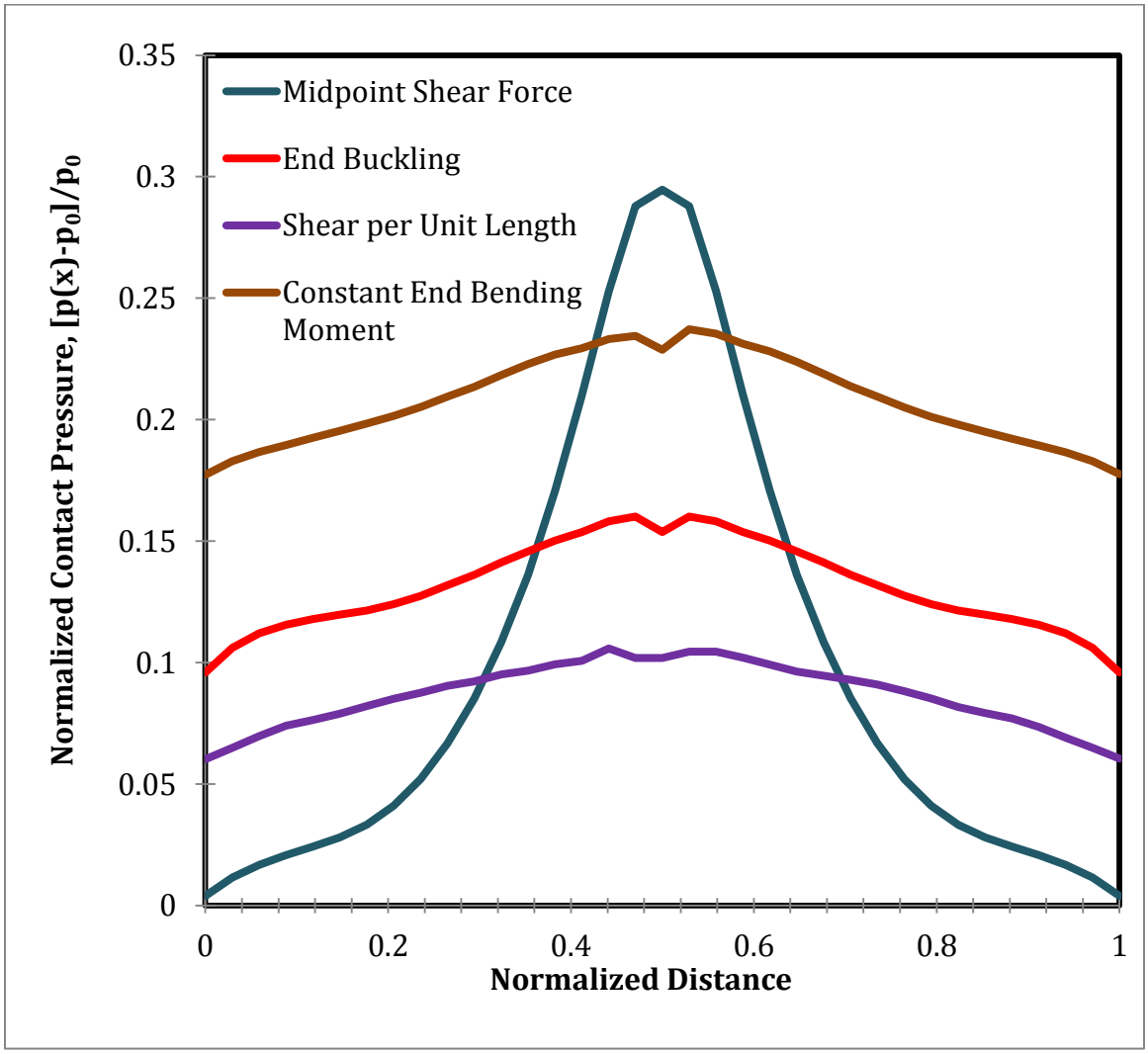

Figure 33: Plot of contact pressure at a contact interface along the length of the electrolyte (bending radius ρ≈17mm) [226].

The average of the contact pressure profile along the length of the electrolyte was then obtained, and the data was normalized and plotted as a function of the

center curvature as shown in Figure 34. The center curvature was calculated from the numerical model using Equation 24.

An interesting trend observed is that the contact pressure increases nonlinearly with the increasing curvature of the battery under bending, which is observed for each method of applied bending. One explanation for this is that the magnitude of bending load required to produce a particular center curvature is inversely proportional to bending radius. The variation in the trend of the curvature with average contact pressure for each method of bending is influenced by the resulting geometric profile of the battery, which varies along the length of the battery. The local contact pressure is a function of the local angle and second derivative of the curvature, $d\theta/ds$, which is generally greater along the length of the battery for the constant bending moment, constant shear, and end buckling methods as compared with the shear force applied to beam midpoint. This is supported both mathematically and visually as the deflection profile has a rounder shape in the other bending methods compared with the midpoint shear force method. The contact pressure increases nonlinearly with increasing curvature, and a similar trend was previously observed [11]. There are slight variations in the trend lines for each method of bending.

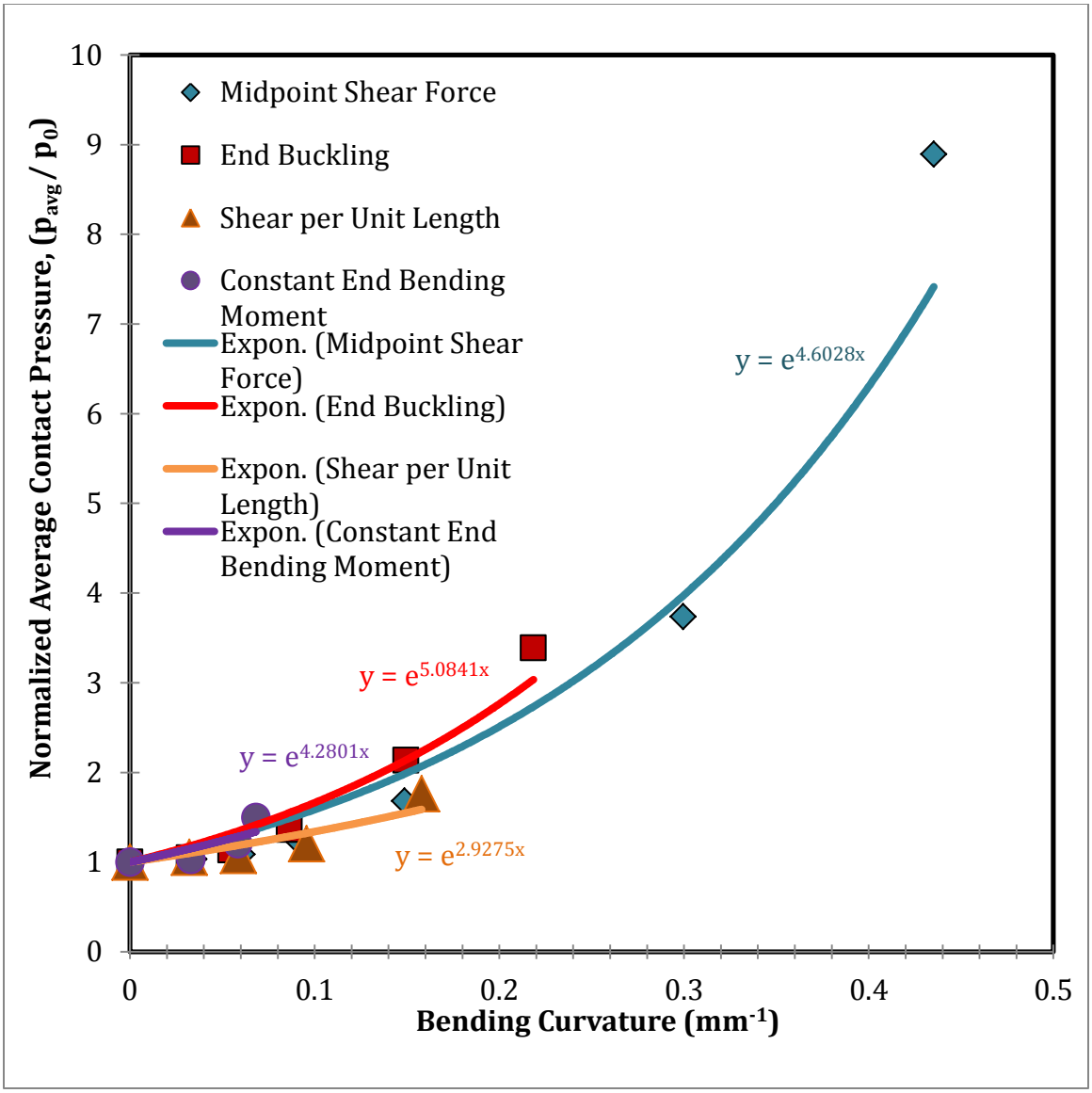

Figure 34: Plot of the average contact pressure change with increasing curvature - normalized by lamination pressure [226].

4. Experimental comparison

The results from the computational work were compared against experimentally obtained data resulting from measuring the impedance of the battery under applied bending. This was to explore the previous observations of the impact of bending on

the battery performance. Multiple flexible batteries, using our laboratory's design [11], were fabricated and used for the bending experiment.

Each battery was placed into an apparatus, and an end displacement was applied to each battery, as shown in Figure 35a-c [226]. Horizontal displacements ranging from approximately 10-20 mm were applied to the end of each battery, which resulted in different center bending curvatures. The radius of curvature at the center of the bent battery was measured using a circle fit method. The contact impedance was measured for each curvature using Nyquist plots and equivalent circuits, as shown in Figure 35d, and the contact conductance was determined as the reciprocal of the contact component of impedance ($1/R_c$). The experimentally applied method of bending is similar to the end buckling method that was numerically modeled, and therefore both results were compared.

The measured contact conductance for a given curvature was normalized by the contact conductance of the battery in the unloaded, flat condition and plotted as a function of curvature. Likewise the contact pressure determined from the numerical analysis was normalized against the initial lamination contact pressure and plotted as a function of curvature. The normalized experimental and numerical data was combined into a single plot as shown in Figure 35d. In comparing the data, it is observed that both lines follow a similar exponential trend, and a direct proportionality can be demonstrated between contact pressure and contact conductance. This shows that the battery performance is directly influenced by the layer contact pressure that results from the applied bending. The slight difference

between the numerical and experimental values is attributed to the interfacial contact properties of the experimental battery, and the condition modeled numerically, which can be difficult to measure [226].

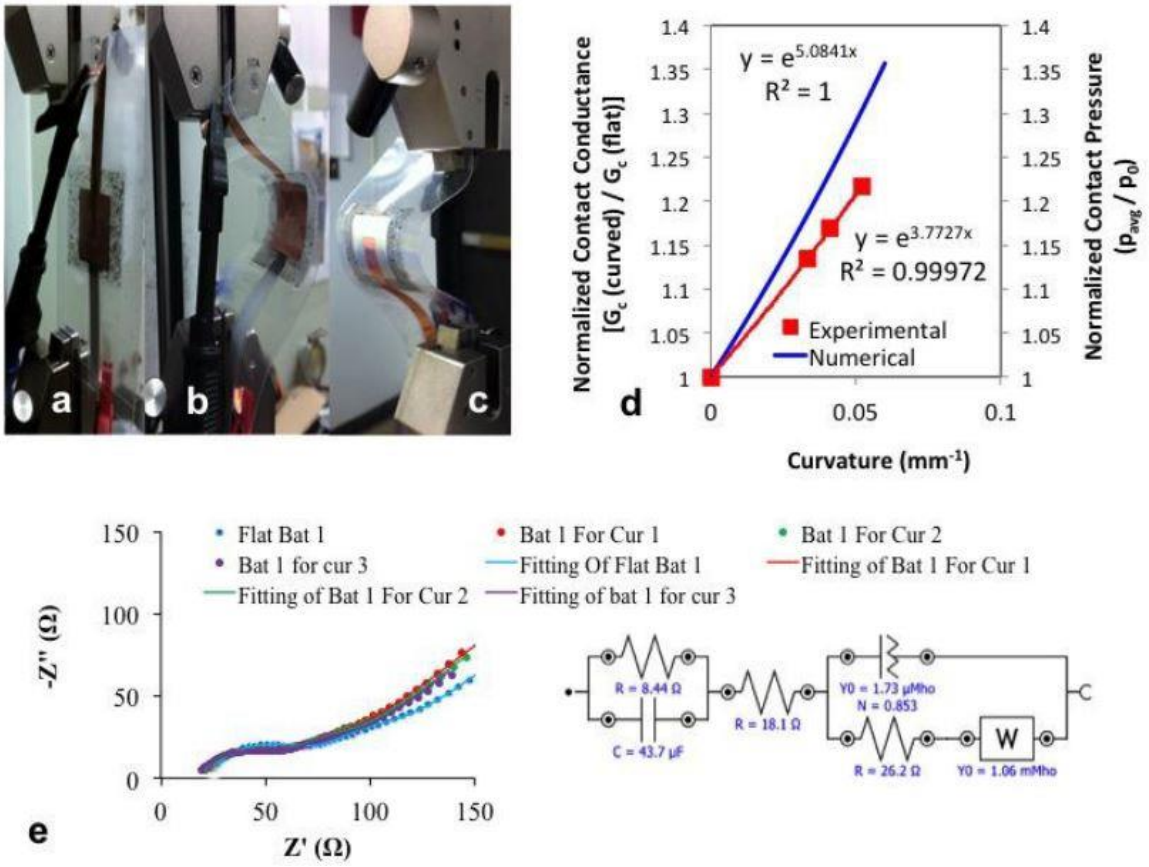

Figure 35: Experimental procedure showing a-c) test apparatus demonstrating battery displacement; d) circle fit method; e) comparison between the experimental and numerical contact pressure [226].

A useful empirical relationship between the contact conductance, G_c, and the bending curvature, κ, was obtained from the data presented in Figure 35, and is shown in the following:

$$G_c = e^{m\kappa}. \qquad (41)$$

Equation 41 suggests that the relationship of contact conductance to bending curvature is exponential, where the exponential constant, m, is approximately $3.7 \leq m \leq 5.1$. This is valid for the end buckling bending type in the range of bending curvatures from $0 \leq \kappa \leq 0.05$, and is in the range of testing experimentally, which may encompass a broad range of practical bending curvatures [226].

5. Conclusions

The analytical framework shows a direct relationship between bending, interface properties between the battery layers, and contact pressure in the battery structure, which was verified using finite element modeling. The contact conductance is shown to follow the same trend as the contact pressure. A nonlinear increase in contact pressure that follows an exponential trend was observed, and the method of bending and interface properties were found to substantially impact the contact pressure profiles. The contact conductance is shown to correlate to the contact pressure, since experimentally the change in contact conductance with bending was shown to follow the same trend as the contact pressure obtained numerically. This demonstrates how the applied bending and resulting contact pressure between the electrode/electrolyte layers affects the battery performance.

Chapter IV Modeling the Mechanical Response of a Spiral Stretchable Battery

1. Spiral stretchable battery design

In previous chapters the focus was on flexible batteries, which are optimized for bending and twisting loads. Another battery concept that was developed in our laboratory was a stretchable SPE LIB based on a spiral pattern geometry. The spiral geometry concept allows the battery to be capable of large out-of-plane tensile deformation as opposed to bending, while maintaining operation. This battery was fabricated in our laboratory and subject to load testing to evaluate the performance under applied extension loading. The fabrication of the spiral stretchable battery utilized stacking similar to that of the flexible SPE LIB, where the battery components were stacked into layers. The fabrication methods and procedures were similar to those for the flexible battery described in Chapter II. The spiral pattern LIB was capable of achieving 9000 stretching cycles and an energy density of 4.862 mWh/cm^3 at 600% out-of-plane deformation [227]. Figure 36 shows the configuration of the spiral battery, provided courtesy of [227], in addition to showing how the battery functions under applied out-of-plane loading.

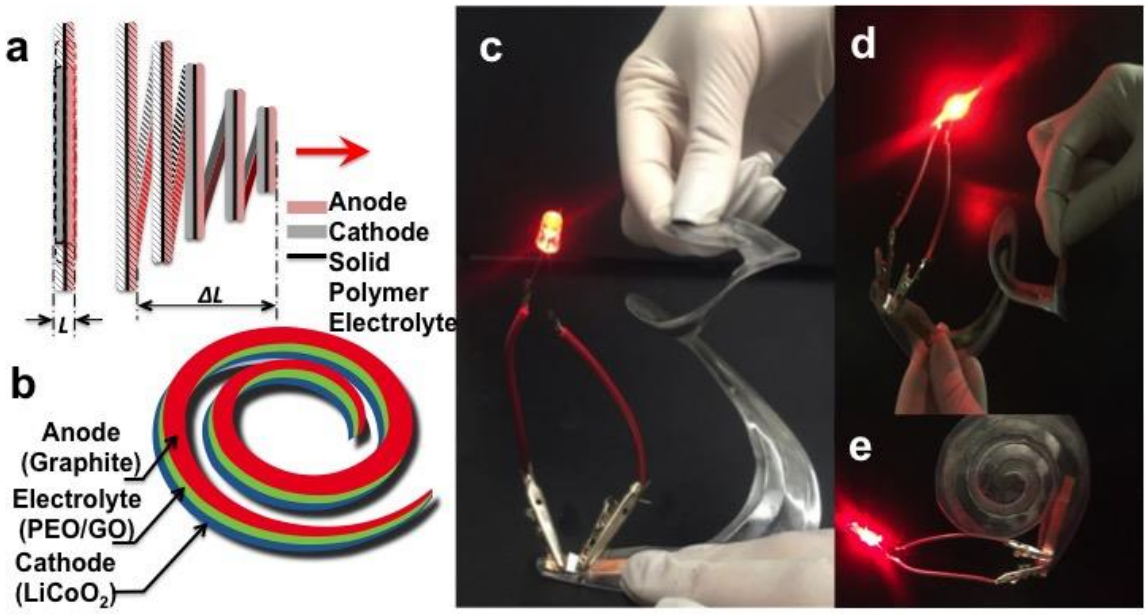

Figure 36: Illustration showing (a)-(b) the schematics of the spiral Li-ion battery, (c)-(d) photo image of the fabricated spiral battery in stretched positions lighting a red LED, (e) spiral battery in flat position (provided courtesy of [227]).

As with the flexible battery, the mechanical response of the spiral battery under states of loading was of interest in the evaluation of the battery performance due to the fact that a key feature of the battery is that it is designed to be subjected to mechanical loading, which will result in a state of stress in the battery. Additionally, the loading state can influence battery performance, e.g., delamination of the layers. In addition to the experimental evaluation of the battery, a simulation of the battery subjected to the loading as described in the lab was completed. This was to conduct a more detailed evaluation of the material response of the battery by evaluating parameters such as stress, strain, and displacement. The following sections provide the details of the simulation methods, and a discussion of the results and the implications on battery performance.

2. Numerical analysis

The numerical analysis of the spiral stretchable battery was completed using the finite element method, in order to model the response of the battery. Dassault Systemmes Abaqus Version 6.13-5 commercially available finite element software was used to evaluate the battery under loading. The following sections outline the details of the numerical analysis completed, including a description the geometry, mesh, materials, contacts, loads, and boundary conditions.

2.1 Geometry and mesh

The layers of the battery were stacked initially in contact and modeled in a 3D spiral pattern with uniform prismatic cross-sections. The thicknesses of each battery layer and the materials were modeled based on the experiment, and a linear elastic material model was created. The geometry was meshed using a part instance dependent mesh scheme. Each layer was meshed with 3D continuum stress elements. The 3D continuum stress elements are solid elements that calculate field variables in all coordinate directions to account for translations and rotations. In other words, the full stress and deformation tensors can be calculated. All layers were modeled with C3D20 elements. These are higher order elements that are capable of modeling the large strains and kinematics associated with the types of loading for this stretchable battery. Mesh refinement was completed to ensure that proper mesh convergence was achieved. This provided the most accurate resolution of the strain field.

2.2 Material models

Only the PEO with 1 wt% GO electrolyte was modeled in the finite element analysis. The following assumptions were made with regard to the simulation:

- The mechanical response of the battery could be modeled using linear elastic material constitutive models, e.g., no plasticity or yielding is assumed to occur during the loading considered.
- Large deformation modeling was assumed, with deformation tensors calculated with respect to current configuration, and effects due to nonlinear geometry were considered.

Material properties inputs for the analysis included the bulk modulus of elasticity and Poisson's ratio for each material. The materials for this battery were the same as that for the flexible battery, and therefore the same material properties were used in the numerical analysis of the spiral stretchable battery as the flexible battery materials, as shown in Table 2.

2.3 Contact properties and layer interactions

Since each layer was modeled as a separate, individual part mating together in a stack, contact properties were defined in the model. Due to the battery fabrication, each layer was assumed in hard contact with all layers assumed to be held together with adhesive. In order to simulate the adhesive condition, multipoint constraints, or "tie" constraints, were defined at each layer interface.

2.4 Loads and boundary conditions

The simulation separates the various loading out by modeling each load individually in different steps. In a linear elastic stress analysis, by modeling the loads sequentially in steps, the full stress state can be accounted for in the simulation via superposition. The simulation starts by modeling the lamination/ encapsulation process, which is followed by the applied out-of-plane loading.

A fixed displacement boundary condition was applied to the outer end of the spiral to prevent it from movement during extension, and to provide a reaction point during the application of the load. The extension load was in the form of a displacement at the innermost part of the spiral of 200 mm in the axial (out-of-plane) direction. After encapsulation, the extension was applied to the battery. Nodal forces were selected as a field output in order to obtain the magnitude and the direction of net resultant nodal forces resulting from element stress during load application. At cross-sections of interest along the spiral length the net forces and moments with respect to a local coordinate system and the cross-sectional centroid were determined via the program by accounting for the resulting directional nodal force variation through the cross-section due to element stress. This made it possible to determine the effects of torsion, the stress distribution, and the change in local moment throughout the spiral with respect to the local moment arm, which is at a particular radial location along the spiral. This process is explained and illustrated in greater detail in the following section.

3. Results and discussion

The finite element model that was created for simulation, and the associated results, are shown in Figure 37 [227], which shows the axial displacement gradient, state of stress during the extension process, and the force variation across the spiral cross-section corresponding to the torsional direction, indicating a resulting torsional moment. The results of the analysis shows the stress distribution increases throughout the spiral, and the local torsional and bending moments vary along the spiral, which is expected as the moment arm increases radiating outward on the spiral. The axial (out-of-plane) displacement and extension also follows this same pattern since this loading is directly related to the distribution of material during the loading.

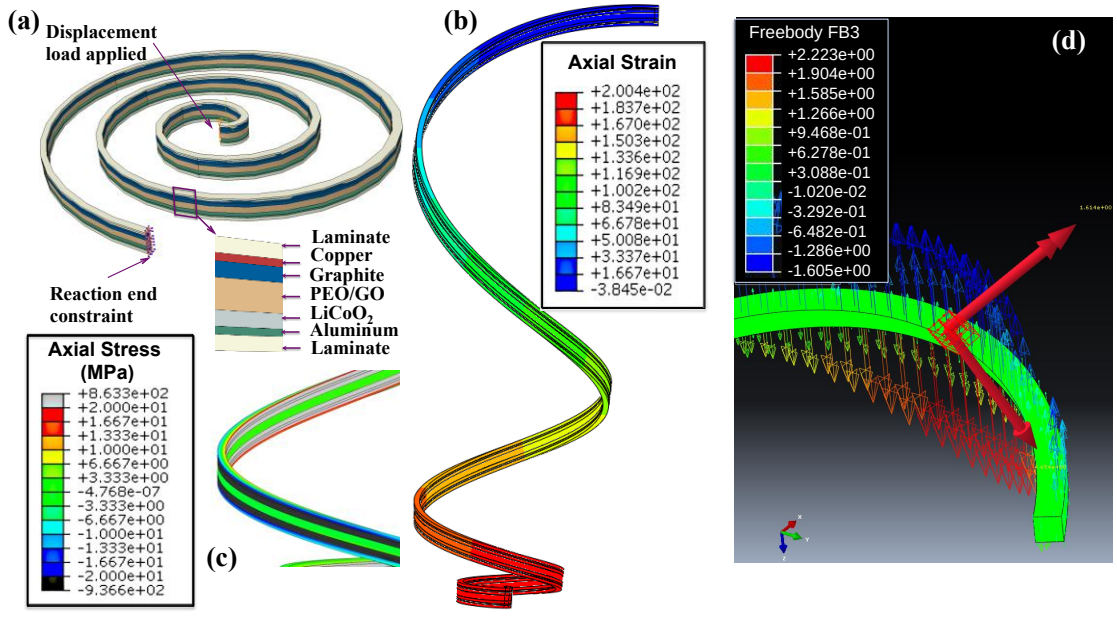

Figure 37: (a) Finite element model, (b) strain variation in stretched spiral battery, (c) stress variation in spiral battery, (d) cross-sectional force variation indicating the state of torsion in the spiral battery [227].

The extension results in a normal bending moment in addition to torsion, both of which increase with increasing spiral radius, which is expected since the moment arm from the center increases. This is further demonstrated in the plot of the stress variation in the battery, which shows a variation going from tensile to compressive through the cross-section. The extension of the battery results in the displacement gradient shown in Figure 37b, with increased displacement/extension as the spiral radius increases from the center. The torque, moment and displacements increase along the axial direction of the battery and with increasing spiral radius, and the stress distribution varies through the cross-section and along the battery length at the equilibrium state.

4. Analytical development of mechanical response in spiral battery

In order to explain the results obtained in the finite element analysis, an analytical model is obtained to generalize the mechanical response in the spiral pattern battery. A spiral geometry is assumed for the flexible battery resembling the depiction shown in Figure 38.

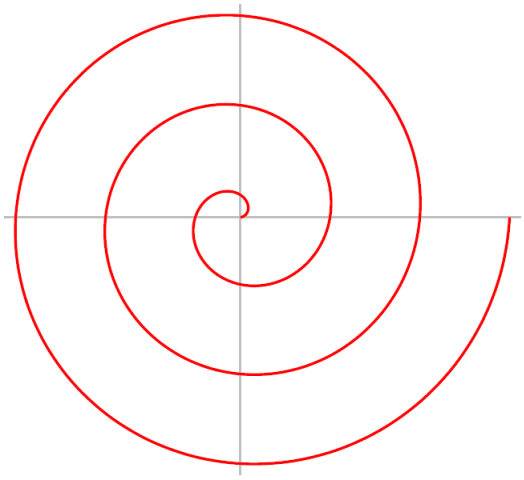

Figure 38: General depiction of a spiral geometry.

The instantaneous radius of the spiral varies with angle and increases moving away from the center. In polar coordinates the spiral can be represented by radius, r, as a function of angle, θ, as shown in

$$\boldsymbol{r} = \boldsymbol{f}(\boldsymbol{r}(\boldsymbol{\theta})). \qquad (42)$$

It is important to understand that the coil radius is not constant. It is useful to develop a relationship between the parameters of applied input extension force, instantaneous spiral radius, stress, and the displacement in the axial direction. We start by evaluating the stress in a cross-section of interest at instantaneous radius, r. For this evaluation, the termination point at the outer part of the battery is assumed fixed while an extension force is applied at the center starting point of the battery in the out-of-plane or axial direction, illustrated in Figure 39. In consideration of the cross-section stresses, dominant stress effects in the cross-section are due to shear and torsional stresses, as shown in Figure 40.

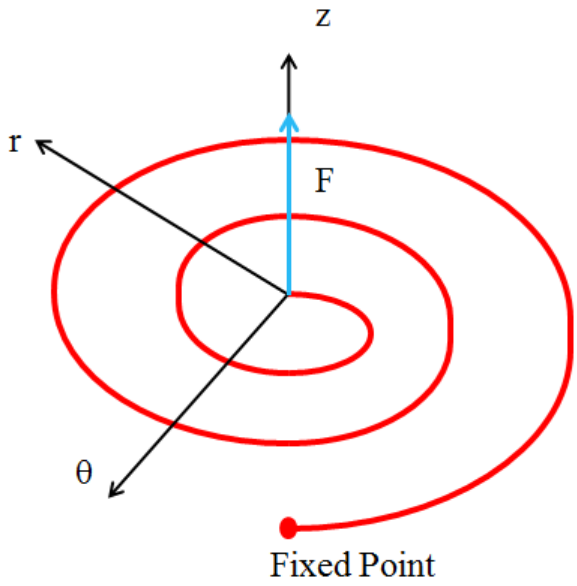

Figure 39: Load diagram depicting applied extension force normal to spiral plane and end constraint.

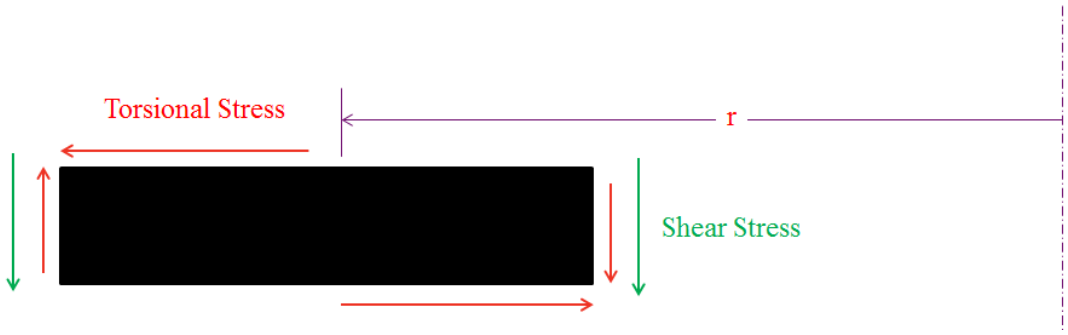

Figure 40: Representation of stresses acting on battery cross-section and radius, r.

Since the applied force is in the out-of-plane direction relative to the spiral plane, and under extension the coils would orient themselves parallel to one another, shear plane stresses are expected to dominate [228]. For the applied extension force, the direction of shear stress and torsional stress is such that the stress at the innermost fiber of the coil geometry, at the ID, is the most highly stressed. In an

elastic material model the directional shear stresses act in the same plane and would interact via superposition, and the max shear stress is represented by

$$\boldsymbol{\tau_{max}} = \frac{\boldsymbol{Tr}}{\boldsymbol{J}} + \frac{\boldsymbol{F}}{\boldsymbol{A}}, \tag{43}$$

where J is the polar moment of inertia, r is the instantaneous radius of the spiral, F is the applied extension force, T is the cross-sectional torsion, and A is the cross-sectional area of the battery. It is shown in the numerical model that the torque increases as the instantaneous radius increases. This can be shown by

$$\boldsymbol{T = Fr}, \tag{44}$$

which shows that if the applied input force is constant, the torque varies proportionally to the instantaneous radius, r. The partial of stress with respect to the radius is given as

$$\frac{\boldsymbol{\partial \tau_{max}}}{\boldsymbol{\partial r}} \frac{\boldsymbol{\partial r}}{\boldsymbol{\partial \theta}} = \frac{\boldsymbol{2Fr}}{\boldsymbol{J}} \frac{\boldsymbol{\partial r}}{\boldsymbol{\partial \theta}}. \tag{45}$$

For an Archimedean spiral, where r=θ, the partial derivative of stress with respect to instantaneous diameter remains constant. This would indicate a linear stress increase throughout the length of the spiral. It is observed in the numerical model that the axial displacement increases nonlinearly as the instantaneous radius increases. In order to understand this increase, application of Castagliano's Theorem is necessary and is given in the following:

$$\boldsymbol{dU} = \frac{\boldsymbol{1}}{\boldsymbol{2}} \boldsymbol{\tau d\varphi}, \tag{46}$$

$$\boldsymbol{\varphi} = \frac{\boldsymbol{FrS}}{\boldsymbol{G}}, \tag{47}$$

$$\boldsymbol{S} = \boldsymbol{f}(\boldsymbol{r}), \tag{48}$$

$$\boldsymbol{U} = \frac{(\boldsymbol{Fr})^2\boldsymbol{rS}}{\boldsymbol{6JG}} + \frac{\boldsymbol{F^2rS}}{\boldsymbol{2AG}}, \tag{49}$$

$$\boldsymbol{\delta} = \frac{\boldsymbol{\partial U}}{\boldsymbol{\partial F}} = \left[\frac{\boldsymbol{Fr^2}}{\boldsymbol{3J}} + \frac{\boldsymbol{F}}{\boldsymbol{A}}\right]\left(\frac{\boldsymbol{rS}}{\boldsymbol{G}}\right), \tag{50}$$

$$\frac{\boldsymbol{\partial\delta}}{\boldsymbol{\partial S}}\frac{\boldsymbol{\partial S}}{\boldsymbol{\partial r}}\frac{\boldsymbol{\partial r}}{\boldsymbol{\partial\theta}} = \frac{\boldsymbol{\partial^2 U}}{\boldsymbol{\partial F\partial S}}\frac{\boldsymbol{\partial S}}{\boldsymbol{\partial r}}\frac{\boldsymbol{\partial r}}{\boldsymbol{\partial\theta}} = \boldsymbol{F}\frac{\boldsymbol{\partial r}}{\boldsymbol{\partial\theta}}\left(\boldsymbol{r^3}\frac{\boldsymbol{\partial S}}{\boldsymbol{\partial r}} + \boldsymbol{2r^2S}\right)\left(\frac{\boldsymbol{1}}{\boldsymbol{3GJ}} + \frac{\boldsymbol{1}}{\boldsymbol{2AGr^2}}\right), \text{ and} \tag{51}$$

$$\boldsymbol{k} = \frac{\boldsymbol{F}}{\boldsymbol{\delta}} = \left[\frac{\boldsymbol{3JA}}{\boldsymbol{r^2A+3J}}\right]\left(\frac{\boldsymbol{rS}}{\boldsymbol{G}}\right). \tag{52}$$

Evaluation of the strain energy due to the applied loading is necessary, which is represented generally by Equation 46. The angle of twist, φ, in terms of applied force, F, and instantaneous radius, r, is related to Hooke's law in the elastic stress limit. Combining Equations, 43, 46, and 47, and integrating yields an expression for internal energy. The value of S is the total length of the spring. Per Castagliano's Theorem, the axial displacement, collinear to the applied extension force in the out-of-plane direction, is related to the partial derivative of the strain energy with respect to the applied force, F [228]. Out of this, the displacement, δ, is shown to be related to a polynomial of the instantaneous radius, r. The rate of change of the axial displacement, the second partial derivative of the strain energy with respect to radius, is related to a polynomial of the instantaneous radius, r. Equation 52 illustrates the rate at which the axial displacement changes with instantaneous radius, r. This is as expected since as the instantaneous radius increases, the local axial displacement and elastic spring constant associated with the spring changes

with instantaneous radius. This is reflected in the numerical results using the finite element method.

5. Conclusions

The results of the analysis suggest that the force reactions and out-of-plane displacement of the spiral are strongly tied to the instantaneous radius, which is what was observed experimentally. However, the stress in the battery along the length of extension is observed to have little variation. As a result, it is expected that the contact pressure between the various layers within the battery will vary less as a result of change in instantaneous radius, but is expected to vary from the ID to the OD of the battery due to torsion. This is expected to be most influential in limiting battery performance, since the torsional stress at the ID may lead to material failure, or delamination of the layers is possible in this region due to excessive strains.

Chapter V The Influence of Deformation on Ionic Conductivity in Solid Polymer Electrolytes

1. Coupling of mechanical and electrochemical properties

Previously in this work, the assessment of battery performance was based primarily on modeling the mechanical response of the flexible battery under an applied load. The resulting stress and deflection was evaluated in depth, and the impact on battery performance was studied through a combination of modeling, computational simulation, and experimental observation. In this section, a discussion of the battery materials undergoing deformation, specifically the polymer electrolyte, and the impact on the ionic conduction, will commence. The goal is to obtain an understanding of the coupling between electrochemical and mechanical response of flexible and stretchable batteries. In this chapter, the focus will be initially on understanding polymer deformation mechanisms that occur in a sample of PEO, which has been selected as a candidate for the electrolyte material in a stretchable battery concept developed in our lab.

2. Mechanical properties and polymer deformation

A discussion of the characteristics of the PEO electrolyte itself, which is a semi-crystalline polymer, is warranted. Semi-crystalline polymers have both crystalline and amorphous phase grains within their microstructures. In the structured crystalline phases, polymer chains are ordered into regions called crystallites. The

amorphous phase is generally present on the edges of the crystallites tying these grains together. The microstructure of the semi-crystalline PEO sample was viewed using Polarization Light Microscopy (PLM). In addition to viewing the microstructure in an unstretched state, PLM was used to observe the effect of stretching on the molecular structure of the polymer electrolyte. Figure 41 shows the evolution during stretching, provided courtesy of [12]. The PLM images in Figure 41 are of the PEO polymer in unstretched (left) and stretched (right) states at various levels of magnification. There is a color contrast in the images, where dark regions suggest amorphous phases, and the light regions highlight the crystalline grains. The dark areas, visible at 10x-50x magnification, around the crystallites are the amorphous entalged polymer chains tying the crystallite grains together. As can be seen in the images, the dark regions appear to become larger going from unstretched to stretched states, which confirms a growth or extension of the amorphous regions as the chains disentangle [12].

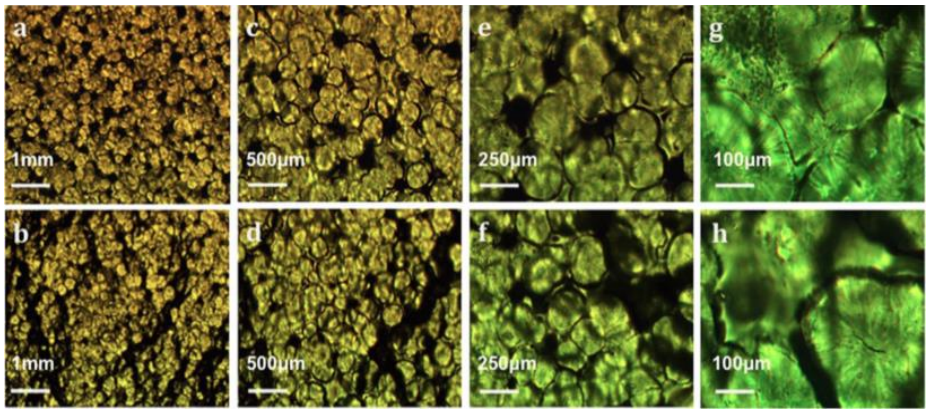

Figure 41: Polarization Light Microscopy (PLM) images of unstretched (top) and stretched (bottom) PEO where (a-b) indicate 50x magnification, (c-d) indicate 100x, (e-f) indicate 200x, and (g-h) indicate 500x magnifications [12].

The mechanical properties of 600,000 Mw PEO/LiClO4 were obtained via mechanical testing which occurred in our lab. This was to verify that the PEO electrolyte strain response under loading was similar to that of typical semi-crystalline polymers. Initially, tensile testing was carried out on PEO electrolyte samples to obtain stress vs. strain curves, shown in Figure 42a-b, provided courtesy of [12]. The strain rate of each sample was varied to assess the influence of the viscoelastic response in the PEO material. Strain rates were increased by an order of magnitude in each test, starting with 0.5 mm/min, increasing to 3.5 mm/min, and then 35 mm/min in the tensile test machine. Table 3 provides the measured property values of yield strength and ultimate tensile strength. The Poisson's ratio and elastic modulus are also provided, with the elastic modulus being calculated by evaluating the slope of the elastic region of the stress vs. strain curve. As shown, the modulus of elasticity, or stiffness response of the material, increases with increasing strain rate. This is expected since at high strain rates, the time scale is such that the viscous forces do not have time to respond, and their effects are small.

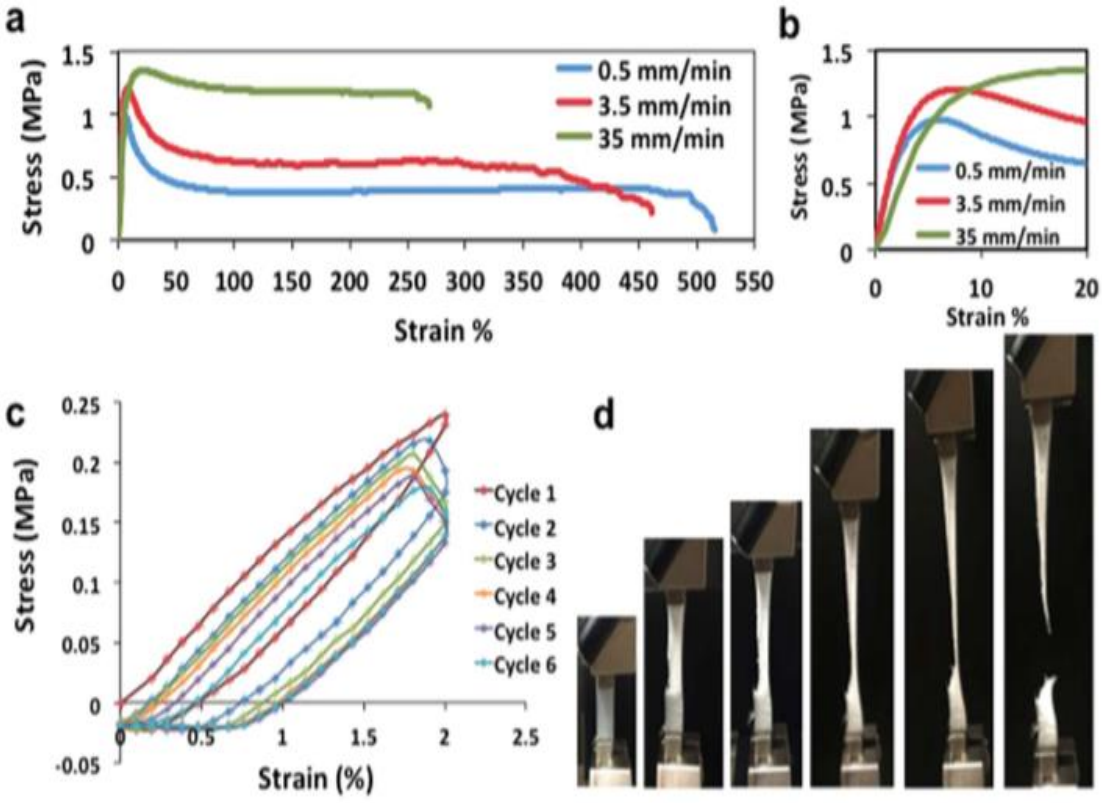

Figure 42: Tensile stress-strain behavior of solid PEO electrolyte (a) at three strain rates, (b) magnified curve below 20% strain, (c) stress-strain hysteresis, and (d) images of PEO under tensile deformation [12].

Table 3: Mechanical properties of thin- lm 600,000 Mw PEO/LiClO4.

Material (Temperature, Strain Rate)		Yield Strength (MPa)	Tensile Strength (MPa)	% Elongation	Poisson's Ratio
PEO (18 °C, 3.5 mm/min)		0.81	1.26	141	0.231
PEO (25 °C)	0.5 mm/min	0.64	0.99	509	0.241
	3.5 mm/min	0.66	1.02	457	0.236
	35 mm/min	0.91	1.54	278	0.238

As can be observed in the stress vs. strain curves, a few different behaviors are seen in the mechanical response of the sample. Initially the deformation is linearly elastic. This is followed by a peak stress that is reached in the stress vs. strain curve,

which is accompanied by a drop in stress. After the drop in stress, the stress response is monotonically increasing, which corresponds to a “drawing” process. Finally, the sample fractures and the tensile strength is observed [229].

The deformation within a semi-crystalline polymer has been studied previously [230-243]. The evolution of the microstructural changes during deformation is illustrated in Figure 43, provided courtesy of [12]. The changes in the microstructure during deformation can be explained by a number of sequential processes. For a small applied stress or strain the polymer chains begin to elongate, but the mechanical response is elastic in nature. During this process the amorphous regions grow and transmit the imparted loading, which is carried by the crystalline grains. The crystallite blocks slide and begin to orient into the direction of applied load [230]. The mechanical response of the crystalline region is elastic while the response of the amorphous region possess both elastic and viscoelastic behavior. Beyond a critical stress, or yield stress, the onset of yielding occurs, where favorably oriented crystalline grains subject to excessive shear begin to see an increase in dislocation motion. During this stage the polymer chain sliding results in the crystallites being transformed into fibrils [230-231]. With the increase in dislocations, void nucleation and growth, and necking occur. As this process progresses, the force carried predominantly by the crystallites shifts to the amorphous regions until the chains are fully disentangled. This is the so-called “drawing” region of the stress vs. strain curve. Once the chains are fully disentangled, bonds begin to break, and fracture of the sample is complete.

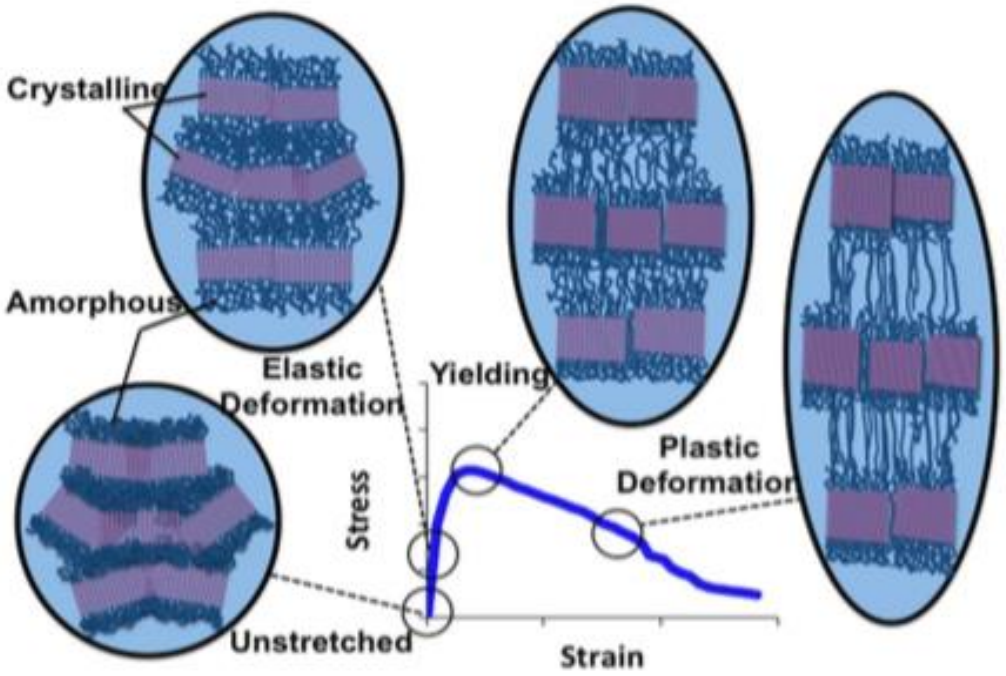

Figure 43: Diagram illustrating the microstructural evolution during deformation, provided courtesy of [12].

The strength of the polymer depends largely upon the degree of crystallinity, temperature, density, etc. among other factors. In PEO, the amorphous regions of the polymer are the most mechanically compliant part of the microstructure during applied tensile loading. The nature of inelastic deformation, or plasticity, in semi-crystalline polymers can be preceded by cavitation in the amorphous regions; however, the driving mechanisms depend on the strength of the crystallite grains and their susceptibility to shear deformation, void nucleation and growth [12, 240-243].

Another important feature in understanding the polymer response is the time-dependency of the viscoelasticity. It is important to note that as the strain rate

increases, the stress vs. strain curve appears to shift upward. This would seem to impact the strength of the sample as well, in addition to the character of the crystallite grains present in the sample. This is because for higher strain rates, the viscous forces within the sample do not have adequate time to respond, and therefore the elastic-plastic rather than viscoelastic response dominates [231, 233-235].

Further studying the viscoelastic characteristics of the electrolyte sample, the cyclic stress/strain response is also tested. For a constant strain rate and fixed strain, the polymer sample is loaded and unloaded multiple times, with each load/unload event considered as a single cycle. This cyclic behavior is plotted in Figure 42. It can be shown upon close evaluation of the tensile behavior of the specimen that the unload path differs from the load path, which forms a hysteresis loop. Upon tensile reloading of the specimen, a noticeable drop in stress is observed at fixed strain. This is a feature of the viscoelasticity of the semi-crystalline polymer and indicative of a type of mechanical damage [244]. Further cyclic loading would theoretically show that the change in stress with cyclic loading would be monotonic and approach an asymptotic value. This indicates that the viscoelasticity results in a stress relaxation phenomenon.

It is predicted that the hysteresis behavior observed in the polymer electrolyte would result in heat generation [233-235]. This heat generation could be determined by accounting for both the steady state true stress/strain and the time dependent viscous dissipation, given by the following:

$$\boldsymbol{Q} = \oint_{\mathbf{1}}^{\mathbf{2}} \left[\boldsymbol{\sigma}(\boldsymbol{\varepsilon}, \boldsymbol{t} \to \infty)\boldsymbol{d\varepsilon} + \boldsymbol{\sigma}(\boldsymbol{\varepsilon}, \boldsymbol{t})\frac{\boldsymbol{d\varepsilon}}{\boldsymbol{dt}}\boldsymbol{dt}\right] \text{ and} \quad (53)$$

$$\varepsilon=\varepsilon_B+\varepsilon_C. \quad (54)$$

In this model the dissipation can be calculated per cycle via a closed contour integral following the cycle path, where Q is the heat dissipation, σ is the stress, ε is the strain, and t is time. Furthermore, it is suggested that on unloading the strain, ε, can be represented by the recoverable cyclic component, ε_C, and a non-recoverable component, ε_B [231].

3. Impact of deformation on ionic conductivity

With an understanding of the how the deformation mechanisms relate to the mechanical response of the polymer electrolyte, deeper study can commence to understand how the deformation processes influence the electrochemistry of the electrolyte. In this case, of particular interest is the property of ionic conductivity, which is related to the mobility and diffusivity of the lithium ions within the polymer sample.

We begin our discussion by first reiterating the various phases of deformation within the polymer. When the behavior of the specimen is predominantly elastic in nature, internal forces and viscous forces are transmitted within the amorphous and crystalline phase structures. The forces carried by the structures manifest as stress. The elastic strain range in the semi-crystalline PEO is small and less than 5% strain at room temperature. Due to the high degree of crystallinity present in the PEO

samples at room temperature, the ion conduction is generally low under these conditions since the crystalline grains slow diffusion of lithium ions due to the arrangement of the polymer chains. The ions can move more freely in the amorphous regions of the sample [245-246]. When a large enough stress is applied to the polymer sample, enough to cause the onset of yielding, void nucleation and growth occurs at yielding, which can be confirmed visually by observed voids within the sample [12]. The degree of void nucleation and growth is dependent on whether or not particles are in contact with the void surfaces, which constrains the void [232]. As voids grow in the crystalline phases during deformation, ion mobility is enhanced and ionic conductivity is observed to increase, as predicted by [12].

The effects of ionic conductivity in stretched PEO samples in the direction parallel to polymer extension have been studied [245-254]. The increasing trends observed in ion conductivity are a result of the changes that occur in the polymer electrolyte microstructure due to deformation. Improved ion conduction is observed to result from the tensile deformation of the PEO. Based on the measurement and experimental work completed by others in our research group [12], we can hypothesize that the stretching and aligning of the amorphous polymer chains decreases the degree of tortuosity in the polymer, which results in less obstruction in the microstructure and enhanced ion transport throughout the polymer electrolyte. Additionally, as previously stated the nature of the amorphous polymer chains plays an important role in ion conductivity. Specifically, conformation of the chains in the amorphous region, and the strength of polymer chains, are dependent on several components [229, 231-237, 239-244]. Factors such

as tortuosity, and chain disentanglement upon deformation, also influence ion motion [12].

4. Conclusions

The physical mechanisms that influence ionic conductivity and ion motion within the electrolyte sample have been discussed and explored in this chapter. These are important in understanding how battery performance can be influenced by applied loading and deformation of the electrolyte, since ion diffusion through the electrolyte directly impacts battery performance. While these microstructural mechanisms relate to the influence of deformation on ion mobility, it is desired to establish a direct relationship between the applied load, and the resulting strain field, ion diffusion, and ionic conductivity, which is also related to other physical mechanisms and forms of mass diffusion. In the following chapter, models will be developed to directly relate electrochemistry with mechanical response of the battery. These will be coupled multiphysics equations in terms of material parameters that are related to the mechanisms described in this chapter.

Chapter VI Analytical Models Coupling Ionic Conduction to Deformation to Predict Battery Performance

1. Coupled diffusion-stress ion conduction models

In Chapter V the deformation mechanisms and properties of the PEO electrolyte were discussed as they relate to ion conductivity. During the operation of a lithium ion battery, Li ions diffuse through the electrolyte moving between the electrodes during the intercalation process. This process is driven by both a concentration gradient and a difference in chemical potential, where on discharge Li ions are driven by available free energy, which facilitates the formation chemical reaction at the electrodes. During charge, energy is supplied in order to drive the chemical reaction in reverse. The ability of the ions to diffuse through the electrolyte directly impacts battery performance, since greater mobility of the ions to diffuse through the electrolyte matrix improves battery performance. Understanding the mechanisms and the kinetics of the diffusion process of the Li ions in the electrolyte matrix, particularly under deformation, is therefore important in order to better understand the direct impact on battery performance.

Since flexible and stretchable batteries are intended to function under an applied stress or strain field, it is important to understand how the intercalation process may be influenced by applied loading on the battery. Therefore, in this chapter, an analytical model is developed in order to understand the relationship between an

applied strain field on a body, in this case the electrolyte, and the diffusion within the body. Other relevant studies have been conducted to couple diffusion and stress in multiphysics equations [255-257]. In a study by Sastry and associates, an analogy to a heat transfer model is made to evaluate diffusion-induced stress in lithium ion batteries [255]. Work by Ferreira and colleagues takes a new look at diffusion induced stress, termed non-Fickian diffusion, to describe absorption phenomena in polymers, which results in considering nonlinear diffusion equations [257].

In order to start the model derivation, the mass flux of the Li ions is derived from the system mass balance. Assuming a steady state relationship, the terms within the flux equation are modeled by creating a relationship between the concentration gradient, which is typical Fickian diffusion, the stress gradient, which is associated with non-Fickian diffusion, and the overall driver of chemical species flux, which is the chemical potential gradient. Using this balance, and applying thermodynamic laws to develop a continuum equation to model the relationship between mass kinetics and mechanical deformation, the equation can be simplified and put into terms of concentration, applied strain or displacement field, and experimentally derived material parameters.

This initial framework considers small deformation mechanics, or a geometrically linear solution, which is typically applicable to more rigid bodies and structures characteristic of crystalline atomic structures, more common to structural alloys. Since solid polymer electrolyte batteries contain semi-crystalline polymer electrolytes that may be capable of larger elastic displacements which are

visually noticeable to an observer, the equations are adapted to consider geometric nonlinearity.

Finally, the concentration terms in these equations are then related to ionic conductivity via a key relationship per Sillamoni and Iadart [258], and the final equations are modified in order to develop a relationship between ionic conductivity and strain. The ionic conductivity of the electrolyte is an important design parameter in the battery, since ionic conductivity is a direct indication of the ability of the Li ions to diffuse through the electrolyte between the electrodes. This enhances the discussion from the previous chapter.

There are no closed-form solutions for the multivariable partial differential equations in this model that is developed, and therefore simplifications are made initially in order to obtain a relationship between ionic conductivity and strain, which is then compared with experimental data obtained from stretching a PEO electrolyte [12]. The model is also applied directly to the flexible battery design, with appropriately defined boundary conditions reflective of battery performance, and the model equations are solved numerically.

While much work has been completed to look into diffusion induced stress, what makes the work in this chapter new and insightful is that it looks at how stress or an applied strain field may influence mass diffusion, and subsequently takes a step further to determine how this impacts the ionic conductivity in the SPE. While much focus and observation on the relationship between ionic conductivity and applied

strain has been experimental, this work looks to provide more detail to enhance these observations with analytical models.

2. Analytical development

In order to carry out the analytical development, which will result in obtaining coupled mass diffusion and displacement equations, naturally a mass balance will be applied to the system, since matter is diffusing through the region of interest. This will be followed by applying thermodynamic laws which will yield an energy balance that will be used to obtain expressions for certain terms, namely stress and chemical potential. Following this development, the effects of geometric nonlinearity will be considered and discussed. The modeling efforts are based on continuum modeling techniques.

2.1 Mass balance

For this analytical development, an element P_t in body Ω with surface ∂P_t as shown in Figure 44 is considered [259]. This element may represent a region within the electrolyte, through which Li ions may diffuse.

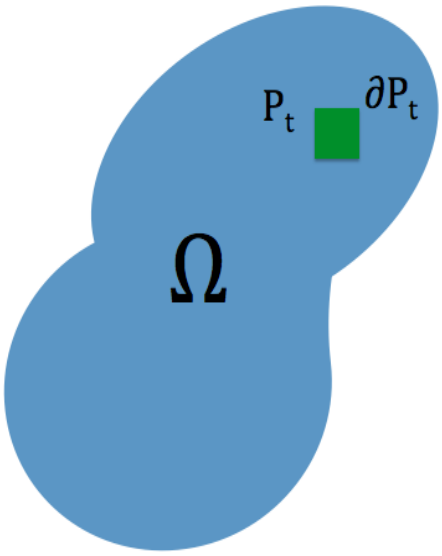

Figure 44: A geometric region of interest represented of body, Ω, with region P_t and surface $\boldsymbol{\partial P_t}$ [259].

A species may enter and exit the region, and flux may be modeled by considering this movement of mass. Concentration within the defined control volume can be represented using

$$\int_{P_t} N\rho dV = \int_{P_t} C dV, \tag{55}$$

where N is the species mass fraction, ρ is the density of solid body, C is the species concentration in the control volume, and V is the volume of the region. In order to obtain the flux, the equation is differentiated with respect to time to yield

$$\int_{P_t} \rho \dot{N} dV = \int_{P_t} \dot{C} dV = -\int_{\partial P_t} \boldsymbol{\phi} \cdot \mathbf{n} dA + \int_{P_t} h dV, \tag{56}$$

where ϕ is the species flux, n is a normal vector indicating flux direction, A indicates the surface area through which there is species flux, and h is a generation or source

term indicating supply or production of the species. It is important to note that Equation 56 contains dissimilar terms, specifically area and volume integrals, making it difficult to combine like terms into a single integral. Therefore, a transform is used to convert the integral containing flux into a volumetric integral. This transform is the Gauss divergence theorem, and is given by

$$\int_{\partial P_t} \boldsymbol{\phi} \cdot \mathbf{n} dA = \int_{P_t} div\boldsymbol{\phi} dV. \tag{57}$$

Applying the theorem and collecting like terms results in the following:

$$\int_{P_t} \left(\dot{C} + div\boldsymbol{\phi} - h\right) dV = 0, \tag{58}$$

$$\dot{C} + div\boldsymbol{\phi} - h = 0, \text{ and} \tag{59}$$

$$\frac{\partial C}{\partial t} + div\boldsymbol{\phi} = 0. \tag{60}$$

Differentiating the equation with respect to volume further simplifies the equation, and if there is no species supply or production, then h=0 is set. This equation can be used to model the mass diffusion throughout the region or control volume of interest.

2.2 Development of the total flux equation

For problems where mass is driven by a concentration gradient only, under steady state conditions, Fick's first law is adequate to represent mass diffusion within the system. For the flexible and stretchable battery application, where the battery undergoes an applied stress or strain field, it is inadequate to model

diffusion considering a concentration gradient only. It is possible for diffusion to be induced by a stress gradient within a system [255-257]. This is referred to as non-Fickian diffusion. It is known that depending on the available free volume, and host atomic configuration, both of which influence the ability of a species to diffusion through, local strains may develop in the host matrix due to swelling [257]. This is linked to what may drive non-Fickian diffusion. However, while concentration increase may cause swelling, also known as diffusion induced stress, an additional link to a stress induced diffusion due to an applied strain is of interest in this analytical development.

Accounting for both concentration and stress gradients as diffusion drivers, it is considered the total flux in a body can be represented by a summation of two flux terms [257, 259], shown as

$$\phi_{Total} = \phi(C) + \phi(\sigma), \tag{61}$$

where σ is the local stress tensor within associated with the region of interest. This comes directly from the mass balance, assuming steady state diffusion.

Since the particular material of interest is a polymer, it may be important to consider time dependency and viscoelasticity as part of the solution. The relationship to stress and diffusion, including viscoelasticity, has been studied by Ferreira and colleagues, who consider a new approach to non-Fickian diffusion within a body considering viscoelasticity, and propose the following equation [257]:

$$\frac{\partial C}{\partial t} = -\nabla \cdot D_C \nabla \mathrm{C} - \nabla \cdot D_\sigma \nabla \left(\sum_{i=1}^{n} \xi_i \int_0^\infty e^{\frac{1}{\omega_i}\int_s^t E_i(C(r))dr} \frac{\partial \varepsilon}{\partial s} ds \right) - \nabla \cdot D_\sigma \nabla \sigma, \quad (62)$$

where t is time, D_C is the Fickian diffusion coefficient dependent on temperature and free volume activation energy, D_σ is the non-Fickian diffusion coefficient which is a material parameter that may depend on an applied strain, ε is the local strain tensor, and ξ is the modulus of elasticity of the host matrix.

For simplification, only a steady state solution is of interest, where on a sufficiently long time scale, viscoelastic effects such as stress relaxation and strain creep are complete and the viscoelastic terms in the above equation are neglected. Therefore, Equation 62 can be simplified to account for the total flux, or diffusion of mass, and given as

$$\phi_{Total} = -D_C \nabla \mathrm{C} - D_\sigma \nabla \sigma = Cv, \quad (63)$$

where v is the velocity of the diffusing species. The total flux is simply governed by the rate of change of the diffusing species. Since the main driving force of a diffusing chemical species is the chemical potential gradient, which is directly related to the velocity of the diffusing species and total flux, the above equation can be modified to produce

$$v = -M \nabla \mu \text{ and} \quad (64)$$

$$\phi_{Total} = -MC \nabla \mu, \quad (65)$$

where μ is the chemical potential and M is the mobility tensor, which is tied to the ability of a species to diffuse through the region of interest. It is analogous to a

pressure drop in a pipe, which may drive fluid flow. In considering this expression, the total flux equation can be modified to be a balance between the gradients of concentration and stress, which are related to the gradient of chemical potential, shown as

$$D_C \nabla \mathrm{C} + D_\sigma \nabla \sigma = MC \nabla \mu. \quad (66)$$

2.3 System energy balance and thermodynamic continuum modeling

For this particular application, the concentration may be directly specified. The terms that are unknown are the chemical potential, μ, and the stress, σ, and therefore it is useful to determine an expression for chemical potential and for stress in terms of concentration. In order to accomplish this, a continuum modeling approach is considered by applying the 1st and 2nd Laws of Thermodynamics [185].

Applying the 1st Law of Thermodynamics to the system, specifically on the region of interest, results in the energy balance given by

$$Q = W - \frac{dE}{dt}, \quad (67)$$

where Q is the heat dissipation, W is the system rate of work, or power, and E is the total internal energy of the system. An additional term, U, is defined, which is the volumetric internal energy given by

$$E = \int_{P_t} U(\nabla u, C) dV \text{ and} \quad (68)$$

$$W = \int_{\partial P_t} \boldsymbol{t^e} \cdot \mathbf{v} dA - \int_{\partial P_t} \mu \boldsymbol{\phi} \cdot \mathbf{n} dA + \int_{P_t} \mu h dV, \quad (69)$$

where t_e is an applied surface traction, and as before, v and n denote velocity and normal vector directionality. As before, in the rate of work equation, unlike integrals are contained due to surface and volumetric terms. Therefore, again applying the divergence theorem like integral terms can be simplified and combined. Assuming that the source or production term does not contribute (h=0), rearrangement of terms using the differentiation product rule yields the following:

$$-\int_{\partial P_t} \mu\boldsymbol{\phi}\cdot\mathbf{n}dA = -\int_{P_t} div(\mu\boldsymbol{\phi})dV, \tag{70}$$

$$-\int_{\partial P_t} \mu\boldsymbol{\phi}\cdot\mathbf{n}dA = -\int_{P_t} [\mu div(\boldsymbol{\phi}) + \boldsymbol{\phi}\cdot\nabla\mu]dV, \tag{71}$$

$$-\int_{\partial P_t} \mu\boldsymbol{\phi}\cdot\mathbf{n}dA = -\int_{P_t} \left[\mu\left(h-\dot{C}\right) + \boldsymbol{\phi}\cdot\nabla\mu\right]dV, \text{ and} \tag{72}$$

$$W = \int_{\partial P_t} \boldsymbol{t^e}\cdot\mathbf{v}dA - \int_{P_t}\left(\boldsymbol{\phi}\cdot\nabla\mu - \mu\dot{C}\right)dV. \tag{73}$$

It is assumed that the volumetric internal energy is a function of both the strain and concentration within the region. By making this assumption the chain rule is applied, where u represents the displacement field of the region, the gradient of which produces strain. Taking the expressions, the rate of work and rate of change of internal energy are plugged back into Equation 67 to yield

$$\frac{dE}{dt} = \int_{P_t} \dot{U}(\nabla u, C)dV = \int_{P_t}\left[\dot{C}\frac{\partial U}{\partial C} + \nabla\mathbf{v}\frac{\partial U}{\partial \nabla u}\right]dV \text{ and} \tag{74}$$

$$Q = \int_{P_t}\left[\mu - \frac{\partial U}{\partial \mathrm{C}}\right]\dot{C}dV + \int_{P_t} \mathrm{div}\left(\frac{\partial U}{\partial \nabla u}\right)\cdot\mathbf{v}dV + \int_{\partial P_t}\left[\boldsymbol{t^e} - \frac{\partial U}{\partial \nabla u}\mathbf{n}\right]\cdot\mathbf{v}dA - \int_{P_t}\boldsymbol{\phi}\cdot\nabla\mu dV. \tag{75}$$

Holding the system to obeying the 2nd Law of Thermodynamics, it follows that $Q \geq 0$. In order for this to hold, $\boldsymbol{\phi}\cdot\nabla\mu \leq 0$. The terms in Equation 75 were strategically

rearranged in order for useful expressions to be derived to define key terms that will be considered later, which include the following:

$$\varepsilon = \frac{1}{2}(\nabla \mathbf{u} + \nabla \mathbf{u}^{T}), \tag{76}$$

$$\sigma = \left(\frac{\partial U}{\partial \varepsilon}\right)_{C}, \tag{77}$$

$$\mu = \left(\frac{\partial U}{\partial \mathrm{C}}\right)_{\varepsilon}, \tag{78}$$

$$div\boldsymbol{\sigma} = 0, \text{ and} \tag{79}$$

$$\boldsymbol{\sigma} \cdot \mathbf{n} = \boldsymbol{t}^{e}. \tag{80}$$

Using these definitions, expressions for both the stress and chemical potential can be derived. This approach requires that the volumetric internal energy of the system be known, or that it may be represented by a functional expression in terms of concentration and strain. This derivation will be discussed in the following development.

2.4 Small deformation development: linear geometry

As before, consideration of geometric nonlinearity, or large deformation, will influence the solution. Initially small deformations within the structure were assumed for simplicity, which is consistent with deformation in the elastic response regions of many materials with a crystalline lattice structure.

As previously stated, the internal energy must be known or prescribed in order to obtain expressions for chemical potential and stress. It is often convenient, and accurate, to represent the volumetric internal energy as a sum of the contributions

due to elastic strain energy, diffusional strain, and concentration change [185], which is given as

$$U = \frac{1}{2}\nabla \mathrm{u} \cdot \mathbb{C}\nabla \mathrm{u} + \alpha(C - C_o)Tr(\nabla u) + RTC\left[ln\left(\frac{C}{C_o}\right) - 1\right], \quad (81)$$

where $\mathbb{C}$ is the fourth order stiffness tensor, which is a term that represents directionally dependent material stiffness, which is useful for considering isotropic or anisotropic material properties, and RT is simply the product of temperature and Universal Gas Constant. This expression derives from the Boltzmann thermodynamic relation [255].

Rewriting the differential of volumetric internal energy as a sum of the partial derivatives of internal energy with respect to both strain and concentration, and considering the relations shown in Equations 77-78, yields

$$dU = \frac{\partial U}{\partial \nabla u}\Big|_C d\nabla u + \frac{\partial U}{\partial C}\Big|_\varepsilon dC, \quad (82)$$

$$\mu = \frac{\partial U}{\partial C}\Big|_F = \alpha\nabla \cdot u + RTln\left(\frac{C}{C_o}\right), \text{ and} \quad (83)$$

$$\sigma = \frac{\partial U}{\partial \nabla u}\Big|_C = \mathbb{C}\nabla u + \alpha(C - C_o)\mathbf{I}. \quad (84)$$

Using Equations 83-84 and plugging them back into the original expression for total flux produces

$$D_C\nabla \mathrm{C} + D_\sigma\nabla[\mathbb{C}\nabla u + \alpha(C - C_o)\mathbf{I}] = MC\nabla\left[\alpha\nabla \cdot u + RTln\left(\frac{C}{C_o}\right)\right]. \quad (85)$$

This equation is now in terms of two parameters: displacement and concentration. This is convenient since for the battery application a strain or displacement field can be specified leaving concentration as the dependent variable in the system.

2.5 Large deformation development: consideration of nonlinear geometry

In many cases it is often necessary to consider large deformation mechanics and nonlinear geometry, particularly for materials that are capable of visually large elastic stretch. This is typical of stretchable polymers and elastomers with Poisson ratios closer to 0.4-0.5 composed of amorphous and tangled molecular chains. This may also hold true for semi-crystalline polymers with lower degrees of crystallinity.

In the previous section considering small deformation mechanics, substantial volume change and displacement difference between the unstrained and strained conditions of the region were thought to be very small. In the large deformation solution, the changes between the reference (unstrained) state and the current (strained) condition must be considered, since the local spatial coordinate changes between these two states may not be negligible.

It is important to define a number of variables for this development including y, which is the coordinate position of the current configuration; x, which is the coordinate position of the reference configuration; F, which is the deformation tensor, which differs from the strain tensor since it is in terms of stretch terms rather than strain terms; J, which is the Jacobian that represents the volume change of the region from the current to the reference configuration; and T, which is the 1st

Piola-Kirchhoff stress tensor, which is related to the Cauchy stress tensor, σ, via the Jacobian and the inverse and the deformation tensor [185]. An important item to note in the process of developing a solution considering large deformation is that the reference state and current state configurations can be mapped to each other via the Jacobian term. This is shown in the following:

$$y(x) = x + u(x), \tag{86}$$

$$\mathbf{F} = \nabla_x y, \tag{87}$$

$$J = det\mathbf{F} > 0, \tag{88}$$

$$dV^y = \mathrm{JdV}^x, \tag{89}$$

$$\mathrm{N}^y = \mathbf{F}^{-\boldsymbol{T}}\mathrm{N}^x, \tag{90}$$

$$(\mathbf{n}dA)^y = \mathrm{J}\mathbf{F}^{-\boldsymbol{T}}(\mathbf{n}dA)^x, \tag{91}$$

$$C^y = J^{-1}C^x, \tag{92}$$

$$\dot{C^y} + div\boldsymbol{\phi}^y - h^y = 0, \text{ and} \tag{93}$$

$$\dot{C^x} + div\boldsymbol{\phi}^x - h^x = 0, \tag{94}$$

where the superscripts ^{x} and ^{y} denote the reference state and current state, respectively. Referring back to the energy balance that was previously obtained using the 1st Law of Thermodynamics, the terms of rate of work and rate of change of internal energy must be modified to include the newly defined variables in current configuration. Consideration of the deformation tensor, and the area, volume, and coordinate position associated with the current configuration, are given by the following:

$$W = \int_{\partial P_t} \boldsymbol{t^e} \cdot \dot{\mathbf{y}} dA - \int_{\partial P_t} \mu \boldsymbol{\phi} \cdot \mathbf{n} da + \int_{P_t} \mu h dV, \tag{95}$$

$$\frac{dE}{dt} = \int_{P_t} \dot{U}(\mathbf{F}, C) dV = \int_{P_t} \left[\dot{C} \frac{\partial U}{\partial C} + \dot{\mathbf{F}} \frac{\partial U}{\partial \mathbf{F}} \right] dV, \text{ and} \tag{96}$$

$$Q = \int_{P_t} \left[\mu - \frac{\partial U}{\partial \mathrm{C}} \right] \dot{C} dV + \int_{P_t} \operatorname{div} \left(\frac{\partial U}{\partial \mathbf{F}} \right) \cdot \dot{\boldsymbol{y}} dV + \int_{\partial P_t} \left[\boldsymbol{t^e} - \left(\frac{\partial U}{\partial \mathbf{F}} \right)^T \mathbf{N} \right] \cdot \dot{\boldsymbol{y}} dA - \int_{P_t} \boldsymbol{\phi} \cdot \nabla \mu dV. \tag{97}$$

Again holding the system to obeying the 2nd Law of Thermodynamics, it follows that $Q \geq 0$. As before, in order for this to hold, it follows that $\boldsymbol{\phi} \cdot \nabla \mu \leq 0$. The terms in Equation 97 were again rearranged in order for useful expressions to be derived to define key terms that will be considered later. These terms are defined with respect to the current configuration considering nonlinear geometric effects, shown in the following:

$$\boldsymbol{t^e} - \left(\frac{\partial U}{\partial \mathbf{F}} \right)^T \mathbf{n} = 0, \tag{98}$$

$$\mathbf{T} = \left(\frac{\partial U}{\partial \mathbf{F}} \right)_C, \tag{99}$$

$$\mu = \left(\frac{\partial U}{\partial \mathrm{C}} \right)_F, \tag{100}$$

$$div \boldsymbol{T} = 0, \text{ and} \tag{101}$$

$$\boldsymbol{\phi} \cdot \mathbf{n} = \text{Constant}. \tag{102}$$

The 1st Piola-Kirchhoff stress tensor must be defined to show how it is related to the Cauchy (true) spatial stress tensor. This is given by

$$\mathbf{T} = \mathrm{J} \mathbf{F^{-1}} \boldsymbol{\sigma}. \tag{103}$$

As was done previously, the internal energy potential can now be modified to account for the geometrically nonlinear terms, which include the deformation tensor and consideration of the current configuration [185]. Accounting for the current configuration terms yields

$$U = \frac{1}{2}(\mathbf{F} - I) \cdot \mathbb{C}(\mathbf{F} - I) + \alpha(C - C_o)Tr\mathbf{F} + RTC\left[ln\left(\frac{C}{C_o}\right) - 1\right]. \quad (104)$$

Equation 66 can then be augmented to account for the large deformation terms, specifically the 1st Piola-Kirchhoff stress tensor as shown in

$$D_C \nabla \mathrm{C} + D_\sigma \nabla \mathbf{T} = MC\nabla\mu. \quad (105)$$

2.6 Large deformation materials model

In order to obtain an expression that relates displacement to concentration considering nonlinear geometry, it is convenient to account for the behavior of the material since the equations in large deformation consider volume change and deformation stretch behavior. In this work, for simplicity, the Neo-Hookean Hyperelastic materials model with isotropic material properties is assumed. This is especially appropriate for electrolyte materials capable of large elastic stretches, particularly ones with low crystallinity and Poisson's ratios approaching 0.5. Applying this materials model transforms the internal energy equation to

$$U = \frac{G}{2}(I_{F1} - 3) + \frac{K}{2}(J - 1)^2 + \alpha(C - C_o)Tr\mathbf{F} + RTC\left[ln\left(\frac{C}{C_o}\right) - 1\right], \quad (106)$$

where G is the shear modulus, K is the bulk modulus, and I_{F1} is the first invariant of the deformation tensor. Considering again that the differential of volumetric internal energy is a sum of the partial derivatives of internal energy with respect to both deformation and concentration, applying the chain rule the derivatives with respect to the Jacobian and the deformation tensor invariant can be obtained to yield the following:

$$dU = \left.\frac{\partial U}{\partial \mathbf{F}}\right|_C d\mathbf{F} + \left.\frac{\partial U}{\partial C}\right|_F dC, \tag{107}$$

$$dU = \left.\frac{\partial U}{\partial I_{F1}}\frac{\partial I_{F1}}{\partial \mathbf{F}}\right|_C d\mathbf{F} + \left.\frac{\partial U}{\partial J}\frac{\partial J}{\partial \mathbf{F}}\right|_C d\mathbf{F} + \left.\frac{\partial U}{\partial C}\right|_F dC, \tag{108}$$

$$\mu = \left.\frac{\partial U}{\partial C}\right|_F = \alpha(\mathbf{F} - I) \cdot I + RTln\left(\frac{C}{C_o}\right), \text{and} \tag{109}$$

$$\mathbf{T} = \left.\frac{\partial U}{\partial \mathbf{F}}\right|_C = GJ\mathbf{F}^T - J\mathrm{p}\mathbf{F}^{-1} + \alpha(C - C_o)\mathbf{I}. \tag{110}$$

The expressions for chemical potential and Piola-Kirchhoff stress are obtained from this expansion. A term that results in Equation 110 is p, which is referred to as the indeterminate pressure. This is an internal hydrostatic pressure term associated with the material stress, which can be solved if the applied internal forces are known.

Another important assumption is that of incompressible behavior for the material. This is an appropriate assumption for many polymers and elastomer materials, since their Poisson's ratios approach the incompressibility limit. By assuming that the material is incompressible, there is no volume change, and therefore the Jacobian simplifies to $J = 1$. Assuming that the dimensions of the

region of interest can be represented by length terms, as shown in Figure 45 [259], the volume and the stretch can be determined from

$$V = L_1 L_2 L_3 = l_1 l_2 l_3 \text{ and} \tag{111}$$

$$\lambda_i = \frac{l_i}{L_i}. \tag{112}$$

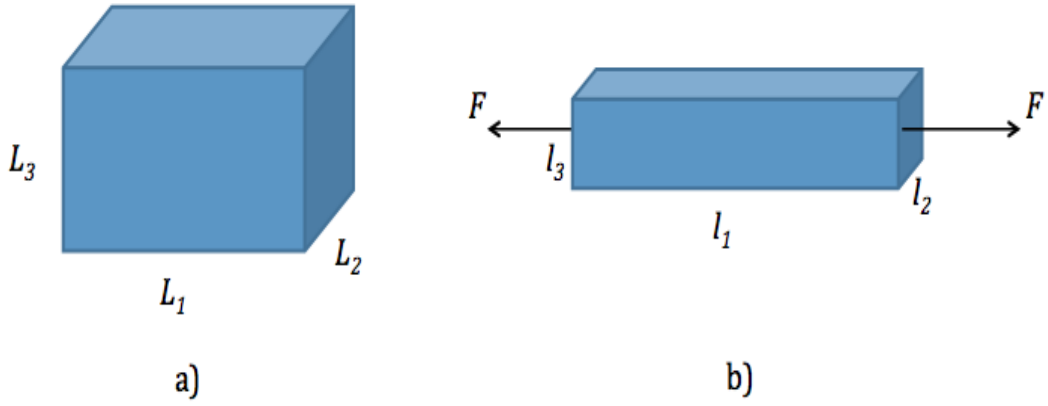

Figure 45: Dimensional representation of the region of interest in the a) reference and b) current configurations [259].

Applying these assumptions, the Piola-Kirchhoff stress and the chemical potential can be substituted into Equation 105 to yield

$$D_C \nabla \mathrm{C} + D_\sigma \nabla [G\mathbf{F}^T - \mathrm{p}\mathbf{F}^{-1} + \alpha(C - C_o)\mathbf{I}] = MC\nabla \left[\alpha(\mathbf{F} - I) \cdot I + RTln\left(\frac{C}{C_o}\right)\right]. \tag{113}$$

This provides a relationship between concentration and deformation, where either a displacement field or deformation can be specified on the body. This allows for the concentration to be solved spatially under an applied displacement field.

3. Numerical solution

The equations derived in the previous section require definition of boundary conditions based on the physics at the system boundary in order to obtain a solution. The first objective to evaluate these equations is to model the stretching experiment of a PEO electrolyte that was conducted in our lab [12]. However, in their current form, it is difficult to obtain closed-form solutions from these equations without further simplification. In this section, simplifying assumptions are made and to define boundary conditions to numerically model the stretching experiment.

Referring back to the stretching experiment, the ionic conductivity of a PEO electrolyte sample was measured for an applied uniaxial strain. That experiment considered an electrolyte sample of PEO only, in air, and a fixed strain was applied using a tensile test machine. As previously discussed, the experiment showed an increase in ionic conductivity with applied strain. The following sections will take the coupled mass diffusion/strain equations derived in the previous section and modify them in order to relate strain to ionic conductivity. The equations will be simplified to more accurately model the experiment.

3.1 Small deformation assumption

Since the experiment was based on a sample of PEO under an applied uniaxial tension, Equation 81 will be simplified to consider a 1-D uniaxial deformation, assuming isotropic material properties, and a small deformation or linearly

geometric solution. In this case, only with strain in the direction of applied tension is of interest. Using this assumption, the internal energy term can be simplified to

$$U = \frac{1}{2}\xi\varepsilon^2 + \alpha(C - C_o)\varepsilon + RTC\left[ln\left(\frac{C}{C_o}\right) - C\right]. \quad (114)$$

From this expression, a simplified expression for chemical potential can be obtained and plugged into Equation 66 to yield the following:

$$dU = \left.\frac{\partial U}{\partial \varepsilon}\right|_C d\varepsilon + \left.\frac{\partial U}{\partial C}\right|_\varepsilon dC, \quad (115)$$

$$\mu = \left.\frac{\partial U}{\partial C}\right|_\varepsilon = \alpha\varepsilon + RTln\left(\frac{C}{C_o}\right), \text{ and} \quad (116)$$

$$D_C\frac{\mathrm{dC}}{\mathrm{dx}} + D_\sigma\frac{\mathrm{d\sigma}}{\mathrm{dx}} = MC\frac{d}{dx}\left[\alpha\varepsilon + RTln\left(\frac{C}{C_o}\right)\right]. \quad (117)$$

An applied strain can be prescribed for the specimen. Since a linear relationship exists between the applied strain, and the stress via Hooke's law, for a uniaxial applied strain considering linear geometry, the stress across the sample in the direction of applied strain is uniform. Therefore, that term goes to zero. The dependent variable in this case is the concentration. Since the sample is in air, and no mass flux crosses the boundary of the PEO electrolyte, the following boundary conditions are applied for the concentration for a sample of length, L:

$$\left.\frac{dC}{dx}\right|_{x=0} = \left.\frac{dC}{dx}\right|_{x=L} = 0. \quad (118)$$

Considering these boundary conditions, at steady state when chemical potential across the sample is uniform, there would be no concentration gradient across the

electrolyte in experiment. Therefore, applying these conditions, Equation 117 can be simplified to

$$0 = \alpha\varepsilon + RTln\left(\frac{C}{C_o}\right). \quad (119)$$

The ionic conductivity of the sample, in this case in the direction of the applied strain, can be related directly to concentration using a relationship from Sillamoni and Iadart [258], using the following expression:

$$\psi = (FZ)^2 MC, \quad (120)$$

where ψ is the ionic conductivity of the sample, F is Faraday's constant, and Z is the valency. Rearranging the equation to solve for concentration, and plugging into Equation 120 yields

$$C = (FZ)^{-2} M^{-1} \psi \text{ and} \quad (121)$$

$$0 = \alpha\varepsilon + RTln\left[\frac{(\psi/M)}{(\psi/M)_0}\right]. \quad (122)$$

It is important to discuss the physical implications of the mobility tensor. The mobility tensor is related to the ability of a species to diffuse through a host matrix. In this case, the component of mobility associated with the direction of applied strain is of interest. In a semi-crystalline polymer, the mobility tensor can vary spatially whether the species may be diffusing through a crystalline or an amorphous region. There is increased mobility in the amorphous region for the reasons described in Chapter 5. The experiment measures ionic conductivity for the

sample as a whole, rather than a spatial measurement of ionic conductivity within the sample. Therefore, in the analysis, the mobility term in the equation will receive a similar treatment, and will be defined as an average across the sample. Since small deformation or linear geometry is being considered, for a small applied elastic strain, $M_\varepsilon \approx M_0$, since the material lattice is not expected to change considerably for a small elastic strain. This requires referring back to the deformation mechanisms that were described in Chapter V, with consideration to the deformation in the elastic region. Applying this assumption, and rearranging Equation 122 yields

$$\frac{\Delta\psi}{\psi_0} = exp\left(\frac{-\alpha\varepsilon}{RT}\right) - 1, \qquad (123)$$

which provides an expression for change in ionic conductivity normalized by the initial ionic conductivity.

3.2 Large deformation solution

Again the 1-D uniaxial applied tension is considered, and the same boundary conditions are applied for modeling the experiment, but geometric nonlinearity is considered. For simplification, isotropic material properties are assumed, and the material is also assumed to be incompressible. Under this assumption, for a uniaxial applied stretch, the resulting deformation tensor, transform of the deformation tensor, inverse of the deformation tensor, and strain, which is the difference of the deformation tensor and identity matrix are shown in the following:

$$\mathbf{F} = \begin{vmatrix} \lambda & 0 & 0 \\ 0 & -\lambda^{-1/2} & 0 \\ 0 & 0 & -\lambda^{-1/2} \end{vmatrix}, \tag{124}$$

$$\mathbf{F}^T = \begin{vmatrix} \lambda & 0 & 0 \\ 0 & -\lambda^{-1/2} & 0 \\ 0 & 0 & -\lambda^{-1/2} \end{vmatrix}, \tag{125}$$

$$\mathbf{F}^{-1} = \begin{vmatrix} \lambda^{-1} & 0 & 0 \\ 0 & \lambda^{1/2} & 0 \\ 0 & 0 & \lambda^{1/2} \end{vmatrix}, \text{and} \tag{126}$$

$$\mathbf{F} - \mathbf{I} = \begin{vmatrix} \lambda - 1 & 0 & 0 \\ 0 & -\lambda^{-1/2} - 1 & 0 \\ 0 & 0 & -\lambda^{-1/2} - 1 \end{vmatrix}. \tag{127}$$

In this case, the strain term is substituted for the trace of the tensor. For large deformation modeling, it may not be appropriate to assume that the mobility term does not change with applied elastic strain, particularly for large percent strain. This may be consistent with elastomers and polymers with low degrees of crystallinity, with greater amorphous grains, due to chain sliding and extension. The final expression for relating ionic conductivity to deformation using large deformation mechanics and nonlinear geometry yields

$$\psi = \psi_o M_\lambda M_o^{-1} exp\left[-\frac{\alpha}{RT}\left(\lambda - 2\lambda^{-1/2} - 3\right)\right]. \tag{128}$$

4. Comparison with experimental data

The PEO sample considered in the stretching experiment, described in Chapter V, has a higher degree of crystallinity, which results in a small elastic range. Furthermore, increased deformation at higher strains, particularly in regions approaching and exceeding yielding of the sample, the assumption that the mobility

term does not change with increasing strain, $M_\varepsilon \approx M_0$, may not be appropriate. This would require materials data for a value of mobility change. For the purposes of correlating the model to the experimental data, using Equation 123 and considering small deformation for applied elastic strain would be an appropriate assumption, since the data is for relatively low strain for a PEO sample with high crystallnity (60-80%). Figure 46 provides a plot of the numerical curve created from the analytical model, along with measured ionic conductivity data from the experiment, provided courtesy of [12].

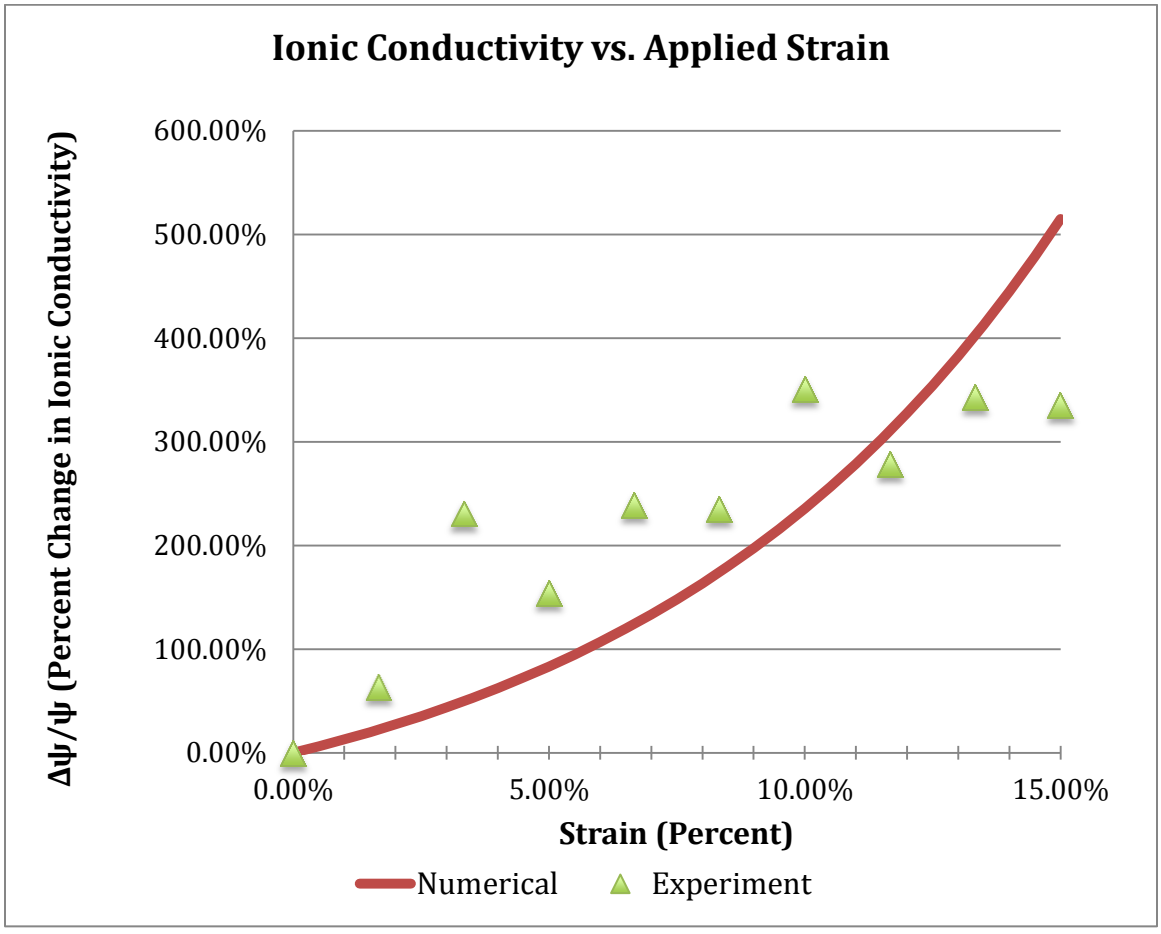

Figure 46: Plot of percent change in ionic conductivity vs. applied uniaxial strain comparing numerical result with experimental result [12].

It is clearly depicted that the ionic conductivity increases with an applied strain, and follows the experimental data. The numerical data supports this increasing trend, since the percent change in ionic conductivity for applied uniaxial strain is directly proportional to the strain term via an exponential expression. It is important to note that it is assumed that α is an experimentally determined constant that is a negative value, which results in the exponential increase in ionic conductivity. This is supported in literature, which proposes that the chemical potential is directly related to the hydrostatic stress state and the stress triaxiality [255]. Since chemical potential is a driving force for diffusion, and diffusion is composed of both Fickian and non-Fickian terms, it is important to consider more deeply the driving mechanism for each term. In Fickian diffusion a concentration gradient drives diffusion, where species migrate from high concentration to low concentration. This indicates that concentration is directly related to chemical potential, since species flow from a region of higher chemical potential to lower chemical potential. Applying this principle, if chemical potential is proportional to a negative stress field, this indicates that the flow of species will be from a local compressive to a tensile stress field along a stress gradient. Whether the field is tensile or compressive is dictated by the hydrostatic stress state, and the stress triaxiality. Physically this is intuitive, since a species is likely to be driven out of a compressive zone to a region in tension.

5. Direct application to lithium ion battery

Previously the diffusion and ionic conductivity model was simplified, and boundary conditions were applied to more closely model the extension experiment as previously described. The boundary conditions in that case were such that the concentration flux was negligible or zero at all boundaries, a fixed ion concentration resided within the sample, and the applied strain resulted in a uniform stress field across the sample, and therefore there was no stress gradient across the sample. For an electrolyte that would perform in a lithium ion battery, a different set of boundary conditions must be considered.

The stretchable and flexible lithium ion battery designs consist of an electrolyte that is sandwiched between two electrodes. During the intercalation process, the Li ions permeate the electrolyte entering from the cathode and pass through to complete the formation reaction with the anode. Appropriate boundary conditions to model this process would consist of approximating a constant flux boundary condition at the cathode/electrolyte interface, and an outflow boundary condition at the anode/electrolyte surface. Depending on the strain field under consideration, and whether nonlinear geometry is considered, based on the model developed in this chapter, the ionic conductivity in the electrolyte would be expected to vary spatially throughout the sample, depending on the local stress field and applied strain.

In order to determine the ionic conductivity variation throughout an electrolyte when functioning in a LIB, the equations were solved using numerical methods for the conditions described above. Since the uniaxial tensile experiment yields a somewhat trivial result, i.e., no strain gradient across the sample, a flexible SPE LIB was modeled assuming an applied bending load. This is because these equations hold for either flexible or stretchable battery models. The partial differential equations were simplified to 2-D space, assuming a 2-D PEO electrolyte sample, since the bending results in a strain and concentration flux in the in-plane direction. A flexible battery subject to bending was modeled using a finite element analysis, similar to that described in Chapters II and III, and the flexible battery was bent to two different curvatures (approximately 10 mm and 2 mm). The strain field was extracted from the finite element model considering small deformation and nonlinear geometry at each bending radius, and these values were plugged into Equations 85 and 113, which were then solved using numerical methods. Details of this solution method are described in Appendix B. A diagram illustrating the space considered for the battery is shown in Figure 47.

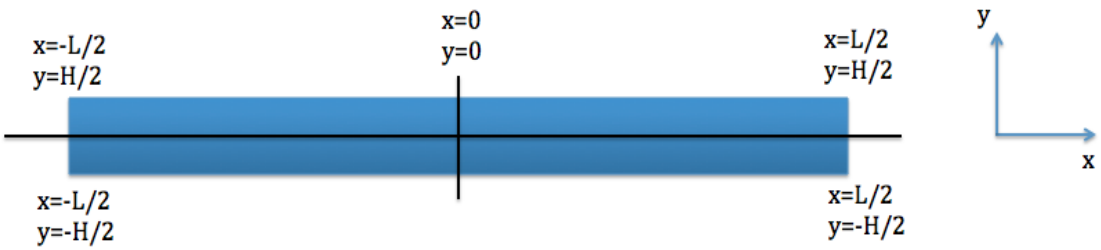

Figure 47: Diagram illustrating the size and space of the electrolyte considered for the numerical analysis [259].

The following boundary conditions were defined for concentration within the model:

$$\frac{\partial}{\partial x}[C(-L/2, y)] = 0, \quad (129)$$

$$\frac{\partial}{\partial x}[C(L/2, y)] = 0, \quad (130)$$

$$\frac{\partial}{\partial x}[C(x, H/2)] = \phi_B/D, \text{ and} \quad (131)$$

$$\frac{\partial}{\partial x}[C(x, -H/2)] = \phi_{OF}/D, \quad (132)$$

where ϕ_B and ϕ_{OF} represent the inflow and outflow ion fluxes from the electrodes at the top and bottom boundaries of the electrolyte. The ionic conductivity was then calculated as a function of (x,y) location within the 2-D electrolyte under bending. These values of ionic conductivity were normalized with a sample in an unstrained state, to produce a percent change in ionic conductivity. Figures 48-55 provide the plots of the ionic conductivity throughout the electrolyte sample as a function of (x,y) location, which include both surface plots and contour plots. Both small deformation and large geometry solutions are provided for comparison.

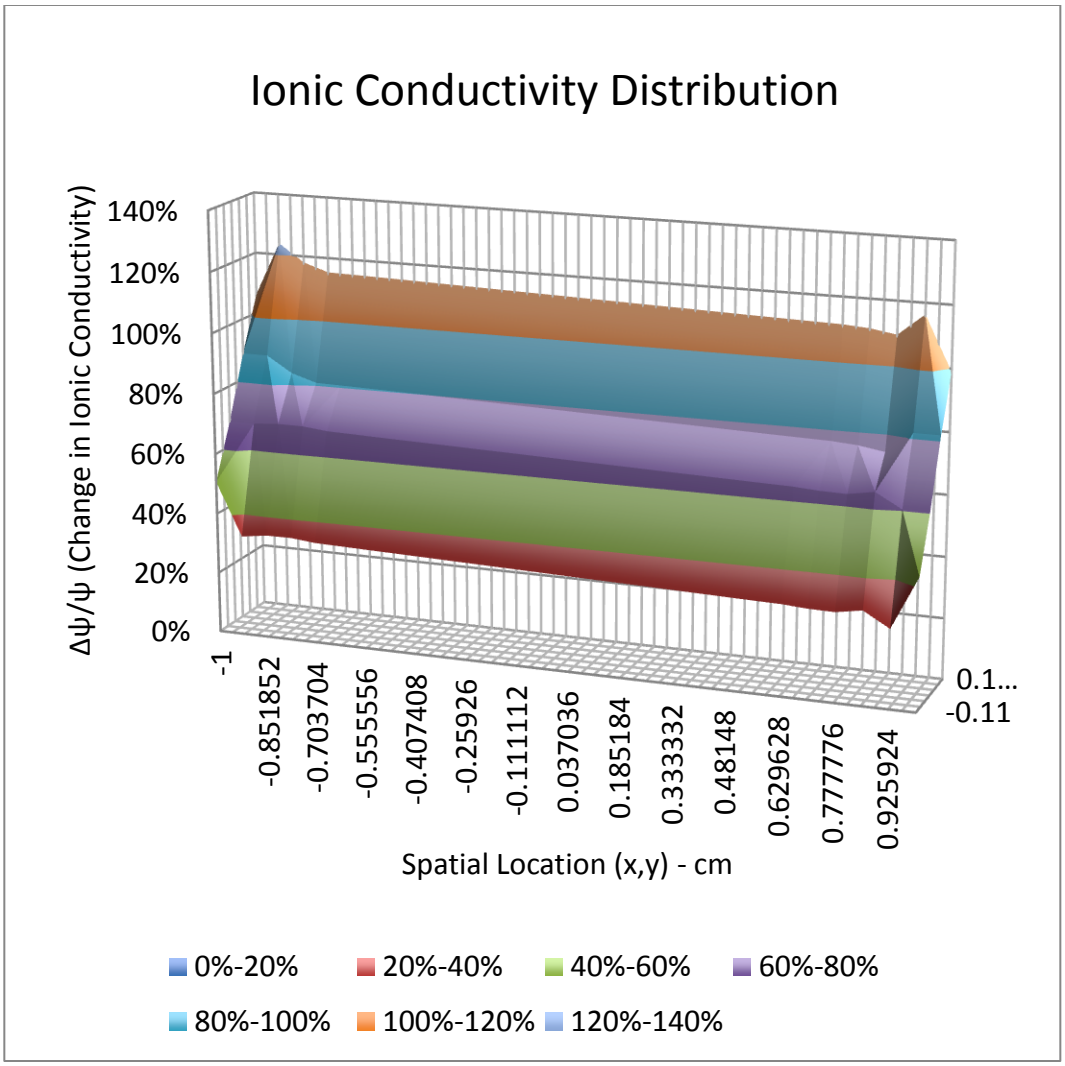

Figure 48: Surface plot illustrating percent change in ionic conductivity spatially with applied bending stress field (small deformation assumption, bending curvature radius of 10 mm) [259].

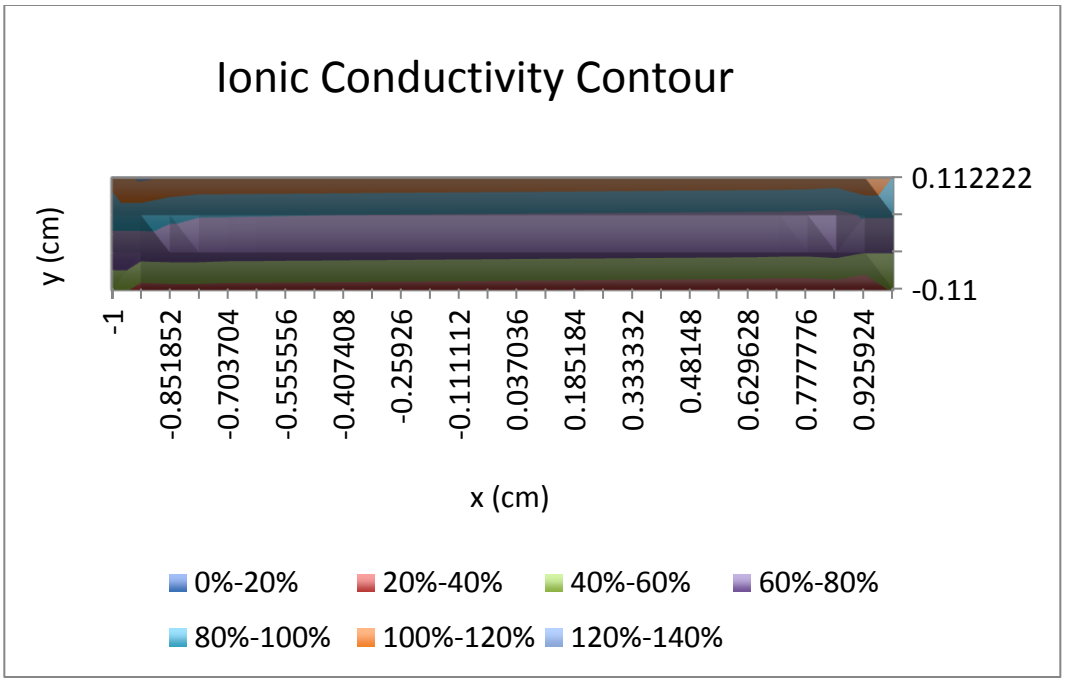

Figure 49: Contour plot illustrating percent change in ionic conductivity spatially with applied bending stress field (small deformation assumption, bending curvature radius of 10 mm) [259].

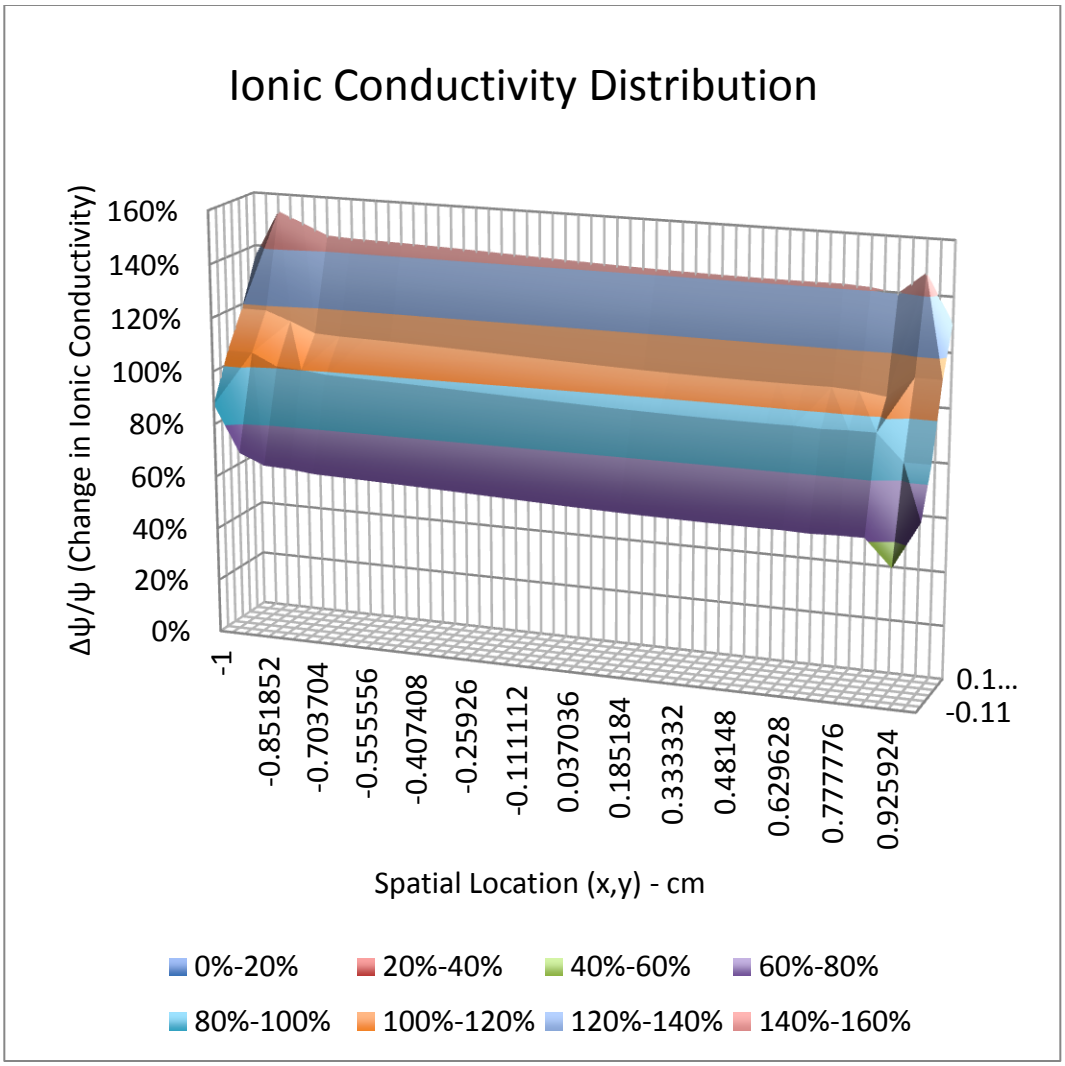

Figure 50: Surface plot illustrating percent change in ionic conductivity spatial with applied bending stress field (nonlinear geometry considered, bending curvature radius of 10 mm) [259].

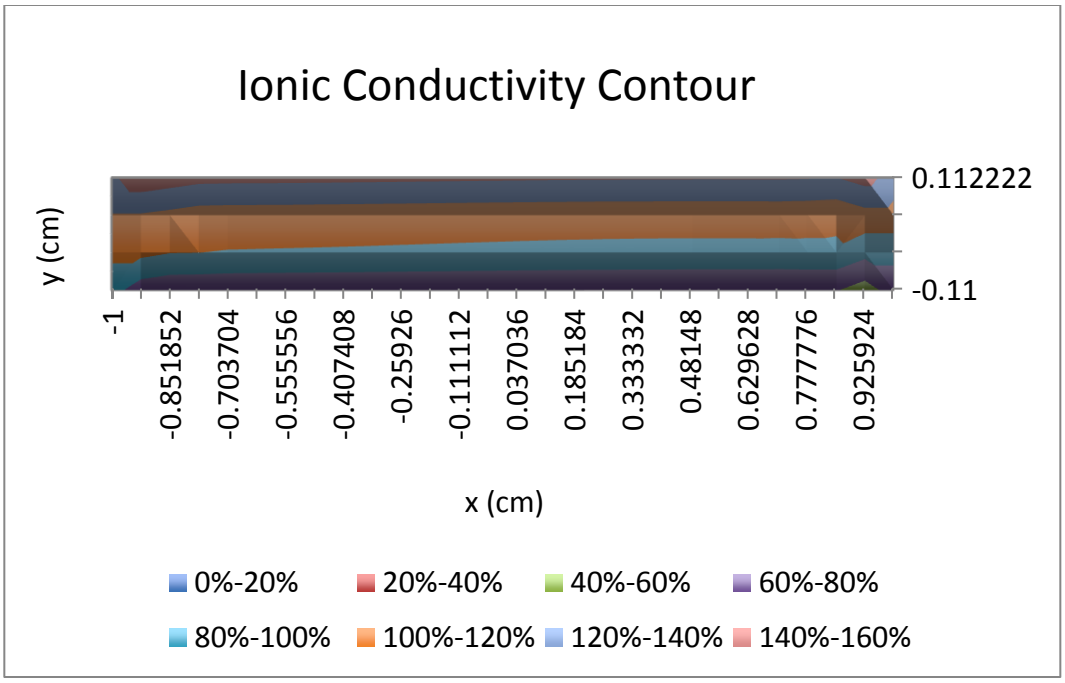

Figure 51: Contour plot illustrating percent change in ionic conductivity spatial with applied bending stress field (nonlinear geometry considered, bending curvature radius of 10 mm) [259].

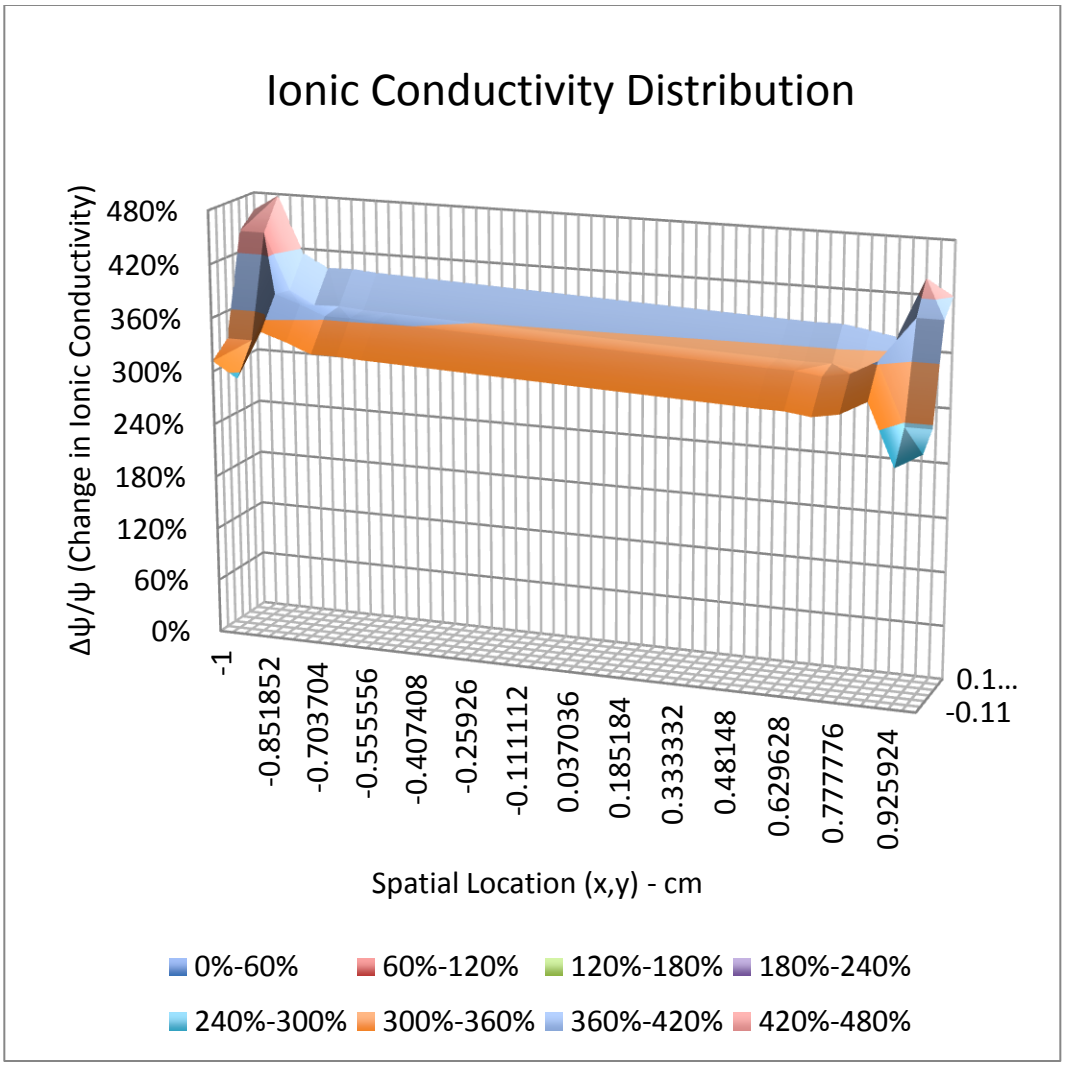

Figure 52: Surface plot illustrating percent change in ionic conductivity spatial with applied bending stress field (small deformation assumption, bending curvature radius of 2 mm) [259].

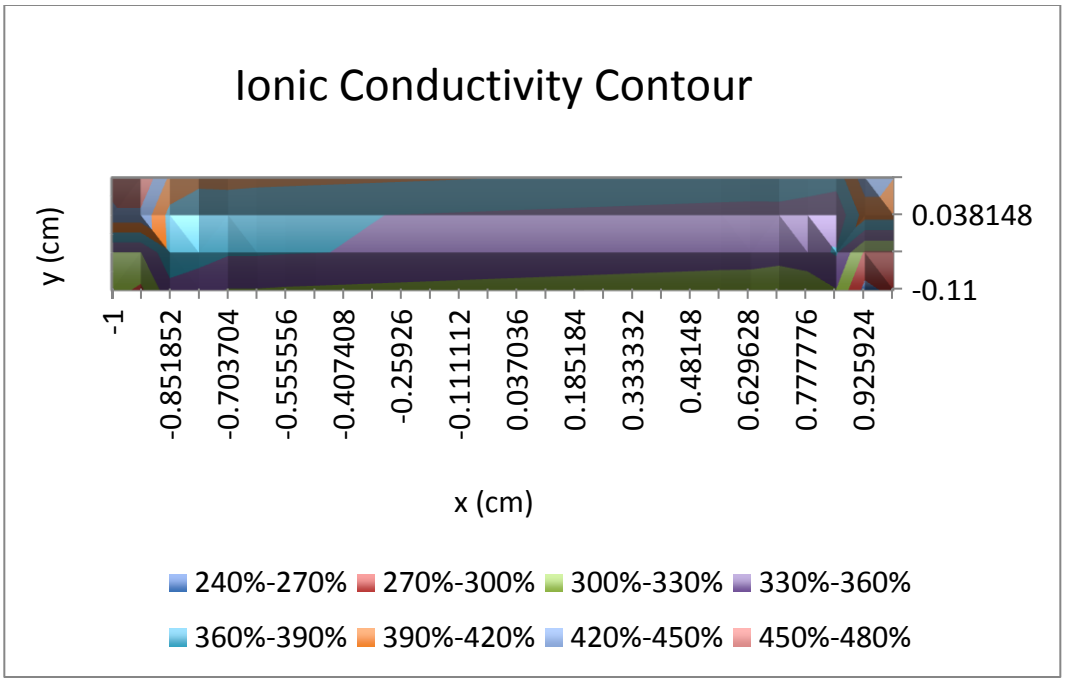

Figure 53: Contour plot illustrating percent change in ionic conductivity spatial with applied bending stress field (small deformation assumption, bending curvature radius of 2 mm) [259].

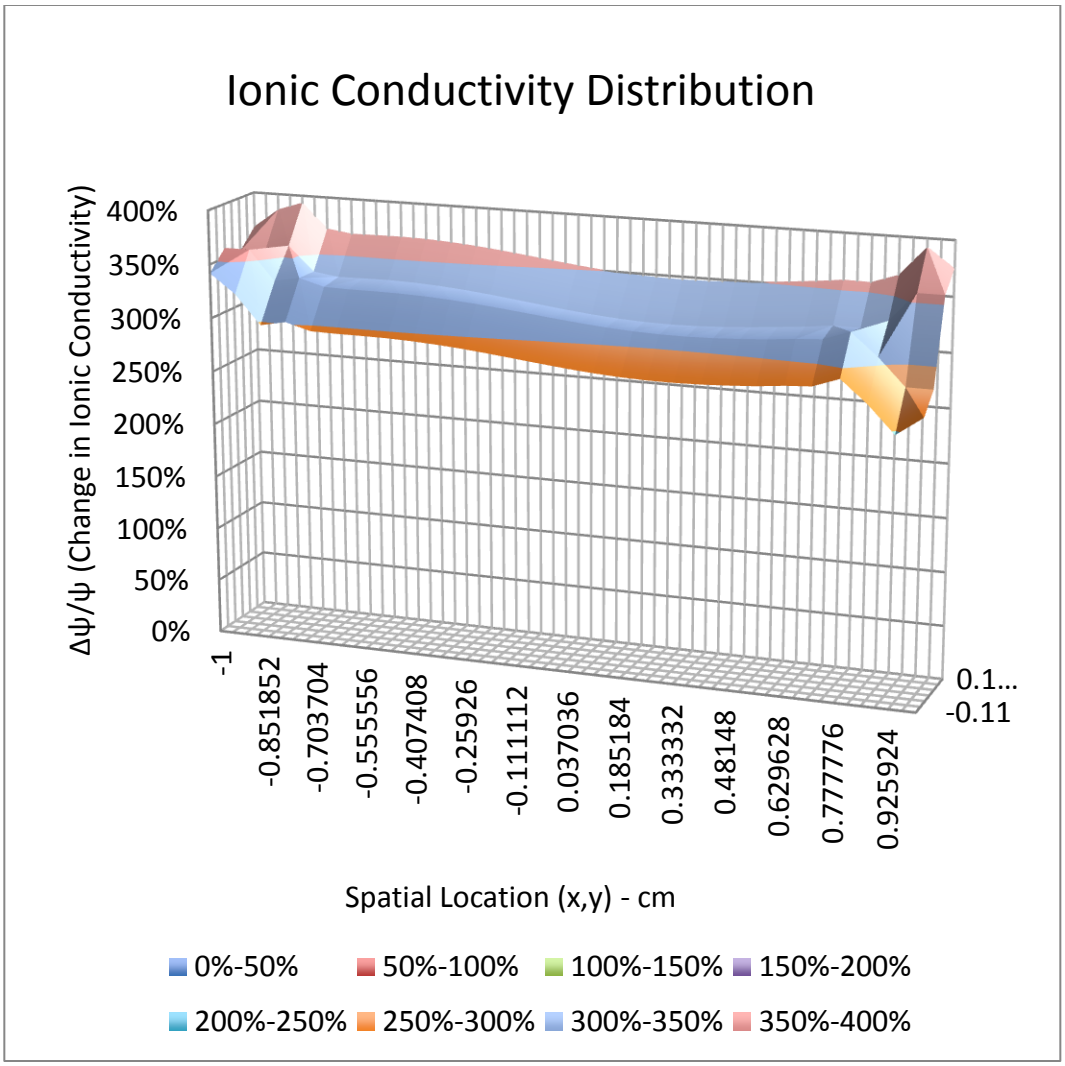

Figure 54: Surface plot illustrating percent change in ionic conductivity spatial with applied bending stress field (nonlinear geometry considered, bending curvature radius of 2 mm) [259].

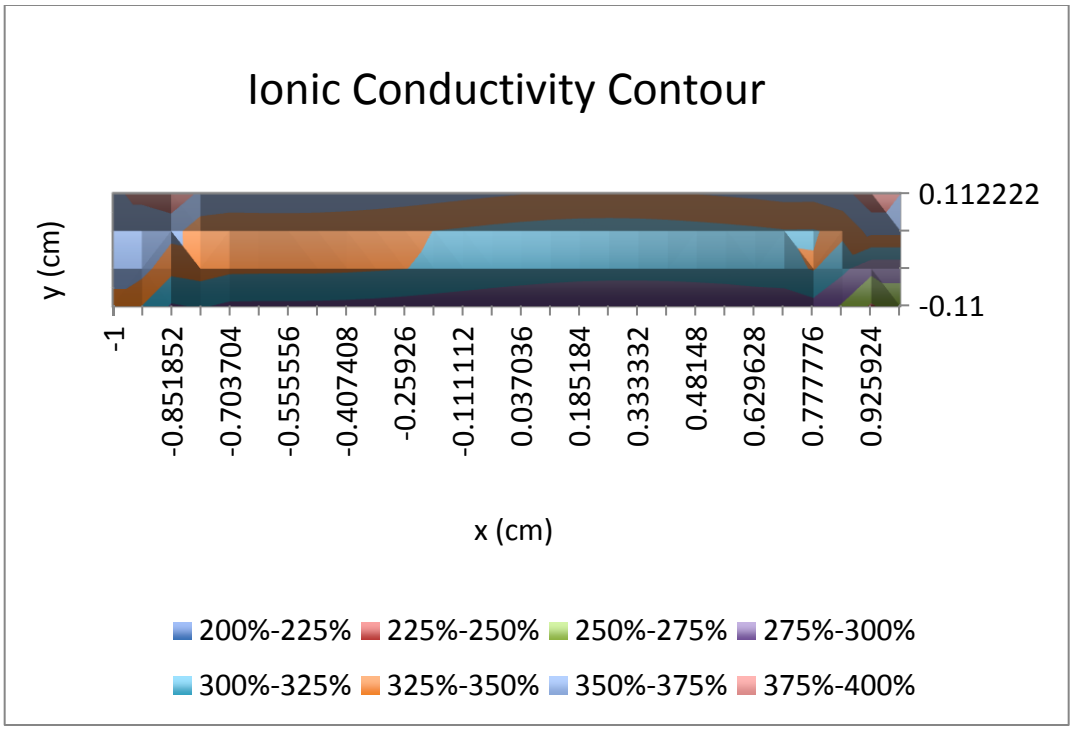

Figure 55: Contour plot illustrating percent change in ionic conductivity spatial with applied bending stress field (large deformation assumption, bending curvature radius of 2 mm) [259].

For simplicity the diffusion coefficients are assumed to be constant and isotropic, and an average value is assumed across the electrolyte material (PEO). In reality, depending on the degree of crystallinity and the quality of the electrolyte sample, the diffusion coefficients may vary spatially throughout the electrolyte, e.g., higher diffusion coefficients in amorphous regions than in crystallite regions. Additionally, swelling of regions within the electrolyte can affect the stiffness, and the bulk and elastic modulus, in addition to the mobility which can increase or decrease. This could affect the ionic conductivity throughout the sample, introducing additional nonlinearity into the solution. Further experimental work would be needed to determine these coefficients.

An important observation about the solution is that the effect of nonlinear geometry can be seen as the bending radius decreases. For larger bending radius (10 mm), the ionic conductivity distribution is comparable for small and large deformation results. However, as bending radius changes to 2 mm, the difference in the solution diverges more substantially. This indicates that nonlinear geometry must be considered for large deformations and high bending curvature. Furthermore, it is seen that an increase in applied strain results in a substantial increase in the ionic conductivity, as observed experimentally [12]. There is a slight variation at the boundaries, where ionic conductivity increases sharply, which can be attributed to mechanical boundary constraint where strain gradients are larger. Furthermore, the ionic conductivity is observed to be higher on the tension side of bending than on the compressive side. This is somewhat intuitive since species diffusion progresses more easily in tensile regions, which is confirmed by how the hydrostatic stress state influences the chemical potential [255]. However, the deformation mechanisms occurring on the compressive side of bending would require further evaluation to determine the manner of influence on ion conduction, since experimental data suggests improved ion conduction in a compressive stress field [12].

It is important to note that further refinement of the mesh, and smaller step iterations for simultaneously solving the coupled differential equations numerically can increase the accuracy of the numerical solution. For the results presented, in the small bending radius case, for some applications the solution may be reasonably accurate. However, further increment and mesh refinement may be needed to

improve the accuracy in the large deformation case. Many commercially available software packages and solver codes lack the capability of obtaining a solution for the coupled equations in the form presented in this dissertation, and therefore additional simplifications of the equations is needed for the large deformation case.

6. Conclusions

The results of numerically solving the analytical models confirm that an increase in ionic conductivity is expected with applied deformation of the battery, which was observed experimentally [12]. The boundary conditions were defined according to the application considered, whether modeling the experiment or whether as a component in the flexible or stretchable LIB. The effects of nonlinear geometry under large deformation must be considered for large loads or large displacement problems, particularly in the case of bending loads, since it is shown that the linear small deformation assumption begins to diverge from the large deformation results for low bending radius. The accuracy of the solution may also be improved by further refinement of the mesh, and use of smaller increments between solution steps in simultaneously solving for the concentration term and strain field variable terms.

Chapter VII Conclusions and Future Work

1. Conclusions

The work presented in this dissertation investigated the relationship between multiple design related parameters, material properties and behavior, and the influence of application loads and deformation on battery performance using computational and analytical modeling to assess the performance of flexible and stretchable LIB materials. While the materials used were the same in the stretchable and flexible battery designs that were examined, the target applications and expected loads were very different. This led to consideration of different types of application loads and geometries in the model development.

Initially multiple battery designs, specifically a flexible and a stretchable LIB, were evaluated using a combination of experimental testing and numerical-based simulation. The focus of this work was on analyzing the mechanical response of each battery using the finite element method, to model bending and stretch experiments for each type of battery. The primary loading considered for the flexible battery is bending, and for stretchable battery it is tensile extension loading. Detailed stress analysis was completed to simulate the respective battery experiments, and from this analysis strain, displacement profiles, local forces, and stress were obtained and studied, as shown in Chapter II and Chapter IV. This initial work provided an understanding and a basis for the development of the analytical models that were presented throughout this dissertation.

1.1 Development of analytical models

By considering natural laws such as Newton's laws of motion (2nd Law), thermodynamic laws, and mass balances, the models that were presented in this dissertation were developed. These natural laws formed the basis of the processes used to arrive at the final modeling equations. For the flexible battery, the observations from Chapter II led to the proposed analytical models that were presented in Chapter III. Initially through experiment, it was observed that when bending loads were applied to the flexible battery, it was accompanied by a slight decrease in battery impedance, which is directly related to battery performance. Based on some of the initial modeling efforts to simulate the battery experiment, which showed an increase in contact pressure between the electrodes and the electrolyte layers, it was hypothesized that the change in impedance was due to the increased contact pressure. This is because contact conductance is inversely proportional to contact impedance, and contact conductance was thought to be improved by increased contact pressure between the electrode and electrolyte interfaces. By considering kinetic laws of motion, and assuming that the flexible battery could be modeled similarly to that of a composite multilayer beam, the mechanical response of the flexible battery could be obtained as a function of contact pressure and input bending loads. Further investigation yielded insight into how layer interfacial properties, and manner of bending, affect the contact pressure between the layers. Linear and nonlinear models were obtained, and it was found that the linear models have a limited range of application (large bending radii).

Averaging of the contact pressure between the layers and plotting this average contact pressure as a function of curvature showed that the increase in contact pressure with curvature within the flexible battery follows an exponentially increasing trend. Experimental bend testing of the flexible battery, with measurement of the impedance, yielded a change in conductance that followed a similar exponential trend, with the conductance being the inverse of impedance. This confirmed the original hypothesis that the observed decrease in impedance in the flexible battery under an applied bending load, during operation, could be at least partially attributed to the change in contact pressure between the layers of the battery.

Aside from method of bending, two important features that warrant further discussion are the electrode/electrolyte interfacial properties, and the selection of electrolyte material. Both of the design parameters can have a substantial impact on the battery mechanical response, and also present performance limitations. In Chapter II the contact pressure and mechanical response of a PEO electrolyte and a PEO with 1% GO electrolyte were compared, and it was found that the PEO with 1% GO electrolyte resulted in a larger contact pressure with bending curvature than the PEO electrolyte. This is because there is a difference in stiffness between these electrolytes, specifically that the stiffness of the PEO with 1% GO is higher than the PEO electrolyte. This means that a higher bending load is required to bend the flexible battery to a particular bending radius, and the load transmittal due to higher bending load increases the contact pressure. This, in turn, is hypothesized to cause a larger reduction in contact impedance as a result. Additionally this can be tied to the

interfacial properties between the electrode/electrolyte layers in the flexible battery. A considerable difference in contact pressure is observed between the strongly bonded and unbounded interface conditions. In reality, it is possible that a weakly bonded or imperfectly bonded condition will be present between the electrode layers. For dissimilar layer materials under loading, it is expected that shear stress will develop between the layers due to differing material properties, e.g., Poisson ratio and elastic modulus, in adjacent layers. If the shear stress is sufficiently high as to break the bonding between the layers, there will be a transition between a bonded and an unbounded interfacial condition. This suggests that there is a limit on the shear stress that can develop between adjacent layers, which is tied directly to the input bending moment. This can be verified by further development of the tangential equations of motion, and would suggest that a sharp performance change is expected if a critical bending curvature is attained. Therefore there is expected to be a material limit in which a user may wish to avoid in order to optimize the performance of the flexible battery. Consequently, electrolyte material type, layer adhesion, and encapsulation methods will all influence the interfacial properties that may drive this limit.

A model for the mechanical response within the spiral geometry battery was proposed in order to relate input tensile/extension loading to the deflection observed in this stretchable battery. Application of Castagliano's theorem allowed for the development of equations that show the relationship between input force, local torsion, instantaneous spiral radius, and deflection. Partial differentiation of the energy and force equations allow for direct verification of the deflection change

with respect to instantaneous radius. Furthermore, it can be demonstrated in this model that the torsional forces change linearly moving along the spiral arm, i.e., with increasing radius the stress variation stays approximately constant with increasing radius. The most prominent stress variation expected is with respect to the shear stress distribution through a cross-section at any radius, r. This was observed in the simulation, and is expected in application. Consequently the change in contact pressure along the spiral with increasing instantaneous radius can be predicted. This parametric relationship of this spiral battery can be used to optimize the design, which includes materials selection.

With an understanding of the mechanical aspects of the flexible and stretchable battery performance, a deeper investigation into the electrochemical performance of the battery and how it is related to the material response of the batteries was completed. The focus in this work was the electrolyte, directly impacting battery ionic conduction, which has a substantial impact on battery performance. Reference to experimental work that relates ionic conductivity to an applied strain starts the theoretical discussion. It was observed experimentally that the ionic conductivity increases with an applied strain in the PEO electrolyte. This was hypothesized to be related to the deformation processes that the electrolyte undergoes in an applied strain field. Due to the changes in the electrolyte during increasing controlled strain, specifically chain motion and extension, the ions were hypothesized to more freely move in the direction of applied strain due to enhanced mobility. In order to model this using analytical methods, a key relation was used to relate ionic conductivity to ionic concentration within the battery.

Using continuum-based methods and thermodynamic laws, a model was obtained to relate mass concentration to strain, and subsequently ionic conductivity to strain. The model includes terms that suggest a spatial dependence, and a direct dependence on the mobility within the host matrix, or electrolyte. By making simplifying assumptions and defining boundary conditions that correspond to the ionic conductivity experiment, and the flexible battery intercalation process, the analytical models were solved and an expression obtained for ionic conductivity as a function of applied strain, which followed an exponentially increasing function. This is validated with the experimental data, and both plots suggest an increase in ionic conductivity with applied strain.

The analytical models were applied to the battery assembly by assuming concentration flux boundary conditions on the electrolyte surfaces at the electrode interfaces. The solution showed that the ionic conductivity can vary spatially within the electrolyte due to a gradient strain field, in this case due to bending. This assumes isotropic or averaged material properties across the sample. Given the dependence of ionic conductivity on the mobility tensor, it is hypothesized that a more detailed analysis would reveal a spatial dependence with respect to mobility locally throughout the sample, since in a semi-crystalline polymer, increased mobility is expected in the amorphous grains due to increased free volume in those regions over the crystalline grains. That is, the mass diffusion of the ions is expected to progress more easily locally in these amorphous regions. In addition to the local mobility, the local strain field is expected to influence ion concentration and ionic conductivity spatially via non-Fickian diffusion. These are important findings since

this shows that ionic conductivity can be anticipated based on degree of crystallinity of the electrolyte polymer material, and characteristics within the host polymer, including tortuosity and free volume, and the applied strain.

1.2 Limitations of linear methods and use of nonlinear models

The analytical models that were developed considered both linear and nonlinear approaches. If rigid materials under small deformation were to be considered, the linear solutions would provide a suitable approximation of battery performance. This would be useful for batteries composed of more rigid, crystalline materials, and if they were subjected to small bending curvature or small stretch. Since the aim of the flexible and stretchable batteries is to develop batteries that are capable of large deformations, nonlinear methods may be required to more accurately predict mechanical and electrochemical response.

In the case of the flexible battery, where the deflection profile of the design was considered under an applied bending load, the assumption that makes valid the small displacement solution is if the bending curvature results in a deflection angle such that $\tan(\theta) \approx 0$. The equation developed in this dissertation is novel because it transforms the common beam deflection equation to put it into terms of the deflection angle, and in doing so considers the inherent nonlinearity in the solution. This is applied to the flexible battery problem by making an analogy to a composite beam subjected to bending loads, which makes it possible to derive an expression that relates the battery loading to deflection state, and the individual force balance at each layer.

For the coupled electrochemical-mechanical model that relates ion concentration and ionic conductivity to strain, neglecting the large deformation solution and nonlinear geometry is thought to be permissible for small applied strains of only a few percent. Since the models developed consider only elastic deformation, and since the PEO material under consideration exhibits only a small elastic range in tensile deformation, a linear solution may yield a reasonably accurate approximation of battery performance. In consideration of the flexible LIB bending problem, it is shown that for large bending radius the small deformation solution is accurate, but for small bending radius/large bending curvature, nonlinearity must be considered.

While similar previous approaches may have yielded useful relationships between strain and mass diffusion, they lack a certain interchangeability that the model in the present work possesses. This model accounts for Fickian and non-Fickian diffusional processes, and relates these to chemical potential. Since this is the case, and since chemical potential is related to a definable internal energy expression, it is possible to more easily include additional energy terms to account for viscoelasticity, plasticity, and the influence of an electric field, in the calculation of ionic conductivity. The advantage is that while the approach derived in this dissertation is fundamental, it is more generalized, and definable boundary conditions make it well suited for solving the coupled electrochemical-mechanical relation inherent in the flexible and stretchable battery problem.

2. Future Work

2.1 Analytical model relationship to battery capacity

The models proposed in this work are useful for predicting certain characteristics of the battery performance under applied loading. While it is useful to understand these particular relationships, including ionic conductivity change with applied strain, and change in battery impedance with applied loading, of considerable research interest is how these relate to and influence the battery capacity. During bending experiments of the flexible LIB, while impedance was seen to decrease, capacity was also observed to decrease. Since the electrodes control the capacity of the battery, this would require additional work on the electrode material response, which could be tied in with the work that produces the coupled electrochemical-mechanical equations governing the electrolyte material behavior. However, more extensive study of the behavior of the deformation mechanisms of the anode and cathode materials would be needed to understand assumptions that can be made to modify or augment the current equations from this dissertation.

2.2 Electrolyte viscoelastic and inelastic deformation

The semi-crystalline polymer may present a challenge because it has a limited range in which its material response will be elastic. In a flexible battery, if the desire is for the battery to remain in this elastic region during operation, there may be a limited bending curvature in which to remain elastic, with higher degree of crystallinity PEO yielding a smaller elastic range. Additionally, loading of the battery

may not always be at a rapid strain-rate so as to minimize the influence of viscoelasticity. Plasticity and viscoelasticity may introduce additional complications in calculating the contact pressure between layers due to residual stress development and time dependent effects. This also holds for calculating the ionic conductivity within a PEO electrolyte in a battery assembly.

The equations that have been proposed in this work would require augmentation with additional terms to account for the influence of viscoelasticity and plasticity. For example, the potential energy expression would have to include a viscoelastic expression, and a transient analysis would need to be completed. An expression that can accurately account for the inelastic deformation of the PEO in the different deformation regions beyond the yield point would have to be developed and included in the energy expression.

2.3 Detailed modeling of non-Fickian diffusion and experimental constants

Inherent in the battery application is the potential for observing non-Fickian diffusional effects. Additionally, the material constants used in these models are assumed, and experiment, MD or quantum mechanics materials models that can be used to predict these constants, would be needed to more comprehensively calculate the change in ionic conductivity with strain. Local swelling of the PEO electrolyte due to diffusion of the Li ions locally within the host polymer matrix may have a local impact or may affect ionic conductivity. Determination of the parameters used in these numerical models, e.g., diffusion coefficients, elastic modulus, mobility, etc., and how these terms vary with increasing local

concentration and applied strain, would enhance the calculation of ionic conductivity within the electrolyte.

References

[1] Li, L., Wu, Z., Yuan, S., and Zhang, X., 2014, "Advances and Challenges for Flexible Energy Storage and Conversion Devices and Systems," *Energy & Environmental Science*, 7(7), pp. 2101-2122.

[2] Armand, M., and Tarascon, J. M., 2008, "Building Better Batteries," *Nature*, 451, pp. 652-657.

[3] Tarascon, J. M., and Armand, M., 2001, "Issues and Challenges Facing Rechargeable Lithium Batteries," *Nature*, 414, pp. 359-367.

[4] Gwon, H., Hong, J., Kim, H., Seo, D. H., Jeon, S., and Kang, K., 2014, "Recent Progress on Flexible Lithium Rechargeable Batteries," *Energy and Environmental Science*, 7(2), pp. 538-551.

[5] Sun, B., Long, Y. Z., Chen, Z. J., Liu, S. L., Zhang, H. D., Zhang, J. C., and Han, W. P., 2014, "Recent Advances in Flexible and Stretchable Electronic Devices via Electrospinning," *Journal of Materials Chemistry C*, 2(7), pp. 1209-1219.

[6] Yan, C. and Lee, P. S., 2014, "Stretchable Energy Storage and Conversion Devices," *Small*, 10(17), pp. 3443-3460.

[7] Whittingham, M. S., 2008, "Materials Challenges Facing Electrical Energy Storage," *Mrs Bulletin*, 33(4), pp. 411-419.

[8] Scrosati, B., and Garche, J., 2010, "Lithium Batteries: Status, Prospects and Future," *Journal of Power Sources*, 195(9), pp. 2419-2430.

[9] Zhou, G., Li, F., and Cheng, H.M., 2014, "Progress in Flexible Lithium Batteries and Future Prospects," *Energy and Environmental Science*, 7(4), pp. 1307-1338.

[10] Zhang, Y., Bai, W., Ren, J., Weng, W., Lin, H., Zhang, Z., and Peng, H., 2014, "Super-Stretchy Lithium-Ion Battery Based on Carbon Nanotube Fiber," *Journal of Materials Chemistry A*, 2(29), pp. 11054-11059.

[11] Kammoun, M., Berg, S., and Ardebili, H., 2015, "Flexible Thin-Film Battery Based on Graphene-Oxide Embedded in Solid Polymer Electrolyte," *Nanoscale*, 7(41), pp. 17516-17522.

[12] Kelly, T., Ghadi, B. M., Berg, S., and Ardebili, H., 2016, "In Situ Study of Strain-Dependent Ion Conductivity of Stretchable Polyethylene Oxide Electrolyte," *Scientific Reports*, 6(20128), pp. 1-9.

[13] Sims, R., Rogner, H. H., and Gregory, K., 2003, "Carbon Emission and Mitigation Cost Comparisons Between Fossil Fuel, Nuclear and Renewable Energy Resources for Electricity Generation," *Energy Policy*, 31(13), pp. 1315-1326.

[14] Hook, M., and Tang, X., 2013, "Depletion of Fossil Fuels and Anthropogenic Climate Change - A Review," *Energy Policy*, 52, pp. 797-809.

[15] Haines, A., Kovats, R. S., Campbell-Lendrum, D., and Corvalan, C., 2006, "Climate Change and Human Health: Impacts, Vulnerability and Public Health," *Public Health*, 120(7), pp. 585-596.

[16] Hadjipaschalis, I., Poullikkas, A., and Efthimiou, V., 2009, "Overview of Current and Future Energy Storage Technologies for Electric Power Applications," *Renewable & Sustainable Energy Reviews*, 13(6-7), pp. 1513-1522.

[17] Ibrahim, H., Ilinca, A., and Perron, J., 2008, "Energy Storage Systems – Characteristics and Comparisons," *Renewable & Sustainable Energy Reviews*, 12(5), pp. 1221-1250.

[18] Carrette, L., Friedrich, K. A., and Stimming, U., 2001, "Fuel Cells – Fundamentals and Applications," *Fuel Cells*, 1(1), pp. 5-39.

[19] Dell, R. M., 2000, "Batteries – Fifty Years of Materials Development," *Solid State Ionics*, 134(1-2), pp. 139-158.

[20] Takamura, T., 2002, "Trends in Advanced Batteries and Key Materials in the New Century," *Solid State Ionics*, 152, pp. 19-34.

[21] Chen, H., Cong, T. N., Yang, W., Tan, C., Li, Y., and Ding, Y., 2009, "Progress in Electrical Energy Storage Systems: A Critical Review," *Progress in Natural Science*, 19(3), pp. 291-312.

[22] Jayalakshmi, M., and Balasubramanian, K., 2008, "Simple Capacitors to Supercapacitors – An Overview," *International Journal of Electrochemical Science*, 3(11), pp. 1196-1217.

[23] Zhang, L. L., Zhou, R., and Zhao, X. S., 2010, "Graphene-Based Materials as Supercapacitor Electrodes," *Journal of Materials Chemistry*, 20(29), pp. 5983-5992.

[24] Ekanayake, S. R., Cortie, M. B., and Ford, M. J., 2004, "Design of Nanocapacitors and Associated Materials Challenges," *Current Applied Physics*, 4(2-4), pp. 250-254.

[25] Cohen, R., 2009, "Nanocapacitors: Undead Layers Breathe New Life," *Nature Materials*, 8(5), pp. 366-368.

[26] Haspert, L. C., Lee, S. B., and Rubloff, G. W., 2012, "Nanoengineering Strategies for Metal-Insulator-Metal Electrostatic Nanocapacitors," *ACS Nano*, 6(4), pp. 3528-3536.

[27] Nishide, H., and Oyaizu, K., 2008, "Materials Science - Toward Flexible

Batteries," *Science*, 319(5864), pp. 737-738.

[28] Koo, M., Park, K., Lee, S. H., Suh, M., Jeon, D. Y., Choi, J. W., Kang, K., and Lee, K. J., 2012, "Bendable Inorganic Thin-Film Battery for Fully Flexible Electronic Systems," *Nano Letters*, 12(9), pp. 4810-4816.

[29] Wu, M.-S, Lee, J.-T., Chiang, P.-C. J., and Lin, J.-C, 2007, "Carbon-Nanofiber Composite Electrodes for Thin and Flexible Lithium-Ion Batteries," *Journal of Materials Science*, 42(1), pp. 259-265.

[30] Goyal, A., Reddy, A. L. M., and Ajayan, P. M., 2011, "Flexible Carbon Nanotube/Cu20 Hybrid Electrodes for Li-Ion Batteries," *Small*, 7(12), pp. 1709-1713.

[31] Chew, S. Y., Ng, S. H., Wang, J., Novak, P., Krumeich, F, Chou, S. L., Chen, J., and Liu, H. K., 2009, "Flexible Free-Standing Carbon Nanotube Films for Model Lithium Ion Batteries," *Carbon*, 47(13), pp. 2976-2983.

[32] Wang, J. Z, Zhong, C., Chou, S. L, and Liu, H. K, 2010, "Flexible Free-Standing Graphene-Silicon Composite Film for Lithium-Ion Batteries," *Electrochemistry Communications*, 12(11), pp. 1467-1470.

[33] Li, N., Chen, Z., Ren, W., Li, F., and Cheng, H. M., 2012, "Flexible Graphene-Based Lithium Ion Batteries with Ultrafast Charge and Discharge Rates," *Proceedings of the National Academy of Sciences of the United States of America*, 109(43), pp. 17360-17365.

[34] Noerochim, L., Wang, J.-Z, Chou, S.-L, Wexler, D, and Liu, H.-K, 2012, "Freestanding Single-Walled Carbon Nanotube/Sn02 Anode Paper for Flexible Lithium-Ion Batteries," *Carbon*, 50(3), pp. 1289-1297.

[35] Lee, S.-Y., Choi, K.-H, Choi, W.-S, Kwon, Y. H, Jung, H.-R, Shin, H.-C, and Kim, J. Y., 2013, "Progress in Flexible Energy Storage and Conversion Systems, with a Focus on Cable-Type Lithium-Ion Batteries," *Energy & Environmental Science*, 6(8), pp. 2414-2423.

[36] Park, M.H., Noh, M., Lee, S. Minseong, K., Chae, S., Sim, S., Choi, S., Kim, H., Nam, H., Park, S., and Cho, J., 2014, "Flexible High-Energy Li-Ion Batteries with Fast-Charging Capability," *Nano Letters*, 14(7), pp. 4083-4089.

[37] Hu, L., Wu, H., La Mantia, F., Yang, Y., and Cui, Y., 2010, "Thin, Flexible Secondary Li-Ion Paper Batteries," *ACS Nano*, 4(10), pp. 5843–5848.

[38] Li, S., Luo, Y., Lv, W., Yu, W., Wu, S., Hou, P., Yang, Q., Meng, Q., Liu, C., and Cheng, H. M., 2011, "Vertically Aligned Carbon Nanotubes Grown on Graphene Paper as Electrodes in Lithium-Ion Batteries and Dye-Sensitized Solar Cells," *Advanced Energy Materials*, 1(4), pp. 486-490.

[39] Xie, K., and Wei, B., 2014, "Materials and Structures for Stretchable Energy Storage and Conversion Devices," *Advanced Materials*, 26(22), pp. 3592-3617.

[40] Kettlgruber, G., Kaltenbrunner, M., Siket, C. M., Moser, R., Graz, I. M., Schwödiauer, R., and Bauer, S., 2013, "Intrinsically Stretchable and Rechargeable Batteries for Self-Powered Stretchable Electronics," *Journal of Materials Chemistry A*, 1(18), pp. 5505-5508.

[41] Song, Z., Ma, T., Tang, R., Cheng, Q., Wang, X., Krishnaraju, D., Panat, R., Chan, C. K., Yu, H., and Jiang, H., 2014, "Origami Lithium-Ion Batteries," *Nature Communications*, 5, pp. 3140.

[42] Gaikwad, A. M., Zamarayeva, A. M., Rousseau, J., Chu, H., Derin, I., Steingart, D., 2012, "Highly Stretchable Alkaline Batteries Based on an Embedded Conductive Fabric," *Advanced Materials*, 24(37), p. 5071-5076.

[43] Kwon, Y. H., Woo, S. W., Jung, H. R., Yu, H. K., Kim, K., Oh, B. H., Ahn, S., Lee, S. Y., Song, S. W., Cho, J., Shin, H. C., and Kim, J. Y., 2012, "Cable-Type Flexible Lithium Ion Battery Based on Hollow Multi-Helix Electrodes," *Advanced Materials*, 24(38), pp. 5192–5197.

[44] Yang, Y., Jeong, S., Hu, L., Wu, H., Lee, S. W., and Cui, Y., 2011, "Transparent Lithium-Ion Batteries," *Proceedings of the National Academy of Sciences of the United States of America*, 108(32), p. 13013-13018.

[45] Xu, S., Zhang, Y., Cho, J., Lee, J., Huang, X., Jia, L., Fan, J. A., Su, Y., Su, J., Zhang, H., Cheng, H., Lu, B., Yu, C., Chuang, C., Kim, T., Song, T., Shigeta, K., Kang, S., Dagdeviren, C., Petrov, I., Braun, P. V., Huang, Y., Paik, U., and Rogers, J. A., 2013, "Stretchable Batteries with Self-Similar Serpentine Interconnects and Integrated Wireless Recharging Systems," *Nature Communications*, 4, p. 1543.

[46] Wang, C., Zheng, W. Yue, Z., Too., C. O., and Wallace, G. G., 2011, "Buckled, Stretchable Polypyrrole Electrodes for Battery Applications," *Advanced Materials*, 23(31): pp. 3580-3584.

[47] Filiatrault, H. L., Porteous, G. C., Carmichael, R. S., Davidson, G. J. E., and Carmichael, T. B., 2012, "Stretchable Light-Emitting Electrochemical Cells Using an Elastomeric Emissive Material," *Advanced Materials*, 24(20), pp. 2673-2678.

[48] Han, S., Hwang, K. S., Yoo, Y. K., Lee, S. M., and Lee, J. H., 2014, "Flexible and Stretchable Energy Harvesting Device Using Three-Dimensional Poly (Dimethylsiloxane)," *Japanese Journal of Applied Physics*, 53(8S3), pp. 08NC01.

[49] Shin, U. H., Jeong, D. W., Kim, S. H., Lee, H. W., and Kim, J. M., 2014, "Elastomer-Infiltrated Vertically Aligned Carbon Nanotube Film-Based Wavy-Configured Stretchable Conductors," *ACS Applied Materials and Interfaces*, 6(15), pp. 12909-12914.

[50] Liu, Y., Gorgutsa, S., Santato, C., and Skorobogatiy, M., 2012, "Flexible, Solid Electrolyte-Based Lithium Battery Composed of LiFePO4 Cathode and Li4Ti5O12 Anode for Applications in Smart Textiles," *Journal of the Electrochemical Society*, 159(4), pp. A349-A356.

[51] Kil, E. H., Choi, K. H., Ha, H. J., Xu, S., Rogers, J. A., Kim, M. R., Lee, Y. G., Kim, K. M., Cho., K. Y., and Lee, S. Y., 2013, "Imprintable, Bendable, and Shape-Conformable Polymer Electrolytes for Versatile-Shaped Lithium-Ion Batteries," *Advanced Materials*, 25(10), pp. 1395-1400.

[52] Ulaganathan, M., Nithya, R., Rajendran, S., and Raghu, S., 2012, "Li-Ion Conduction on Nanofiller Incorporated PVdF-co-HFP Based Composite Polymer Blend Electrolytes for Flexible Battery Applications," *Solid State Ionics*, 218, pp. 7-12.

[53] Dias, F. B., Plomp, L., and Veldhuis, J. B. J., 2000, "Trends in Polymer Electrolytes for Secondary Lithium Batteries", *Journal of Power Sources*, 88(2), 169-191.

[54] Agrawal, R. C., and Pandey, G. P., 2008, "Solid Polymer Electrolytes: Materials, Designing and All-Solid-State Battery Applications: an Overview," *Journal of Physics D: Applied Physics*, 41(22), pp. 1-18.

[55] Croce, F., Appetecchi, G. B., Persi, L., and Scrosati, B., 1998, "Nanocomposite Polymer Electrolytes for Lithium Batteries," *Nature*, 394, pp. 456-458.

[56] Murata, K., 1995, "An Overview of the Research and Development of Solid Polymer Electrolyte Batteries," *Electrochimica Acta*, 40(13-14), pp. 2177-2184.

[57] Murata, K., Izuchi, S., and Yoshihisa, Y., 2000, "An Overview of the Research and Development of Solid Polymer Electrolyte Batteries," *Electrochemica Acta*, 45(8-9), pp. 1501-1508.

[58] Nguyen, C., Xiong, S., Ma, J., Lu, X., and Lee, P. S., 2011, "High Ionic Conductivity P(VDF-TrFE)/PEO Blended Polymer Electrolytes for Solid Electrochromic Devices," *Physical Chemistry Chemical Physics*, 13, pp. 13319-13326.

[59] Scrosati, B., Croce, F., and Persi, L., 2000, "Impedance Spectroscopy Study of PEO-Based Nanocomposite Polymer Electrolytes," *Journal of the Electrochemical Society*, 147(5), pp. 1718-1721.

[60] Yang, L. Y., Wei, D., Xu, M., Yao, Y., and Chen, Q., 2014, "Transferring Lithium Ions in Nanochannels: A PEO/Li+ Solid Polymer Electrolyte Design," *Angewandte Chemie*, 126(14), pp. 3705-3709.

[61] Michael, M. S., Jacob, M. M. E., Prabaharan, S. R. S., and Radhakrishna, S., 1997, "Enhanced Lithium Ion Transport in PEO-Based Solid Polymer Electrolytes Employing a Novel Class of Plasticizers," *Solid State Ionics*, 98(3-4), pp. 167-174.

[62] Karan, N., Pradhan, D. K., Thomas, R., Natesan, B., and Katiyar, R. S., 2008, "Solid Polymer Electrolytes Based on Polyethylene Oxide and Lithium Trifluoro-Methane Sulfonate (PEO–$LiCF_3SO_3$): Ionic Conductivity and Dielectric Relaxation," *Solid State Ionics*, 179(19-20), pp. 689-696.

[63] Fullerton-Shirey, S. K., and Maranas, J. K., 2009, "Effect of LiClO4 on the Structure and Mobility of PEO-Based Solid Polymer Electrolytes," *Macromolecules*, 42, p. 2142.

[64] Quartarone, E., and Mustarelli, P., 2011, "Electrolytes for Solid-State Lithium Rechargeable Batteries: Recent Advances and Perspectives," *Chemical Society Reviews*, 40(5), pp. 2525-2540.

[65] Zhang, Y., Bau, W., Cheng, X., Ren, J., Weng, W., Chen, P., Fang, X., Zhang, Z., and Peng, H., 2011, "Flexible and Stretchable Lithium-Ion Batteries and Supercapacitors Based on Electrically Conducting Carbon Nanotube Fiber Springs," *Angewandte Chemie*, 126(52), pp. 14792-14796.

[66] Lee, K. Y., Gupta, M. K., and Kim, S. W., 2015, "Transparent Flexible Stretchable Piezoelectric and Triboelectric Nanogenerators for Powering Portable Electronics," *Nano Energy*, 14, pp. 139-169.

[67] Ren, J., Zhang, Y., Bai, W., Chen, X., Zhang, Z., Fang, X., Weng. W., Wang, Y., and Peng. H., 2014, "Elastic and Wearable Wire-Shaped Lithium-Ion Battery with High Electrochemical Performance," *Angewandte Chemie*, 126(30), pp. 7998-8003.

[68] Armand, M. B., Bruce, P. G., Forsyth, M., Scrosati, B. and Wieczorek, W., 2011, "Polymer Electrolytes," *Energy Materials*, pp. 1-31.

[69] Ji, J., Li, B., and Zhong, W.H., 2010, "Simultaneously Enhancing Ionic Conductivity and Mechanical Properties of Solid Polymer Electrolytes via Copolymer Multi-Funtional Filler," *Electrochimica Acta*, 55(28), pp. 9075-9082.

[70] Rolland, J., Brassinne, J., Bourgeois, J.P., Poggi, E., Vlad, A., and Gohy, J.F., 2014, "Chemically Anchored Liquid-PEO Based Block Copolymer Electrolytes for Solid-State Lithium-Ion Batteries," *Journal of Materials Chemistry A*, 2, pp. 11839-11846.

[71] Oudenhoven, J. F. M., Baggetto, L., and Notten, P. H. L., 2011, "All-Solid-State Lithium-Ion Microbatteries: A Review of Various Three-Dimensional Concepts," *Advanced Energy Materials*, 1(1), pp. 10-33.

[72] Carta, R., Jourand, P. Hermans, B., Thoné, J., Brosteaux, D., Vervust, T., Bossuyt, F., Axisa, F., Vanfleteren, J., Puers, R., "Design and Implementation of Advanced Systems in a Flexible-Stretchable Technology for Biomedical Applications," *Sensors and Actuators A: Physical*, 156(1), pp. 79-87.

[73] Wang, K., Luo, S., Wu, Y., He., X, Zhao, F., Wang, J., Jiang, K., and Fan, S., 2013, "Super-Aligned Carbon Nanotube Films as Current Collectors for Lightweight and Flexible Lithium Ion Batteries," *Advanced Functional Materials*, 23(7), pp. 846-853.

[74] Choi, J. Y., Lee, D. J., Lee, Y. M., Lee, Y. G., Kim., K. M., Park, J. K., and Cho, K. Y., 2013, "Silicon Nanofibrils on a Flexible Current Collector for Bendable Lithium-Ion Battery Anodes," *Advanced Functional Materials*, 23(17), pp. 2108-2114.

[75] Lee, J. K, Smith, K. B, Hayner, C. M, and Kung, H. H., 2010, "Silicon Nanoparticles-Graphene Paper Composites for Li Ion Battery Anodes," *Chemical Communications*, 46(12), pp. 2025-2027.

[76] Natarajan, C., Setoguchi, K., and Nogami, G., 1998, "Preparation of a

Nanocrystalline Titanium Dioxide Negative Electrode for the Rechargeable Lithium Ion Battery," *Electrochimica Acta*, 43(21-22), pp. 3371-3374.

[77] Ellis, B. L., Lee, K. T., and Nazar, L. F., 2010, "Positive Electrode Materials for Li-Ion and Li-Batteries," *Chemistry of Materials*, 22(3), pp. 691-714.

[78] Wang, B, Bates, J. B, Hart, F. X, Sales, B. C, Zuhr, R. A, and Robertson, J. D, 1996, "Characterization of Thin-Film Rechargeable Lithium Batteries with Lithium Cobalt Oxide Cathodes," *Journal of the Electrochemical Society*, 143(10), pp. 3203-3213.

[79] Whittingham, M. S., 2004, "Lithium Batteries and Cathode Materials," *Chemical Reviews*, 104(10), pp. 4271-4301.

[80] Vincent, C. A., 2000, "Lithium Batteries: A 50-Year Perspective, 1959-2009," *Solid State lonics*, 134(1-2), pp. 159-167.

[81] Nishi, Y., 2001, "Lithium Ion Secondary Batteries; Past 10 years and the Future," *Journal of Power Sources*, 100(1-2), pp. 101-106.

[82] Megahed, S, and Scrosati, B, 1994, "Lithium-Ion Rechargeable Batteries," *Journal of Power Sources*, 51(1-2), pp.79-104.

[83] Liu, S., Wang, Z., Yu, C. Wu, H. B., Wang, G., Dong, Q., Qiu, J., Eychmuller, A., and Lou, X. W., 2013, "A Flexible TiO(2)(B)-Based Battery Electrode with Superior Power Rate and Ultralong Cycle Life," *Advanced Materials*, 25(25), pp. 3462-3467.

[84] Morris, R. S., Dixon, B. G., Gennett, T., Rafaelle, R., and Heben, M. J., 2004, "High-Energy, Rechargeable Li-Ion Battery Based on Carbon Nanotube Technology," *Power Sources*, 138, pp. 277-280.

[85] Ng, S. H., Wang, J., Guo, Z. P., Chen, J., Wang, G. X., Liu, H. K., 2005, "Single Wall Carbon Nanotube Paper as Anode for Lithium-Ion Battery," *Electrochimica Acta*, 51(1), pp. 23-28.

[86] Liu, J., Song, K., van Aken, P. A., Maier, J., and Yu, Y., 2014, "Self-Supported Li4Ti5O12–C Nanotube Arrays as High-Rate and Long-Life Anode Materials for Flexible Li-Ion batteries," *Nano Letters*, 14(5), pp. 2597-2603.

[87] Chan, C. K., Peng, H., Liu, G., McIlwrath, K., Zhang, X. F., Huggins, R. A., and Cui, Y., 2008, "High-Performance Lithium Battery Anodes Using Silicon Nanowires," *Nanotechnology*, 3, pp. 31-35.

[88] Wang, D., Kou, R., Choi, D., Yang, Z., Nie, Z., Li, J., Saraf, L. V., Hu, D., Zhang, J., Graff, G., Liu, J., Pope, M. A., and Aksay, I. A., 2010, "Ternary Self-Assembly of Ordered Metal Oxide–Graphene Nanocomposites for Electrochemical Energy Storage," *ACS Nano*, 4(3), pp. 1587-1595.

[89] Chen, J., Liu, Y., Minett, A., Lynam, C., Wang, J., and Wallace, G. G., 2007, "Flexible, Aligned Carbon Nanotube/Conducting Polymer Electrodes for a Lithium-Ion Battery," *Chemistry of Materials*, 19(15), pp. 3595-3597.

[90] Zhou, M., Pu, F., Wang, Z., Cai, T., Chen, H., Zhang, H., and Guan, S., 2013, "Facile Synthesis of Novel Si Nanoparticles–Graphene Composites as High-Performance Anode Materials for Li-Ion Batteries," *Physical Chemistry Chemical Physics*, 15, pp. 11394-11401.

[91] Agubra, V. A., and Fergus, J. W., 2014, "The Formation and Stability of the Solid Electrolyte Interface on the Graphite Anode," *Journal of Power Sources*, 268, pp.153-162.

[92] Scrosati, B., 2000, "Recent Advances in Lithium Ion Battery Materials," *Electrochimica Acta*, 45(15-16), pp. 2461-2466.

[93] Wakihara, M., 2001, "Recent Developments in Lithium Ion Batteries," *Materials Science & Engineering R-Reports*, 33(4), pp. 109-134.

[94] Baker, D. R., Verbrugge, M. W., and Bower, A. F., 2016, "Swelling and Elastic Deformation of Lithium-Silicon Electrode Materials," *Journal of the Electrochemical Society*, 163(5), pp. A624-A631.

[95] Xu, K., 2004, "Nonaqueous Liquid Electrolytes for Lithium-Based Rechargeable Batteries," *Chemical Reviews*, 104(10), pp. 4303-4417.

[96] Beck, F., and Ruetschi, P., 2000, "Rechargeable Batteries with Aqueous Electrolytes," *Electrochimica Acta*, 45(15-16), pp. 2467-2482.

[97] Hayashi, K., Nemoto, Y., Tobishima, S., and Yamaki, J., 1999, "Mixed Solvent Electrolyte for High Voltage Lithium Metal Secondary Cells," *Electrochimica Acta*, 44(14), pp.2337-2344.

[98] Osaka, T., Naoi, K, Sakai, H, and Ogano, S, 1987, "Effect of PF6-Anion on the Properties of Lithium-Polypyrrole Battery During Polypyrrole File Formation," *Journal of the Electrochemical Society*, 134(2), pp. 285-289.

[99] Campion, C. L, Li, W. T., and Lucht, B. L., 2005, "Thermal Decomposition of LiPF6-Based Electrolytes for Lithium-Ion Batteries," *Journal of the Electrochemical Society*, 152(12), pp. A2327-A2334.

[100] Le Bideau, J., Ducros, J.-B., Soudan, P., and Guyomard, D., 2011, "Solid-State Electrode Materials with Ionic-Liquid Properties for Energy Storage: The Lithium Solid State Ionic-Liquid Concept," *Advanced Functional Materials*, 21(21), pp. 4073-

4078.

[101] Song, J. Y, Wang, Y. Y, and Wan, C. C, 1999, "Review of Gel-Type Polymer Electrolytes for Lithium-Ion Batteries," *Journal of Power Sources*, 77(2), pp. 183-197.

[102] Watanabe, M, Kanba, M, Nagaoka, K., and Shinohara, I., 1982, "Ionic Conductivity of Hybrid Films Based on Polyacrylonitrile and Their Battery Application," *Journal of Applied Polymer Science*, 27(11), pp. 4191-4198.

[103] Bohnke, 0, Frand, G, Rezrazi, M, Rousselot, C, and Tmche, C, 1993, "Fast Ion Transport in New Lithium Electrolytes Gelled with PMMA. 1. Influence of Polymer Concentration," *Solid State lonics*, 66(1-2), p. 97104.

[104] Bohnke, 0., Fraud, G., Rezrazi, M., Rousselot, C., and Tmche, C., 1993, "Fast Ion Transport in New Lithium Electrolytes Gelled with PMMA. 2. Influence of Lithium Salt Concentration," *Solid State lonics*, 66(1-2), pp. 105-112.

[105] Song, J. Y., Wang, Y. Y., and Wan, C. C., 2000, "Conductivity Study of Porous Plasticized Polymer Electrolytes Based on Poly(Vinylidene Fluoride) - A Comparison with Polypropylene Separators," *Journal of the Electrochemical Society*, 147(9), pp. 3219-3225.

[106] Pereira, T., Scaffaro, R., Nieh, S., Arias, J., Guo, Z., and Thomas, H., 2006, "The Performance of Thin-Film Li-Ion Batteries under Flexural Deflection," *Journal of Micromechanical Microengineering*, 16(12), p. 2714.

[107] Kamaya, N., Homma, K., Yamakawa, Y., Hirayama, M., Kanno, R., Yonemura, M., Kamiyama, T., Kato, Y., Hama, S., Kawamoto, K., and Mitsui, A., 2011, "A Lithium Superionic Conductor," *Nature Materials*, 10, pp. 682-686.

[108] Kitaura, H., Hayashi, A., Tadanaga, K., and Tatsumisago, M. J., 2009, "High-Rate Performance of All-Solid-State Lithium Secondary Batteries Using $Li_4Ti_5O_{12}$ Electrode," *Power Sources*, 189(1), pp. 145-148.

[109] Nagao, M., Hayashi, A., Tatsumisago, M., Kanetsuku, T., Tsuda, T., and Kuwabata, S., 2013, "In Situ SEM Study of a Lithium Deposition and Dissolution Mechanism in a Bulk-Type Solid-State Cell with a $Li_2S–P_2S_5$ Solid Electrolyte," *Physical Chemistry Chemical Physics*, 15, pp. 18600-18606.

[110] Armand, M. B., 1986, "Polymer Electrolytes," *Annual Review of Materials Science*, pp. 245-261.

[111] Du, J., and Chen, C.-H., 2012, "Structure and Lithium Ion Diffusion in Lithium Silicate Glasses and at their Interfaces with Lithium Lanthanum Titanate Crystals," *Journal of NonCrystalline Solids*, 358(24), pp. 3531-3538.

[112] Bruce, P. G, 1995, "Structure and Electrochemistry of Polymer Electrolytes," Electrochimica Acta, 40(13-14), pp. 2077-2085.

[113] Fergus, J. W., 2010, "Ceramic and Polymeric Solid Electrolytes for Lithium-Ion Batteries," *Journal of Power Sources*, 195(15), pp. 4554-4569.

[114] Schoonman, J., and Kelder, E. M., 1997, "Thin Film Solid Electrolytes and Electrodes for Rechargeable Lithium-Ion Batteries," *Journal of Power Sources*, 68(1), pp. 65-68.

[115] Skaamp, S., West, K., Zachau-Christiansen, B., Popall, M., Kappel, J., Kron, J., Eichinger, G., and Semrau, G., 1998, "Towards Solid State Lithium Batteries Based on ORMOCER Electrolytes," *Electrochimica Acta*, 43(10-1 1), pp.1589-1592.

[116] Dias, F. B, Plomp, L., and Veldhuis, J. B. J., 2000, "Trends in Polymer

Electrolytes for Secondary Lithium Batteries," *Journal of Power Sources*, 88(2), pp. 169-191.

[117] Minami, T., Hayashi, A., and Tatsumisago, M., 2006, "Recent Progress of Glass and Glass-Ceramics as Solid Electrolytes for Lithium Secondary Batteries," *Solid State Ionics*, 177(26-32), pp. 2715-2720.

[118] Maitra, A., and Heuer, A., 2007, "Cation Transport in Polymer Electrolytes: A Microscopic Approach," *Physical Review Letters*, 98(22).

[119] Stolwijk, N. A., and Obeidi, S., 2004, "Radiotracer Diffusion and Ionic Conduction in a PEO-Nai Polymer Electrolyte," *Physical Review Letters*, 93(12).

[120] Wang, Y., Agapov, A. L., Fan, F, Hong, K, Yu, X, Mays, J, and Sokolov, A. P, 2012, "Decoupling of Ionic Transport from Segmental Relaxation in Polymer Electrolytes," *Physical Review Letters*, 108(8).

[121] Papke, B. L, Ratner, M. A, and Shriver, D. F, 1982, "Conformation and Ion‐Transport Models for the Structure and Ionic Conductivity in Complexes of Polyethers with Alkali Metal Salts," *Journal of the Electrochemical Society*, 129(8), pp. 1694-1701.

[122] Qian, X. M, Gu, N. Y., Cheng, Z. L, Yang, X. R., Wang, E. K, and Dong, S. J., 2002, "Plasticizer Effect on the Ionic Conductivity of PEO-Based Polymer Electrolyte," *Materials Chemistry and Physics*, 74(1), pp. 98-103.

[123] Weston, J. E, and Steele, B. C. H, 1982, "Effects of Inert Fillers on the Mechanical and Electrochemical Properties of Lithium Salt-Poly(Ethylene Oxide) Polymer Electrolytes," *Solid State Ionics*, 7(1), pp. 75-79.

[124] Ji, K. S., Moon, H. S., Kim, J. W., and Park, J. W., 2003, "Role of Functional Nano-Sized Inorganic Fillers in Poly(Ethylene) Oxide-Based Polymer Electrolytes," *Journal of Power Sources*, 117(1-2), pp. 124-130.

[125] Jiang, G., Maeda, S., Saito, Y., Tanase, G., and Sakai, T., 2005, "Ceramic-Polymer Electrolytes for All-Solid-State Lithium Rechargeable Batteries," *Journal of the Electrochemical Society*, 152(4), pp. A767-A773.

[126] Ahn, J. H., Wang, G. X., Liub, H. K., and Doub, S.X., 2003, "Nanoparticle-Dispersed PEO Polymer Electrolytes for Li Batteries," *Journal of Power Sources*, 119–121, pp. 422-426.

[127] Prosini, P. P. Passerini, S., Vellone, R., and Smyrl, W. H., 1998, "V_2O_5 Xerogel Lithium–Polymer Electrolyte Batteries," *Journal of Power Sources*, 75(1), pp. 73-78.

[128] Croce, F., and Scrosati, B., 1993, "Interfacial Phenomena in Polymer-Electrolyte Cells: Lithium Passivation and Cycleability," *Journal of Power Sources*, 43(1-3), pp. 9-19.

[129] Yuan, M., Erdman, J., Tang, C. and Ardebili, H., 2014, "High Performance Solid Polymer Electrolyte with Graphene Oxide Nanosheets," *RSC Advances*, 4, pp. 59637-59642.

[130] Yang, X. Q., Lee, H. S., Hanson, L., McBreen, J, and Okamoto, Y, 1995, "Development of a New Plasticizer for Poly(Ethylene Oxide)-Based Polymer Electrolyte and the Investigation of Their Ion-Pair Dissociation Effect," *Journal of Power Sources*, 54(2), pp. 198-204.

[131] Kelly, I. E, Owen, J. R, and Steele, B. C. H, 1985, "Poly(Ethylene Oxide) Electrolytes for Operation at Near Room Temperature," *Journal of Power Sources*,

14(1-3), pp. 13-21.

[132] Kumar, Y., Hashmi, S. A., and Pandey, G. P., 2011, "Lithium Ion Transport and Ion-Polymer Interaction in PEO Based Polymer Electrolyte Plasticized with Ionic Liquid," *Solid State lonics*, 201(1), pp. 73-80.

[133] Fullerton-Shirey, S. K., and Maranas, J. K., 2010, "Structure and Mobility of PEO/LiC104 Solid Polymer Electrolytes Filled with A1203 Nanoparticles," *Journal of Physical Chemistry C*, 114(20), pp. 9196-9206.

[134] D'Epifanio, A., Fiory, F. S., Licoccia, S., Traversa, E., Scrosati, B., and Croce, F., 2004, "Metallic-Lithium, Lifep04-Based Polymer Battery Using PEO-Zr02 Nanocomposite Polymer Electrolyte," *Journal of Applied Electrochemistry*, 34(4), pp. 403-408.

[135] Chung, S. H, Wang, Y., Persi, L, Croce, F, Greenbaum, S. G., Scrosati, B, and PIichta, E., 2001, "Enhancement of Ion Transport in Polymer Electrolytes by Addition of Nanoscale Inorganic Oxides," *Journal of Power Sources*, 97-8, pp. 644-648.

[136] Hu, M., Pang, X., and Zhou, Z., 2013, "Recent Progress in High-Voltage Lithium Ion Batteries," *Journal of Power Sources*, 237, pp. 229-242.

[137] Hautier, G., Jain, A., and Ong, S. P., 2012, "From the Computer to the Laboratory: Materials Discovery and Design Using First-Principles Calculations," *Journal of Materials Science*, 47(21), pp. 7317-7340.

[138] Plimpton, S, 1995, "Fast Parallel Algorithms for Short-Range Molecular Dynamics," *Journal of Computational Physics*, 117(1), pp. 1-19.

[139] Aider, B. J., and Wainwright, T. E., 1957, "Phase Transition for a Hard Sphere

System," *Journal of Chemical Physics*, 27(5), pp. 1208-1209.

[140] Kresse, G, and Hafher, J., 1993, "Ab Initio Molecular Dynamics for Liquid Metals," *Physical Review B*, 47(1), pp. 558-561.

[141] Isralewitz, B., Gao, M., and Schulten, K., 2001, "Steered Molecular Dynamics and Mechanical Functions of Proteins," *Current Opinion in Structural Biology*, 11(2), pp. 224-230.

[142] Takeuchi, H, Roe, R. J, and Mark, J. E, 1990, "Molecular Dynamics Simulation of Diffusion of Small Molecules in Polymers. II. Effect of Free Volume Distribution," *Journal of Chemical Physics*, 93(12), pp. 9042-9048.

[143] Racko, D., Capponi, S., Alvarez, F., Colmenero, J., and Bartos, J., 2009, "The Free Volume Structure of a Polymer Melt, Poly(Vinyl Methylether) from Molecular Dynamics Simulations and Cavity Analysis," *Journal of Chemical Physics*, 131(6).

[144] Chang, K.-S, Chung, Y.-C, Yang, T.-H, Lue, S. J, Tung, K.-L., and Lin, Y.-F, 2012, "Free Volume and Alcohol Transport Properties of PDMS Membranes: Insights of Nano-Structure and Interfacial Affinity from Molecular Modeling," *Journal of Membrane Science*, 417, pp. 119-130.

[145] Uddin, N. M., Capaldi, F. M., and Farouk, B., 2011, "Molecular Dynamics Simulations of the Interactions and Dispersion of Carbon Nanotubes in Polyethylene Oxide/Water Systems," *Polymer*, 52(2), pp. 288-296.

[146] Cho, J., and Sun, C. T., 2007, "A Molecular Dynamics Simulation Study of Inclusion Size Effect on Polymeric Nanocomposites," *Computational Materials Science*, 41(1), pp. 54-62.

[147] Smith, J. S., Bedrov, D., and Smith, G. D., 2003, "A Molecular Dynamics

Simulation Study of Nanoparticle Interactions in a Model Polymer-Nanoparticle Composite," *Composites Science and Technology*, 63(11), pp. 1599-1605.

[148] Brown, D, Mele, P, Marceau, S, and Alberola, N. D, 2003, "A Molecular Dynamics Study of a Model Nanoparticle Embedded in a Polymer Matrix," *Macromolecules*, 36(4), pp. 1395-1406.

[149] Starr, F. W, Schroder, T. B, and Glotzer, S. C, 2002, "Molecular Dynamics Simulation of a Polymer Melt with a Nanoscopic Particle," *Macromolecules*, 35(11), pp. 4481-4492.

[150] Hong, B., and Panagiotopoulos, A. Z., 2012, "Molecular Dynamics Simulations of Silica Nanoparticles Grafted with Poly(ethylene oxide) Oligomer Chains," *Journal of Physical Chemistry B*, 116(8), pp. 2385-2395.

[151] Liu, J., Gao, Y., Cao, D., Zhang, L., and Guo, Z., 2011, "Nanoparticle Dispersion and Aggregation in Polymer Nanocomposites: Insights from Molecular Dynamics Simulation," *Langmuir*, 27(12), pp. 7926-7933.

[152] Borodin, 0., Smith, G. D., Bandyopadhyaya, R., and Byutner, E., 2003, "Molecular Dynamics Study of the Influence of Solid Interfaces on Poly(Ethylene Oxide) Structure and Dynamics," *Macromolecules*, 36(20), pp. 7873-7883.

[153] Kuppa, V., and Manias, E., 2003, "Dynamics of Poly(Ethylene Oxide) in Nanoscale Confinements: A Computer Simulations Perspective," *Journal of Chemical Physics*, 118(7), pp. 3421-3429.

[154] Hackett, E., Manias, E., and Giannelis, E. P., 2000, "Computer Simulation Studies of PEO/Layer Silicate Nanocomposites," *Chemistry of Materials*, 12(8), pp. 2161-2167.

[155] Neyertz, S, Brown, D, and Thomas, J. O, 1995, "Molecular Dynamics Simulation of the Crystalline Phase of Poly(Ethylene Oxide)-Sodium Iodide, PEO 3nai," *Electrochimica Acta*, 40(13-14), pp. 2063-2069.

[156] Kasemagi, H., Klintenberg, M., Aabloo, A., and Thomas, J. O., 2001, "Molecular Dynamics Simulation of the Effect of Adding an Al2O3 Nanoparticle to PEO-Licvlibr/Li Systems," *Journal of Materials Chemistry*, 11(12), pp.3191-3196.

[157] Liivat, A., Brandell, D., and Thomas, J. O., 2007, "A Molecular Dynamics Study of Ion-Conduction Mechanisms in Crystalline Low-M-W Lipf6 Center Dot PE06," *Journal of Materials Chemistry*, 17(37), pp. 3938-3946.

[158] 180. Brandell, D., Liivat, A., Kasemagi, H., Aabloo, A., and Thomas, J. O., 2005, "Molecular Dynamics Simulation of the LiPF6 Center Dot PEO6 Structure," *Journal of Materials Chemistry*, 15(14), pp. 1422-1428.

[159] Borodin, O., and Smith, G. D, 2000, "Molecular Dynamics Simulation Study of Li-Doped Diglyme and Poly(Ethylene Oxide) Solutions," *Journal of Physical Chemistry B*, 104(33), pp. 8017-8022.

[160] Un, B., Boinske, P. T, and Halley, J. W., 1996, "A Molecular Dynamics Model of the Amorphous Regions of Polyethylene Oxide," *Journal of Chemical Physics*, 105(4), pp. 1668-1681.

[161] Ferreira, B. A., Muller-Plathe, F., Bemardes, A. T, and De Almeida, W. B, 2002, “A Comparison of Li+ Transport in Dimethoxyethane, Poly(Ethylene Oxide) and Poly(Tetramethylene Oxide) by Molecular Dynamics Simulations," *Solid State lonics*, 147(3-4), pp. 361-366.

[162] Karo, J., and Brandell, D., 2009, "A Molecular Dynamics Study of the Influence

of Side-Chain Length and Spacing on Lithium Mobility in Non-Crystalline LiPF6 Center Dot Peox; X=10 And 30," *Solid State lonics*, 180(23-25), pp. 1272-1284.

[163] Borodin, O., Smith, G. D., Bandyopadhyaya, R., Redfem, P., and Curtiss, L. A., 2004, "Molecular Dynamics Study of Nanocomposite Polymer Electrolyte Based on Poly(Ethylene Oxide)/Libf4," *Modeling and Simulation in Materials Science and Engineering*, 12(3), pp. S73-S89.

[164] Kasemagi, H., Aabloo, A., Klintenberg, M. K., and Thomas, J. 0., 2004, "Molecular Dynamics Simulation of the Effect of Nanoparticle Fillers on Ion Motion in a Polymer Host," *Solid State lonics*, 168(3-4), pp. 249-254.

[165] Boulet, P., Covency, P. V., and Stackhouse, S., 2004, "Simulation of Hydrated Li+, Na+- And K+-Montmorillonite/Polymer Nanocomposites Using Large-Scale Molecular Dynamics," *Chemical Physics Letters*, 389(4-6), pp.261-267.

[166] Kasemagi, H, Klintenberg, M, Aabloo, A., and Thomas, J. O., 2003, "Molecular Dynamics Simulation of Temperature and Concentration Dependence of the 'Filler' Effect for the Licvpeo/A1203-Nanoparticle System," *Electrochimica Acta*, 48(14-16), pp. 2273-2278.

[167] Ennari, J., Neelov, I., and Sundholm, F., 2000, "Molecular Dynamics Simulation of the Structure of PEO Based Solid Polymer Electrolytes," *Polymer*, 41(11), pp. 4057-4063.

[168] Ennari, J., Pietila, L. O., Virkkunen, V., and Sundholm, F., 2002, "Molecular Dynamics Simulation of the Structure of an Ion-Conducting PEO-Based Solid Polymer Electrolyte," *Polymer*, 43(20), pp. 5427-5438.

[169] Costa, D, Munao, G, Saija, F, and Caccamo, C, 2007, "Reference Interaction Site

Model and Molecular Dynamics Study of Structure and Thermodynamics of Methanol," *Journal of Chemical Physics*, 127(22).

[170] Humphrey, W., Dalke, A., and Schulten, K., 1996, "VMD: Visual Molecular Dynamics," *Journal of Molecular Graphics & Modelling*, 14(1), pp. 33-38.

[171] Zhao, K. Pharr, M., Cai, S., Vlassak, J. J., and Suo., Z., 2011, "Large Plastic Deformation I High-Capacity Lithium-Ion Batteries Caused by Charge and Discharge," *Journal of the American Ceramic Society*, 94(S1), pp. S226-S235.

[172] Park. M., Zhang, X., Chung, M., Less, G. B., and Sastry, A. M., 2010, "A Review of Conduction Phenomena in Li-Ion Batteries," *Journal of Power Sources*, 195(24), pp. 7904-7929.

[173] Zhang, C., Santhanagopalan, S., Sprague, M. A., and Pesaran, A. A., 2015, "A Representative-Sandwich Model for Simultaneously Coupled Mechanical-Electrical-Thermal Simulation of a Lithium-Ion Cell under Quasi-Static Indentation Tests," *Journal of Power Sources*, 298, pp. 309-321.

[174] Baker, D. R., Verbrugge, M. W., and Bower, A. F., 2016, "Thermodynamics, Stress, and Stefan-Maxwell Diffusion in Solids: Application to Small-Strain Materials Used in Commercial Lithium-Ion Batteries," *Journal of Solid State Electrochemistry*, 20, pp. 163-181.

[175] Purkayastha, R., and McMeeking, R. M., 2012, "A Linearized Model for Lithium Ion Batteries and Maps for Their Performance and Failure," *Journal of Applied Mechanics*, 79, pp. 1-16.

[176] Zhao, K., Pharr, M., Vlassak, J. J., and Suo, Z., 2010, "Fracture of Electrodes in Lithium-Ion Batteries Caused by Fast Charging," *Journal of Applied Physics*, 108.

[177] Siqueira, L. J. A., and Ribeiro, M. C. C, 2005, "Molecular Dynamics Simulation of the Polymer Electrolyte Poly(Ethylene Oxide)/Lic104. I. Structural Properties," *Journal of Chemical Physics*, 122(19).

[178] Siqueira, L. J. A, and Ribeiro, M. C. C, 2006, "Molecular Dynamics Simulation of the Polymer Electrolyte Poly(Ethylene Oxide)/Lic104. II. Dynamical Properties," *Journal of Chemical Physics*, 125(21).

[179] Laasonen, K, and Klein, M. L, 1995, "Molecular Dynamics Simulations of the Structure and Ion Diffusion in Poly(Ethylene Oxide)," *Journal of the Chemical Society-Faraday Transactions*, 91(16), pp. 2633-2638.

[180] Aabloo, A., and Thomas, J., 2001, "Molecular Dynamics Simulation of Lithium Ion Mobility in a PEO Surface," *Solid State lonics*, 143(1), pp. 83-87.

[181] Forsyth, M., Payne, V. A., Ratner, M. A., Deleeuw, S. W., and Shriver, D. F., 1992, "Molecular Dynamics Simulations of Highly Concentrated Salt Solutions: Structural and Transport Effects in Polymer Electrolytes," *Solid State lonics*, 53, pp. 1011-1026.

[182] Costa, L. T., and Ribeiro, M. C. C., 2006, "Molecular Dynamics Simulation of Polymer Electrolytes Based on Poly(Ethylene Oxide) and Ionic Liquids. I. Structural Properties," *Journal of Chemical Physics*, 124(18).

[183] Borodin, O., and Smith, G. D., 2009, "Quantum Chemistry and Molecular Dynamics Simulation Study of Dimethyl Carbonate: Ethylene Carbonate Electrolytes Doped with LiPF6," *Journal of Physical Chemistry B*, 113(6), pp. 1763-1776.

[184] Carter, E. A., “Challenges in Modeling Materials Properties without Experimental Input,” *Science*, 321(5890), pp. 800-803.

[185] Liu, L., and Li, X., 2016, "A Continuum Theory for Electro-Elastic-Diffusive Systems with Applications," In Progress.

[186] Alternative Rules for Construction of High Pressure Vessels (2013). Boiler and Pressure Vessel Code. American Society of Mechanical Engineers, ASME Section VIII Division 3-2013.

[187] Ohno, N., and Wang, J. D., 1993, "Kinematic Hardening Rules with Critical State of Dynamic Recovery, Part I: Formulation and Basic Features for Ratcheting Behavior," *International Journal of Plasticity*, 9(3), pp. 375-390.

[188] Soler, A. I., 1980, "Analysis of Bolted Joints with Nonlinear Gasket Behavior," *Journal of Pressure Vessel Technology*, 102(3), pp. 249-256.

[189] Van Staden, R. C., Guan, H., & Loo, Y. C., 2006, "Application of the Finite Element Method in Dental Implant Research," *Computer Methods in Biomechanics and Biomedical Engineering*, 9(4), pp. 257-270.

[190] Joshi, M. G., Advani, S. G., Miller, F., & Santare, M. H., 2000, "Analysis of a Femoral Hip Prosthesis Designed to Reduce Stress Shielding," *Journal of Biomechanics*, 33(12), pp. 1655-1662.

[191] Katsousnas, A. T., 1989, "Temperature Derating of API Flanges under Combination of Loading," PRAC 89-21, Report prepared for American Petroleum Institute.

[192] Helwig, P., Faust, G., Hindenlang, U., Hirschmuller, A., Konstantinidis, L., Bahrs, C., Sudkamp, N., & Schneider, R., 2009, "Finite Element Analysis of Four Different Implants Inserted in Different Positions to Stabilize an Idealized Trochanteric Femoral Fracture," *Injury*, 40 (3), pp. 285-295.

[193] Abid, M., 2006, "Determination of Safe Operating Conditions for Gasketed Flange Joints under Combined Internal Pressure and Temperature: A Finite Element Approach," *International Journal of Pressure Vessels and Piping*, 83 (6), pp. 433–441.

[194] Abid, M., and Ullah, B., 2007, "Three-Dimensional Nonlinear Finite Element of Gasketed Flange Joint under Combined Internal Pressure and Variable Temperatures," *Journal of Engineering Mechanics*, 113(2), pp. 222–229.

[195] Abid, M., Khan, K. A., and Chattha, J. A., 2008, "Performance of a Flange Joint Using Different Gaskets under Combined Internal Pressure and Thermal Loading, A FEM Approach," *Mechanics Based Design of Structures and Machines*, 36, pp. 212–223.

[196] Bouzid, A. H., and Derenne, M., 2001, "Analytical Modeling of the Contact Stress with Nonlinear Gaskets," *Journal of Pressure Vessel Technology*, 124(1), pp. 47-53.

[197] Bouzid, A. H., and Champliaud, H., 2004, "Contact Stress Evaluation of Nonlinear Gaskets Using Dual Kriging Interpolation," *Journal of Pressure Vessel Technology*, 126(4), pp. 445-450.

[198] Folwer, J. R., and Walker, K. C., 1987, "Capabilities of API Flanges under Combinations of Loading," PRAC 86-21, Report prepared for American Petroleum Institute.

[199] Fowler, J. R., 1994, "Sealability of API R, RX, & BX Ring Gaskets," PRAC 90-21, Report prepared for American Petroleum Institute.

[200] Ghoneim, G. A., and Haverty, K. H., 1990, "Capabilities of API Integral Flanges under Combinations of Loading," PRAC 88-21, Report prepared for American Petroleum Institute.

[201] Kellogg, M. W., 1956, Design of Piping Systems.

[202] Kondo, K., Sato, K., Sawa, T., Tsubaki, S., and Omiya, Y., 2013, "Sealing Performance Evaluation in Bolted Flange Connections with Ring Joint Gasket Subjected to Internal Pressure," ASME 2013 Pressure Vessels and Piping Conference, 2.

[203] Koves, W. J., 1996, "Analysis of Flange Joints under External Loads," *Journal of Pressure Vessel Technology*, 118(1), pp. 59-63.

[204] Krishna, M. M., Shunmugam, M. S., and Prasad, N. S., 2007, "A Study on the Sealing Performance of Bolted Flange Joints with Gaskets Using Finite Element Analysis," *International Journal of Pressure Vessels and Piping*, 84(6), pp. 349–357.

[205] Kumano, H., Sawa T. and Hirose, H., 1994, "Mechanical Behavior of Bolted Joint under Steady Heat Conduction," *Journal of Pressure Vessel Technology*, 116(1), pp. 42–48.

[206] Lumsden, S., and Black, I., 2010, "American Petroleum Institute Welding Neck Flange Design for Subsea Pipelines," *Proceedings of the Institution of Mechanical Engineers, Part E: Journal of Process Mechanical Engineering*, 224(1), pp. 23-33.

[207] Mackerle, J., 2003, "Finite Element Analysis of Fastening and Joining: A Bibliography (1990 - 2002)," *International Journal of Pressure Vessels and Piping*, 80, pp. 253–271.

[208] Pacheco, R. M. I., Riagussoff, I. T., Donato, V. P. G., and Largura, C. J. L., 2011, "Failure Analysis on Flanges Caused by Loss or Damage in Holsters," *Revista Materia*, 16(4), pp. 877-886.

[209] Prasad, N. S., and Mathan, G., 2008, "A Study on the Sealing Performance of Flange Joints with Gaskets under External Bending Using Finite-Element Analysis," *Journal of Process Mechanical Engineering*, 222(1), pp. 22-29.

[210] Sawa, T., Higurashi, N., and Akagawa, H., 1991, "A Stress Analysis of Pipe Flange Connections," *Journal of Pressure Vessel Technology*, 113(4), pp. 497-503.

[211] Sawa, T., Ogata, N., and Nishida, T., 2002, "Stress Analysis and Determination of Bolt Preload in Pipe Flange Connections with Gaskets under Internal Pressure," *Journal of Pressure Vessel Technology*, 124, pp. 385-396.

[212] Sawa, T., and Maezaki, W., 2004, "Thermal Stress Analysis and Sealing Performance Evaluation of Pipe Flange Connections with Spiral Wound Gaskets under Elevated Temperature," ASME/JSME Pressure Vessels and Piping Conference, pp. 61-66.

[213] Shah, V. N., 2008, "Uncertainty of Preloads in Closure Bolts for Transportation Casks for Hazardous and Radioactive Materials," ASME 2008 Pressure Vessels and Piping Conference, 7, pp. 215-223.

[214] "Technical Report on Temperature Derating of API Flanges under Combination of Loading," 1998, American Petroleum Institute, API 6AF1.

[215] Gere, J. M., 2004, "Stresses in Beams," Mechanics of Materials, 6, pp. 350-535.

[216] Lee, K., 2002, "Large Deflections of Canteliver Beams of Non Linear Elastic Material under a Combined Loading," *International Journal of Non-Linear Mechanics*, 37, pp. 439–443.

[217] Noor, A. K., and Burton, W. S., 1990, "Assessment of Computational Models for Multilayered Composite Shells," *Applied Mechanics Review*, 43, pp. 68-97.

[218] Hsueh, C. H., Lee, S., and Chuang, T. J., 2003, "An Alternative Method of Solving Multilayer Bending Problems," *Journal of Applied Mechanics*, 70(1), p. 151.

[219] Conway, H. D., and Farnham, K. A., 1970, "Bending of a Finite Beam in Bonded and Unbonded Contact with an Elastic Foundation," *International Journal of Mechanical Sciences*, 12(11), pp. 997-1005.

[220] Jasem, M. H., 2012, "Study of the Effect of the Variation of Layer's Thickness on the Bending Characteristics of the Composite Beam," *Al-Qadisiya Journal For Engineering Sciences*, 5, pp. 354-366.

[221] Gladwell, G. M. L., 1976, "On Some Unbonded Contact Problems in Plane Elasticity Theory," *Journal of Applied Mechanics*, 43(2), pp. 263-267.

[222] Conway, H. D., Vogel, S. M., Farnham, K. A., and So, S., Normal, 1966, "Normal and Shearing Contact Stresses in Indented Strips and Slabs," *International Journal of Engineering Sciences*, 4(4), pp. 343-359.

[223] Gallagher, A. P., 1983, "Bending of a Free Beam on an Elastic Foundation," *Journal of Applied Mechanics*, 50, pp. 463-465.

[224] Li, H., and Dempsey, J. P., 1988, "Unbonded Contact of Finite Timoshenko Beam on Elastic Layer," *Journal of Engineering Mechanics*, 114(8), pp. 1265-1284.

[225] Belendez, T., Neipp, C., and Belendez, A., 2002, "Large and Small Deflections of a Cantilever Beam," *European Journal of Physics*, 23, pp. 371–379.

[226] Berg, S., Akturk, A., Kammoun, M., and Ardebili, H., 2016, "Flexible Batteries under Extreme Bending: Interfacial Contact Pressure and Conductance," to be submitted.

[227] Kammoun, M., Berg, S., and Ardebili, H., 2016, "Stretchable Spiral Thin-Film Battery Capable of Out-Of-Plane Deformation," *Journal of Power Sources*, 332, pp. 406–412.

[228] Shigley, J. E., and Mischke, C. R., 1989, Mechanical Engineering Design, 5.

[229] Pawlak, A., and Galeski, A., 2010, "Cavitation During Tensile Drawing of Annealed High Density Polyethylene Oxide," *Polymer*, 51(4), pp. 5771-5779.

[230] Hong, K., Rastogi, A., and Strobl, G., 2004, "A Model Treating Tensile Deformation of Semicrystalline Polymers: Quasi-Static Stress-Strain Relationship and Viscous Stress Determined for a Sample of Polyethylene," *Macromolecules*, 37, pp. 10165-10173.

[231] Drozdov, A. D., and Christiansen, J. D., 2003, "Model for the Viscoelastic and Viscoplastic Responses of Semicrystalline Polymers," *Journal of Applied Polymer Science*, 88, pp. 1438-1450.

[232] Fleck, N. A., Hutchinson, J. W., and Tvergaard, V., 1989, "Softening by Void Nucleation and Growth in Tension and Shear," *Journal of Mechanics and Physics of Solids*, 37(4), pp. 515-540.

[233] Drozdov, A. D., 2009, "Mullins' Effect in Semicrystalline Polymers," *International Journal of Solids and Structures*, 46, pp. 3336-3345.

[234] Drozdov, A. D., Klitkou, R., and Christiansen, J. D., 2013, "Multi-Cycle Deformation of Semicrystalline Polymers: Observations and Constitutive Modeling," *Mechanics Research Communications*, 48, pp. 70-75.

[235] Drozdov, A. D., Klitkou, R., and Christiansen, J. D., 2013, "Cyclic Viscoplasticity of Semicrystalline Polymers with Finite Deformations," *Mechanics Research Communications*, 56, pp. 53-64.

[236] Detrez, F., Cantournet, S., and Seguela, R., 2011, "Plasticity/Damage Coupling in Semi-Crystalline Polymers Prior to Yielding: Micromechanisms and Damage Law Identification," *Polymer*, 52, pp. 1998-2008.

[237] Drozdov, A. D., and Dusunceli, N., 2013, "Modeling of Multi-Cycle Deformation of Polymers with Various Deformation Programs," *Multidiscipline Modeling in Materials and Structures*, 9(1), pp. 4-22.

[238] Ward, I. M., and Sweeney, J., 2013, Mechanical Properties of Solid Polymers, 3.

[239] Pawlak, A., Galeski, A., and Rozanski, A., 2014, "Cavitation During Deformation of Semicrystalline Polymers," *Progress in Polymer Science*, 39, pp. 921-958.

[240] Corte, L., Beaume, F., and Liebler, L., 2005, "Crystalline Organization and Toughening: Example of Polyamide-12," *Polymer*, 46, pp. 2748-2757.

[241] Argon, A. S., Galeski, A., and Kazmierczak, T., 2005, "Rate Mechanisms of Plasticity in Semi-Crystalline Polyethylene," *Polymer*, 46(25), pp. 11798-11805.

[242] Sing, C., and Alexander-Katz, A., 2010, "Globule-Stretch Transitions of Collapsed Polymers in Elongational Flow Fields," *Macromolecules*, 43(7), pp. 3532-3541.

[243] Wu, H., Li, X., Wang, Y., Wu, J., Huang, T., and Wang, Y., 2011, "Fracture Behaviors of Isotactic Polypropylene/Poly(Ethylene Oxide) Blends: Effect of Annealing," *Materials Science and Engineering A*, 528, pp. 8013-8020.

[244] Hu., D., Yu, J., Wong, K., Bagchi, B., Rossky, P. J., and Barbara, P. F., 2000, "Collapse of Stiff Conjugated Polymers with Chemical Defects into Ordered, Cylindrical Conformations," *Nature*, 405, pp. 1030-1033.

[245] Gadjourova, Z., Andreev, Y. G., Tunstall, D. P., and Bruce, P. G., 2001, "Ionic Conductivity in Crystalline Polymer Electrolytes," *Nature*, 412, pp. 520-523.

[246] Golodnitsky, D., Livshits, E., Ulus, A., & Peled, E., 2002, "Highly Conductive, Oriented Polymer Electrolytes for Lithium Ion Batteries," *Polymers for Advanced Technologies*, 13, pp. 683-689.

[247] Golodnitsky, D., and Peled, E., 2000, "Stretching-Induced Conductivity Enhancement of Li-(PEO)-Polymer Electrolyte," *Electrochimica Acta*, 45, pp. 1431-1436.

[248] Golodnitsky, D., Livshits, E. U., Barkay, Z., Lapides, I., Peled, E., Chung, S., and Greenbaum, S., 2001, "Fast Ion Transport Phenomena in Oriented Semicrystalline Lii-(PEO)N-Based Polymer Electrolytes," *Journal of Physical Chemistry A*, 105(44), pp. 10098-10106.

[249] Golodnitsky, D., Livshits, E., Rosenberg, Y., Lapides, I., and Peled, E., 2002, "Stretching-Induced Changes in Ion-Polymer Interactions in Semicrystalline Li-P(EO)N Polymer Electrolytes," *Solid State Ionics*, 147, pp. 265-273.

[250] Golodnitsky, D., Livshits, E., Kovarsky, R., and Greenbaum, S., 2004, "New Generation of Ordered Polymer Electrolytes for Lithium Batteries," *Electrochemical and Solid-State Letters*, 7(11), A412-A415.

[251] Livshits, E., Kovarsky, R., Lavie, N., Hayashi, Y., Golodnitsky, D., and Peled, E., 2005, "New Insights into Structural and Electrochemical Properties of Anisotropic Polymer Electrolytes," *Electrochimica Acta*, 50, pp. 3805-3814.

[252] Gitelman, L., Israeli, M., Averbuch, A., Nathan, M., Schuss, Z., and Golodnitsky, D., 2007, "Modeling and Simulation of Li-Ion Conduction in Poly(Ethylene Oxide)," *Journal of Computational Physics*, 227, pp. 1162-1175.

[253] Gitelman, L., Israeli, M., Averbuch, A., Nathan, M., Schuss, Z., and Golodnitsky, D., 2008, "Polymer Geometry and Li+ Conduction in Poly(Ethylene Oxide)," *Journal of Computational Physics*, 227, pp. 8347-8447.

[254] Gitelman, L., Averbuch, A., Nathan, M., Schuss, Z., and Golodnitsky, D., 2010, "Stochastic Model of Lithium Ion Conduction in Poly(Ethylene Oxide)," *Journal of Applied Physics*, 107.

[255] Zhang, X., Shyy, W., and Sastry, A. M., 2007, "Numerical Simulation of Intercalation-Induced Stress in Li-Ion Battery Electrode Particles," *Journal of Electrochemical Society*, 154(10), pp. A910-A916.

[256] Bower, A. F., Guduru, P. R., and Sethuraman, V. A., 2011, "A Finite Strain Model of Stress, Diffusion, Plastic Flow, and Electrochemical Reactions in a Lithium-

Ion Half-Cell," *Journal of Mechanics and Physics of Solids*, 59, 804-828.

[257] Ferreria, J. A., Grassi, M., Gudino, E., and de Oliveira, P., (2015), "A New Look to Non-Fickian Diffusion," *Applied Mathematical Modeling*, 39, pp. 194-204.

[258] Sillamoni, I. J. C., and Iadart, M. I., 2015, "A Model Problem Concerning Ionic Transport in Microstructured Solid Electrolytes," *Continuum Mechanics and Thermodynamics*, 27(6), pp. 941-957.

[259] Berg, S., Kelly, T., and Ardebili, H., 2016, "Multiphysics Models for Predicting Ionic Conduction in Flexible and Stretchable Solid Polymer Electrolyte Lithium Ion Batteries under Mechanical Deformation," to be submitted.

Appendix A

A Case Study to Evaluate the Accuracy of Linear and Nonlinear Analytical Methods to Predict the Response of a Mechanical System

1. Introduction

The flange of interest in the numerical analysis is a 346 mm (13-5/8 in) 103 MPa (15 ksi) API 6BX integral flange. All dimensions that define the geometry of the gasket, the flange body, the blind flange, and the nuts and bolts are defined by API codes [214]. The flange neck was extended to a distance of $2.5(Rt)^{1/2}$ from the hub in order to remove local loading effects from the vicinity of the hub, where R is the mean radius of the wall section and t is the neck wall thickness. This distance was originally used and supported by industry documents [191, 214].

2. Numerical approach

2.1 Finite element geometry

In order to properly account for the asymmetry associated with global bending of the flange hub, a 3-D half section finite element model was used, shown in Figure 56. The nuts and bolts were modeled as continuous components without thread profiles, individually modeled as cylindrical studs of diameter equal to the minimum thread root diameter, and heavy hex nuts modeled cylindrically with diameter equal

to the largest hexagonal distance on either end. This is shown in Figure 57. All finite element analysis was performed using Abaqus v. 6.12 (Simulia/Dassault Systems).

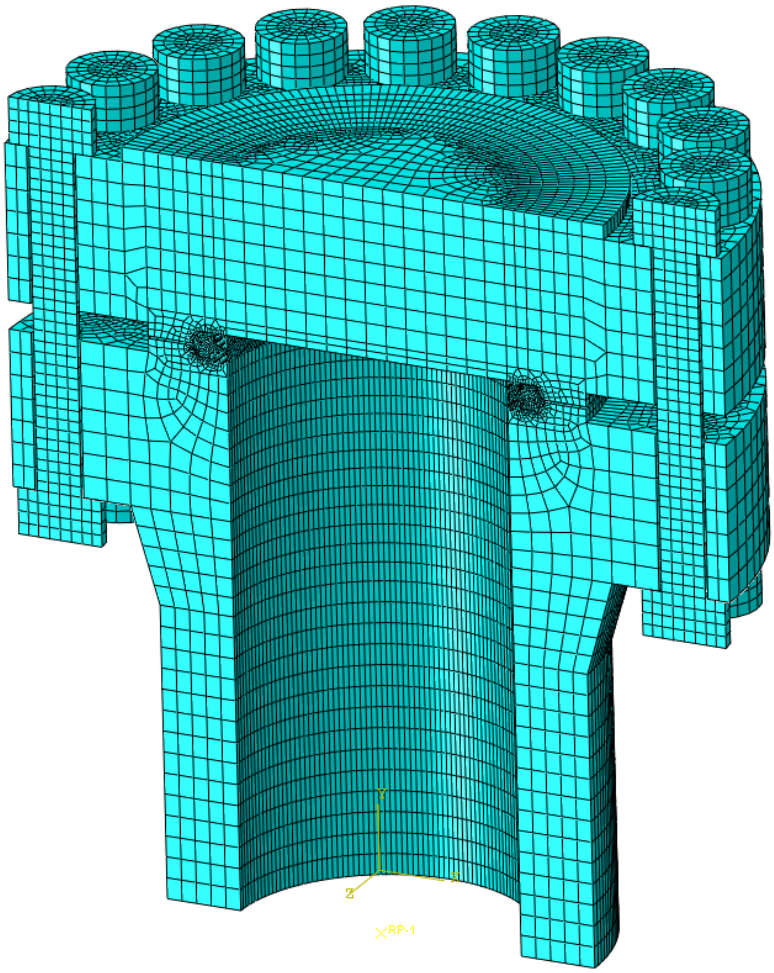

Figure 56: Half section 3-D finite element model of 346 mm (13-5/8 in) 103 MPa (15 ksi) integral flange hub.

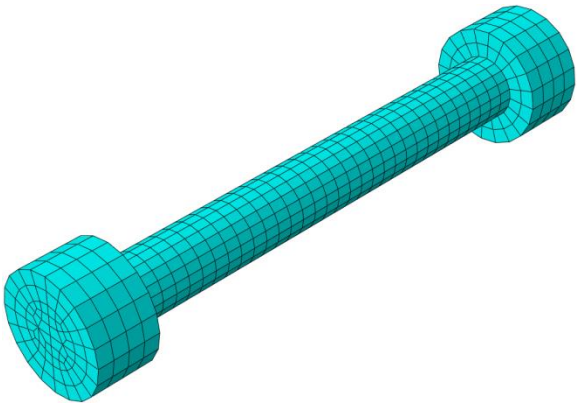

Figure 57: Continuous 3-D model of 57 mm (2-1/4 in) nut/bolt.

2.2 Component material properties

The mechanical and thermal material properties in the finite element model were taken from the original report by Katsousnas upon which API 6AF is based [191] in order to make a more direct comparison between the proposed methodology herein and the API 6AF methodology. Plasticity was only considered in the gasket and not the body or bolts since the criteria used for determining critical stress in these structural components is that the stress should be less than or equal to the yield of the assumed structural material [214]. Therefore, no significant plastic deformation is expected to occur, and the core material behavior can be approximated as elastic. The gasket was assumed to be SS316 since it is a common material used for metallic BX gaskets. The true stress vs. plastic strain curves at ambient temperature, and for temperatures at 176.67 ˚C (350 ˚F) and 343.33 ˚C (650 ˚F) were generated using methods in ASME BPVC to account for strain hardening by calculating parameters that relate plastic strain to yield stress, modulus, and accepted parameters based on material chemistry [186].

2.3 Static analysis

The element type used in the structural analysis was C3D8I elements since these include additional shape functions that allow improved numerical accuracy in cases of component bending. A blind flange was substituted for an adjacent flange body in order to account for the end loading associated with internal pressure. The flange hub symmetry plane was selected such that bolts on the tension and compression side of bending were in the cut plane. In addition to symmetry boundary conditions applied to the cut plane, the bottom surface of the blind flange face was constrained from axial movement with a boundary condition constraining the axial degree of freedom. At the other end of the flange in the neck region, a reference point with axial and rotational degrees of freedom coupled to the bottom surface of the flange was created. This was for the purpose of applying the axial mechanical loads associated with the pressure end load and external tension, and additionally for application of the global bending moment. Figure 58 illustrates the reference point coupling constraint.

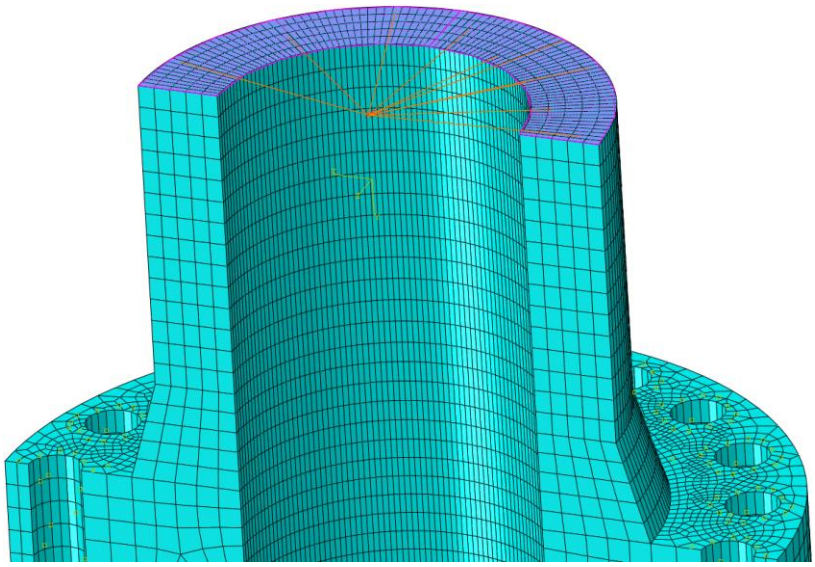

Figure 58: Reference point and surface constraint in FE model.

The first effect of static loading in the connection was that due to bolt makeup. The length of the bolts was adjusted to properly simulate the tightening associated with the makeup procedure. The reaction forces in each bolt were measured until the specified tension associated with half of yield for that prescribed bolt size was reached [214]. After the bolt makeup step, the temperature field was applied and the model was allowed to react to the thermal strains and reach an equilibrium state. After the equilibrium state was reached in the system, following application of the temperature field the internal pressure and corresponding pressure end load were applied. The internal pressure was applied to all wetted surfaces extending out to the OD of the gasket, shown in Figure 59. Three values of internal pressure were applied under combined loading: 0 MPa, 34 MPa, and 103 MPa (0 ksi, 5 ksi, and 15 ksi). Two values of external tension were applied following the internal pressure: 0 kN and 2224 kN (0 kips and 500 kips), which would equivalently be 4448 kN (1,000

kips) for a full section model. The final step was applying a large coupled bending moment equal to 40.67×10^6 N-m (30 million ft-lbf), a large bending moment thought to far exceed the limitations of the flange connection. The flange component stress and gasket contact pressure were monitored until the limitations were reached.

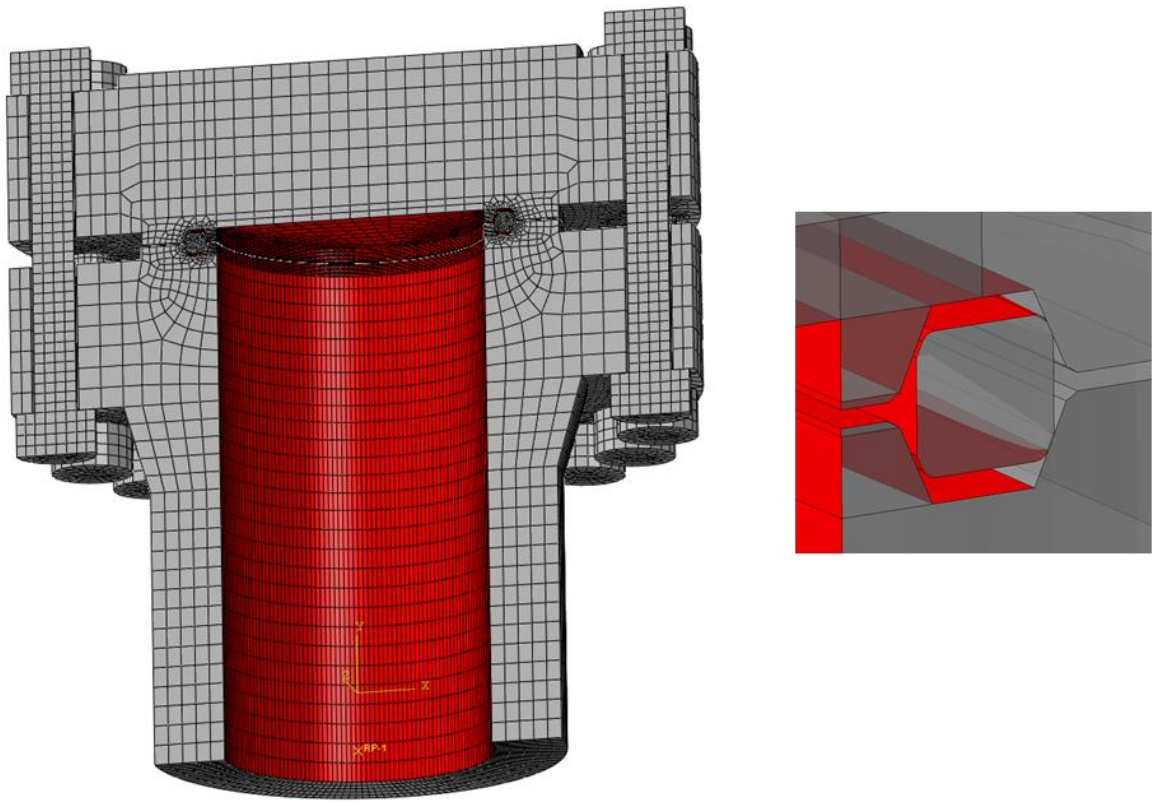

Figure 59: Applied internal pressure boundaries in FE model.

2.4 Thermal analysis

The element type selected for the heat transfer analysis was the DC3D8 element, which is a 3-D, 8 node heat transfer element with a single degree of freedom uncoupled from displacement which is suitable for calculating temperature fields. Flange component thermal interactions were modeled to account for gap

conductance. That is, the heat transfer through the medium between adjacent spaced components was included. This was of particular interest in modeling the heat transfer between the bolt studs and holes. Furthermore when firm contact is established heat transfer was modeled assuming negligible contact resistance. The original method by Katsousnas considers working fluid temperatures of 176.67 ˚C (350 ˚F) and 343.33 ˚C (650 ˚F) [191]. The inner bore was prescribed at these temperatures at all wetted surfaces, which assumes a shut-in condition with still fluid that has heated the inner surfaces to the bore fluid temperature at a steady state condition. The external exposed surfaces were modeled to simulate convection heat transfer. The heat transfer coefficients used on crosswind surfaces, and the bulk external temperature of 0 ˚C (32 ˚F) have been previously prescribed and are used in this analysis [191]. These values are based on extreme conditions of freezing rain and winds exceeding 80.5 km/h (50 mph), which is a severe service condition. The cross flow condition is illustrated in Figure 60. A steady state heat transfer analysis was carried out, and the thermal gradients are shown in Figure 61 and Figure 62.

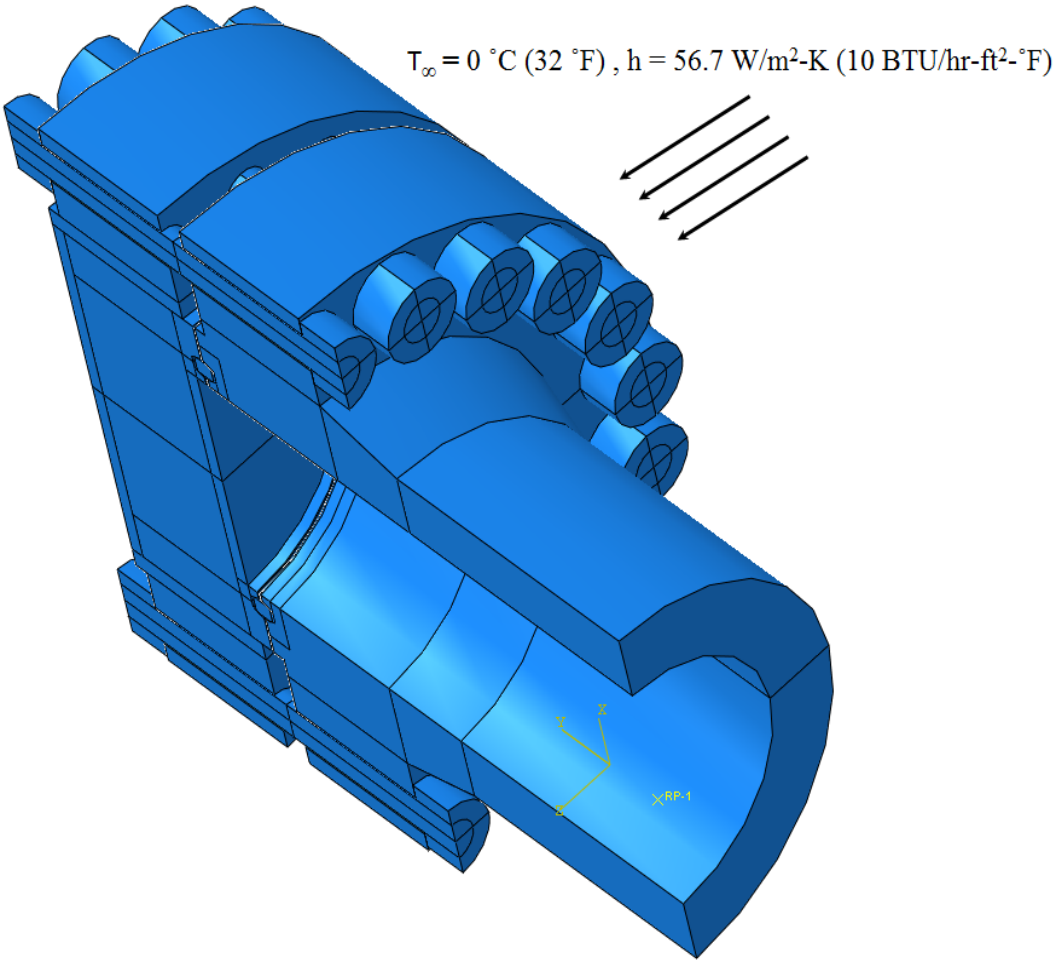

Figure 60: External cross flow boundary condition.

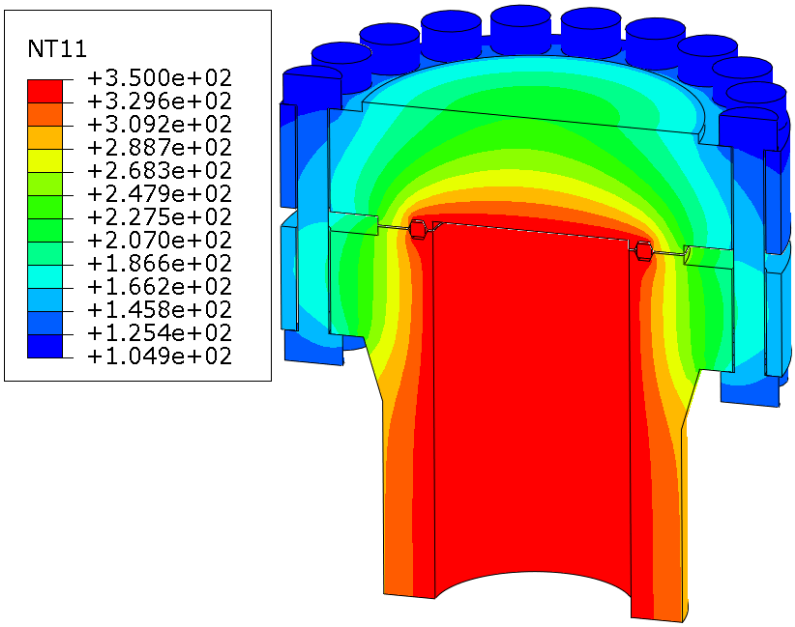

Figure 61: Temperature distribution in flange hub with 176.67 ˚C (350 ˚F) working fluid in bore.

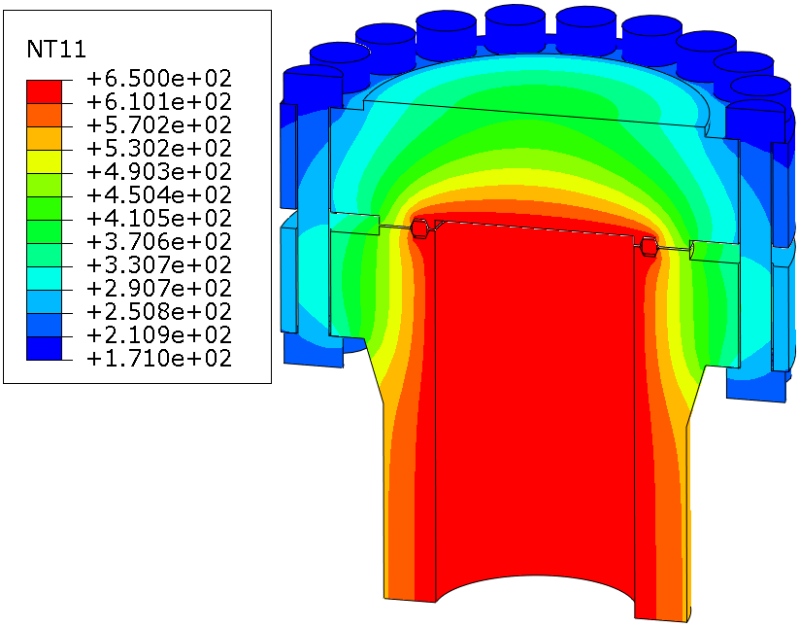

Figure 62: Temperature distribution in flange hub with 343.33 ˚C (650 ˚F) working fluid in bore.

3. Stress capacity results

3.1 Body and bolt stress

The flange component stresses were evaluated to determine the load limitations. Stress classification lines were established at high stress regions within the model, and primary and secondary stresses were obtained and assessed using the ASME methodology [186]. Additionally the bolt reaction forces were measured during the load cycle and compared with allowable stress levels [214]. The bolt stresses were found to exceed allowable stress far in advance of the flange primary and secondary stresses, which indicates that the flange connection load capacity is limited by the bolts.

3.2 Bolt stress limitations

A check was completed to verify the limitations in bolt stress associated with either stud tension (tensile failure) or thread shear stress (stripping). This was to verify the modeling of the bolts without thread profiles. For the bolt size used in the model, a combination of hand calculations with comparisons to code allowable stresses was completed using the following:

$$\boldsymbol{F_T = 0.83\sigma_y \frac{\pi}{4} D_{minor}{}^2} \text{ and} \tag{133}$$

$$\boldsymbol{F_S = 0.25\sigma_y \pi n L_e D_{nut}} \left[\boldsymbol{\frac{1}{2n} + \frac{D_{pitch} - D_{nut}}{\sqrt{3}}}\right], \tag{134}$$

where F_T is the allowable tensile load in the stud, F_S is the allowable stripping load for the threads, σ_y is the bolt yield strength 724 MPa (105ksi), D_{minor}, D_{nut}, and D_{pitch} are the thread root, minor nut contact diameter and pitch diameter of threads, respectively, L_e is the length of engagement, and n is the thread pitch. Dimensions for thread stress calculations were taken from standard values for UNC threads, which are standard for this type of bolt and nut. Taking the ratio of F_S to F_T by combining both equations and plugging in the appropriate values for the thread geometry produces a ratio of approximately 1.4, indicating the stud tensile strength limitation will be reached far in advance of thread stripping.

3.3 Bolt reaction force

The bolt reaction forces were monitored throughout the entire static analysis. Figure 63 is a plot of the average bolt load reaction forces with the application of the loads in each load step, with time 0-1 second being the bolt makeup, and time 1-2 seconds being the application of the temperature field. The comparison is that of the thermal gradient, and the flange hub under uniform temperature where the internal and external temperatures are equal (if the flange were placed in an oven). The results show that the thermal gradient causes the bolt reaction forces to increase. This is due to the differential expansion that occurs along the thermal gradient, which causes residual compression in the higher temperature regions and induces tension in the lower temperature regions and therefore an increase in bolt tension occurs. This effect is confirmed when it is compared to a condition where the temperature is the same everywhere, and no significant change in the bolt reactions

occurs. In this case the bolts are free to expand with the other components in the system.

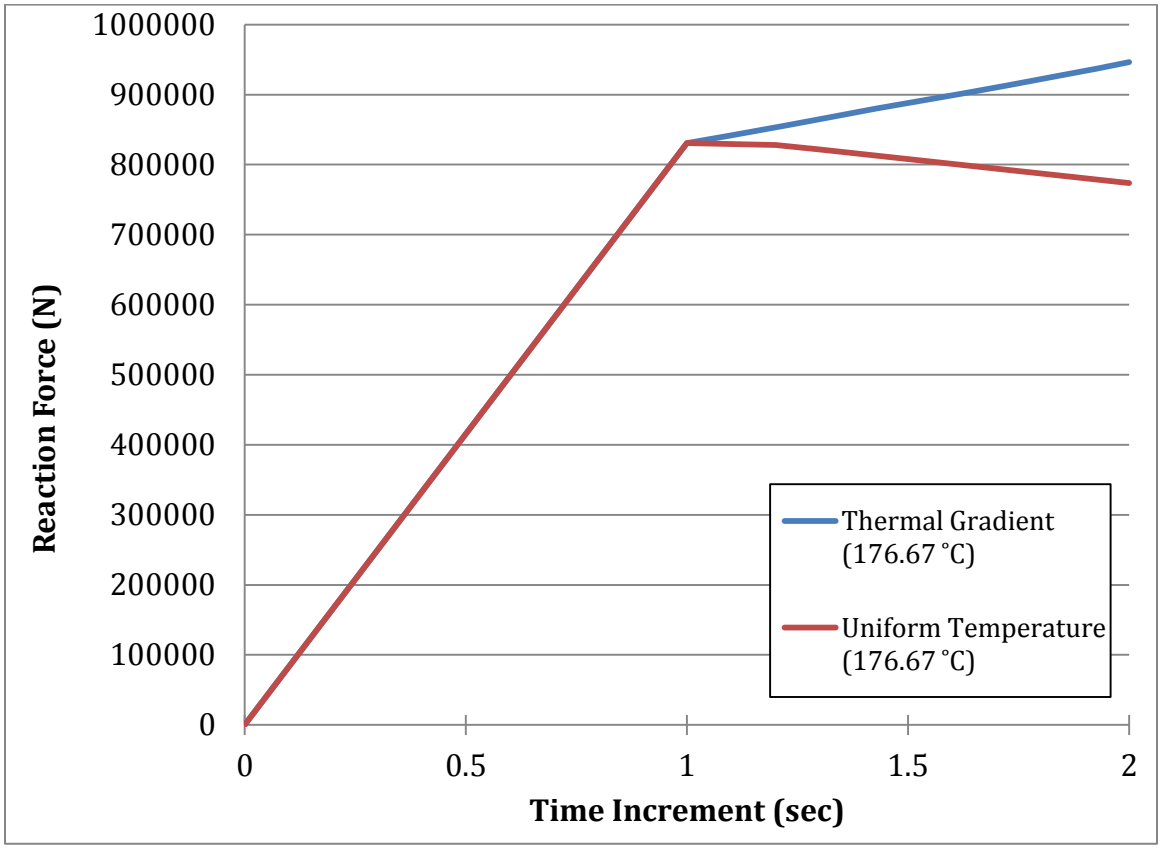

Figure 63: Average bolt reaction (full bolts) during the bolt makeup and temperature field application load steps.

3.4 Bolt material derating

The original analysis by Katsousnas makes the assumption that the bolt yield strength should be derated based on the bore temperature, and the calculated flange capacities are based on this assumption [191]. The thermal analysis, which produces a conservative thermal gradient based on operating conditions, indicates that the bolt temperatures do not exceed 121.11 ˚C (250 ˚F) for either a 176.67 ˚C

(350 ˚F) or 343.33 ˚C (650 ˚F) fluid temperature, which is the temperature threshold at which the material yield should be derated [186]. The bending capacity based on bolt reaction force was calculated for two thermal cases at 103 MPa (15 ksi) internal pressure: assuming a uniform temperature distribution at 176.67 ˚C (350 ˚F) or 343.33 ˚C (650 ˚F), and assuming the large thermal gradient at both temperatures, respectively. This was to compare the effects of the additional bolt loading from the thermal gradient to the derating of bolt strength, since to include both effects to determine bending capacity, as previously done, is overly conservative. In the case of uniform temperature distribution, the bolt material yield was derated for the purposes of determining bending capacity, with derating factors taken from API for low carbon and low alloy steels [214]. In the case of a thermal gradient, where bolts do not exceed 121.11 ˚C (250 ˚F), no derating factor was considered in determining flange capacity. The flange capacities for the two cases are compared in Table 4. Because the thermal gradient produces large additional tension in the bolts, it exceeds the effect of material yield derating due to a more uniform temperature distribution.

Table 4: Bending capacity comparison based on uniform temperature distribution (derated bolt strength) and thermal gradient (non-derated bolt strength).

Temperature (˚C)	Bolt Bending Capacity (N-m)
176.67 - Gradient	2,490,861
176.67 - Uniform	3,046,730
343.33 - Gradient	642,338
343.33 - Uniform	1,818,746

3.5 Stress comparison to API 6AF

The flange bending capacity based on bolt stress was calculated and plotted as a function of internal pressure and external tension, and these values were compared to API 6AF values [214]. This comparison of flange capacities for 176.67 ˚C (350 ˚F) or 343.33 ˚C (650 ˚F) is plotted and shown in Figure 64 and Figure 65, respectively. It is important to note that based on the thermal analysis, and on the study described in Sections 3.3-3.4, the bolt yield strength was not derated. The plots of capacity indicate a linear trend, which follows the trend of the original data obtained by Katsousnas as expected [191]. The removal of bolt yield derating factors accounts for the shift in the lines to higher predicted bending capacities. The change in the slope is due to the inclusion of contact sliding interactions of the flange hub, and a change in hub contact stiffness due to pressure. Since in the original analysis by Katsousnas the bolts were tied to the flange face, and since linear superposition was used, the nonlinear kinematic response associated with bolt/flange face sliding, and frictional contact resistance to the application of bending was not present.

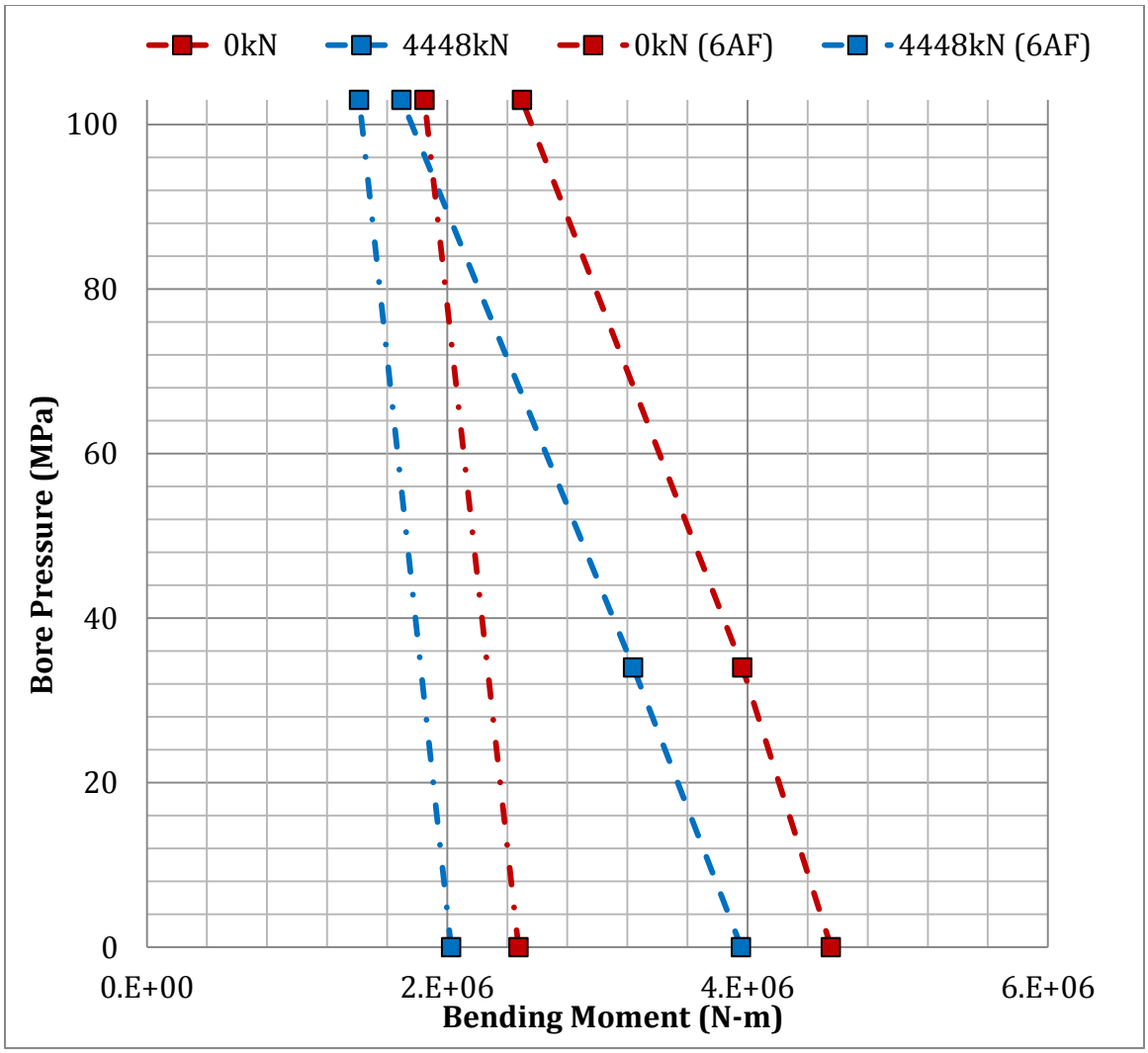

Figure 64: Bending capacity of 346 mm (13-5/8 in) 103 MPa (15 ksi) flange based on stress criteria and bore temperature of a) 176.67 ˚C (350 ˚F) and b) 343.33 ˚C (650 ˚F) with comparison to 6AF.

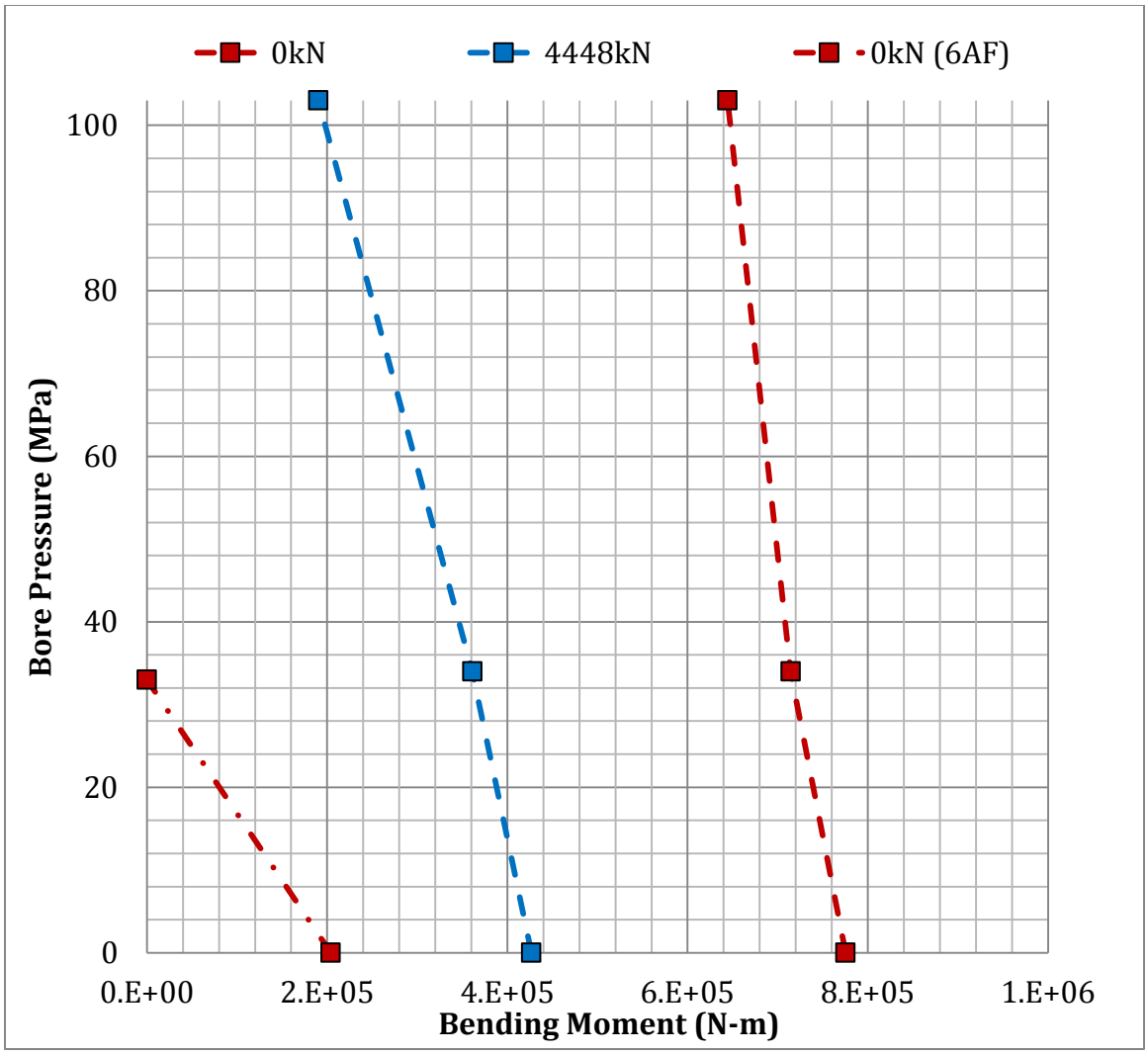

Figure 65: Bending capacity of 346 mm (13-5/8 in) 103 MPa (15 ksi) flange based on stress criteria and bore temperature of a) 176.67 ˚C (350 ˚F) and b) 343.33 ˚C (650 ˚F) with comparison to 6AF.

4. Leakage capacity results

4.1 Leak and gasket contact pressure

The nodal contact pressure around the circumference of the gasket in the contact bands was measured during the application of the static loading. Leak

criteria differed from the original analysis by Katsousnas because the seal contact pressure was evaluated rather than the flange face reaction force [191]. Figure 66 shows an example of a path definition in the region of the contact bands on the OD of the gasket. Leak is predicted to occur when contact pressures in all defined paths in either the upper or lower contact bands drop below the prescribed pressure criteria of 3x working pressure at any given angle around the circumference of the gasket. This method of using contact pressure can account for the changing nature of contact between the gasket and groove, and the plastic response of the gasket as bending increases. An example illustrating how contact pressure leak was determined is shown in Figure 67, where P1-P7 are circumferential paths going around the gasket OD regions of the upper contact band.

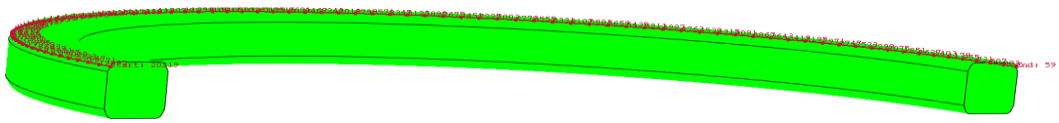

Figure 66: Path definition example around gasket circumference (upper contact band).

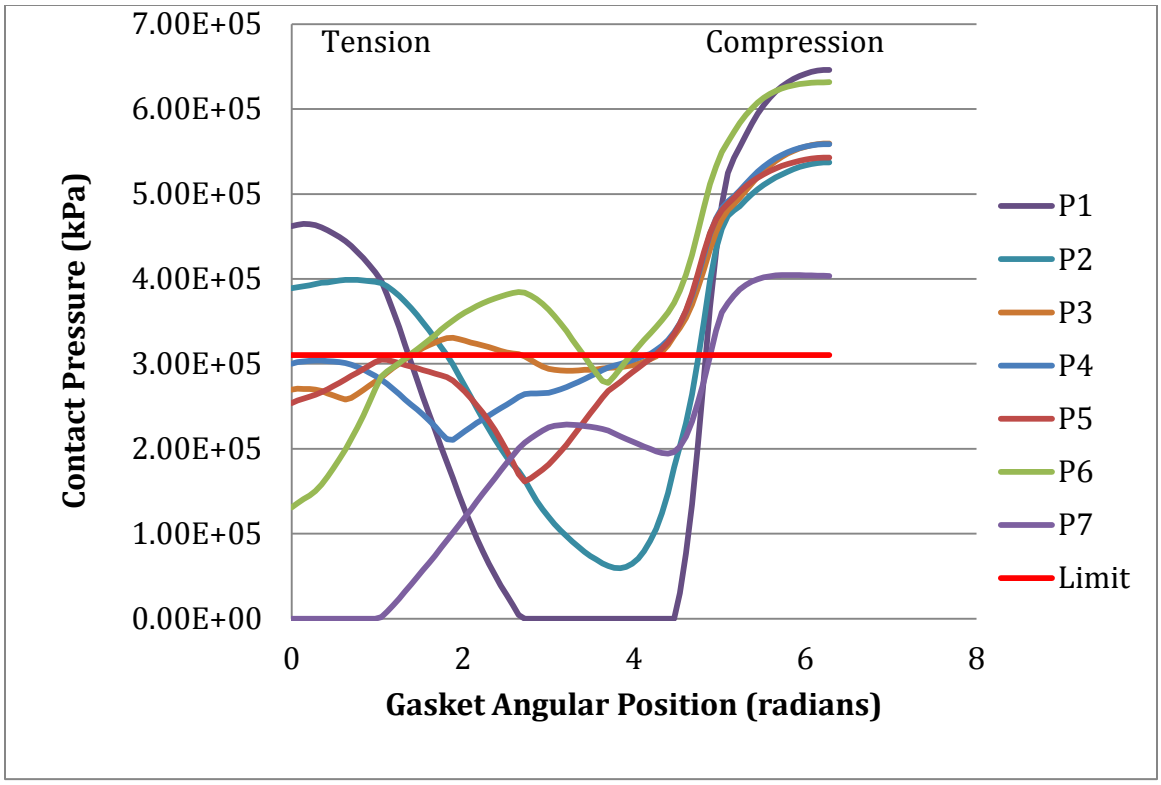

Figure 67: Upper band gasket contact region when leak occurs– circumferential gasket contact pressure (psi) vs. angular position (degrees).

4.2 Leak comparison to API 6AF

The flange bending capacity based on leak criteria was determined and plotted as a function of internal pressure and external tension, and these values were compared to API 6AF values [191, 214]. This comparison of flange capacities for 176.67 ˚C (350 ˚F) or 343.33 ˚C (650 ˚F) is plotted and shown in Figure 68 and Figure 69, respectively. The trends observed are a stark difference to the trends observed in API 6AF [214]. Figure 68 and Figure 69 show a nonlinear trend in the new data, that as pressure increases up to a point, the flange sealing capacity increases, and beyond a critical point, the flange sealing capacity decreases again.

According to the data the flange sealing capacity appears to be larger at 103MPa (15ksi) than at 0MPa internal pressure at 176.67 ˚C (350 ˚F), and smaller at 343.33 ˚C (650 ˚F). A theory for this observation has to do with the effect of the thermal gradient on the hub face contact pressure and its influence on seal integrity. Figures 70-72 show plots of the hub face contact pressure with a uniform temperature (free expansion), and with thermal gradients at 176.67 ˚C (350 ˚F) bore temperature and 343.33 ˚C (650 ˚F) bore temperature. These plots in Figure 70-72 illustrate how the hub face contact pressure changes as a result of thermal strains. Because of the gasket in the seal groove, with no thermal strains the hub face only contacts on the outer edge of the face as the blind flange bows out during clamping (Figure 70). When thermal strains associated with 176.67 ˚C (350 ˚F) are applied, the additional expansion causes increased contact pressure around the face edge, which influences seal integrity (Figure 71). Between 176.67 ˚C (350 ˚F) and 343.33 ˚C (650 ˚F) sufficient thermal expansion occurs near the flange bore to cause contact near that region and shift the contact pressure distribution, effectively reversing the direction of increasing contact pressure (Figure 72). This reversal influences seal integrity between 176.67 ˚C (350 ˚F) and 343.33 ˚C (650 ˚F) as the nature of the hub face contact pressure changes. The sealing capacity decreases as axial tension is increased from 0 kN to 4448 kN, which is expected since the hub separation force increases.

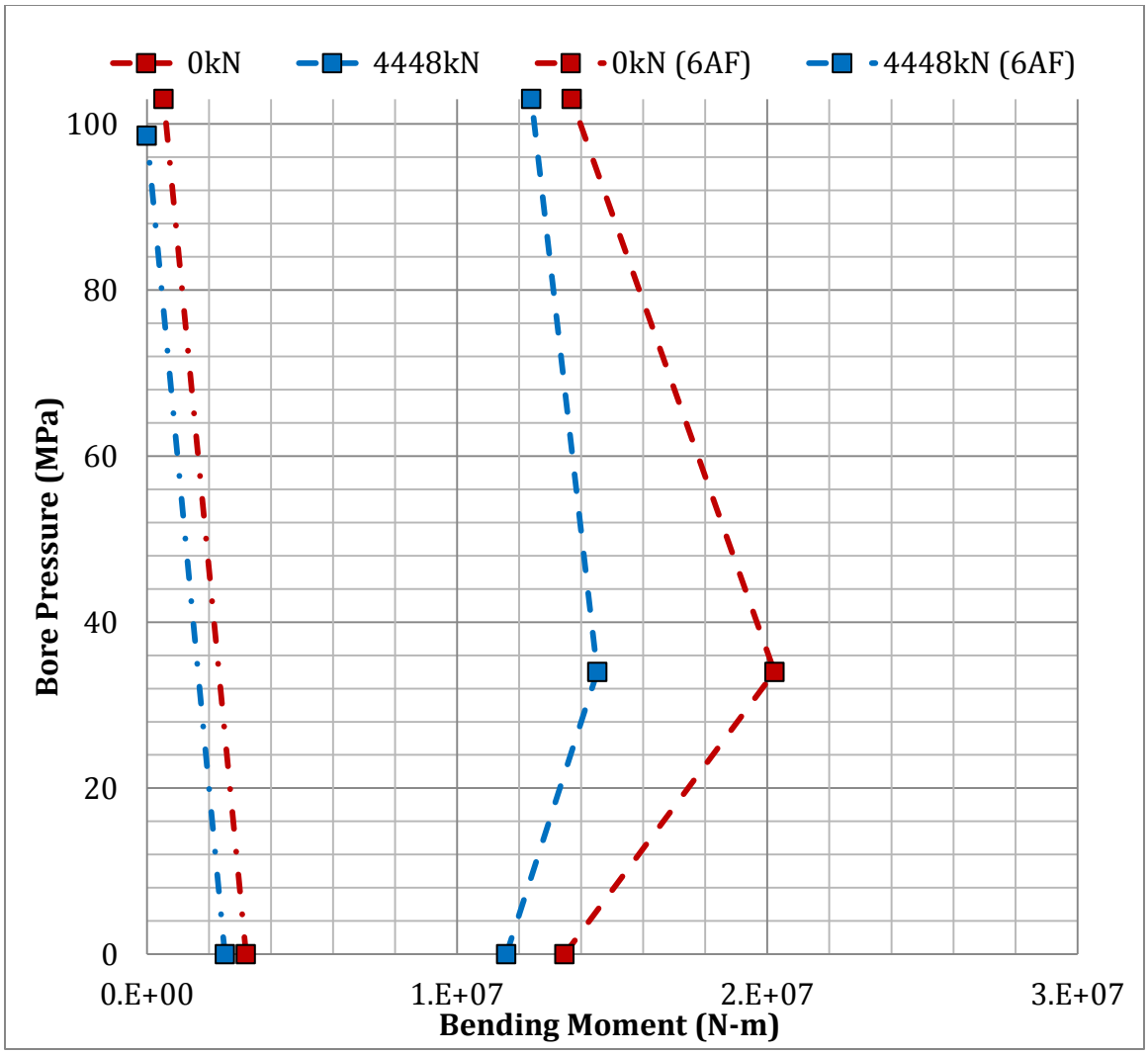

Figure 68: Bending capacity of 346 mm (13-5/8 in) 103 MPa (15 ksi) flange based on leak criteria and bore temperature of a) 176.67 ˚C (350 ˚F) and b) 343.33 ˚C (650 ˚F) with comparison to 6AF.

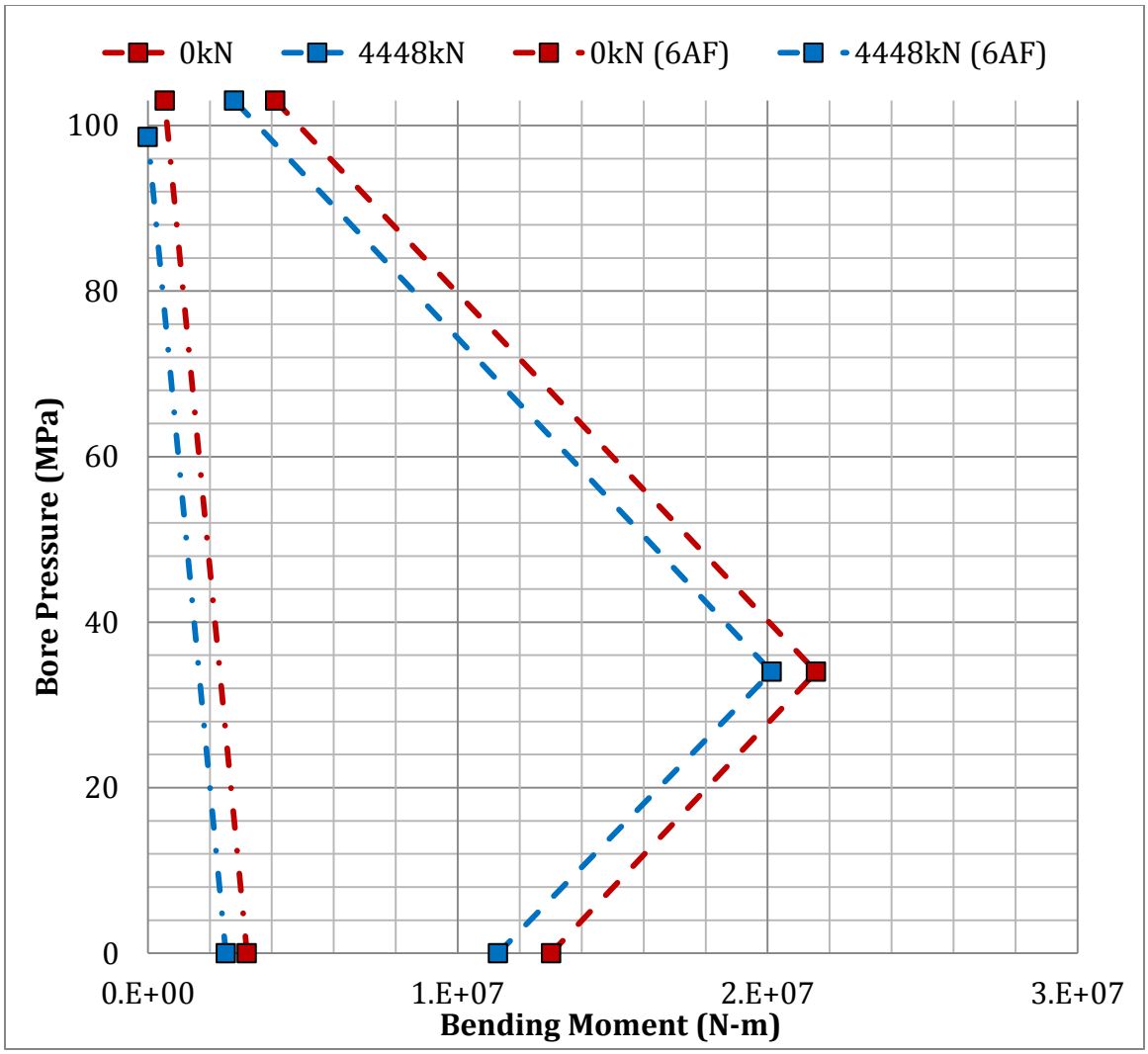

Figure 69: Bending capacity of 346 mm (13-5/8 in) 103 MPa (15 ksi) flange based on leak criteria and bore temperature of a) 176.67 ˚C (350 ˚F) and b) 343.33 ˚C (650 ˚F) with comparison to 6AF.

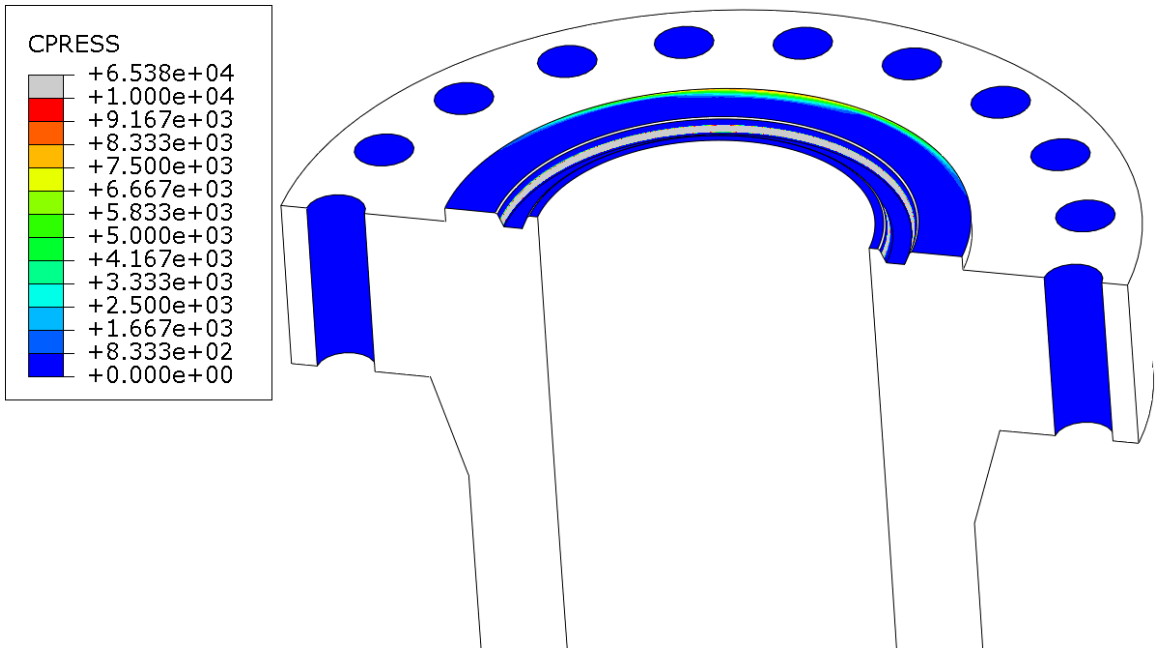

Figure 70: Hub face contact pressure with uniform temperature (no gradient).

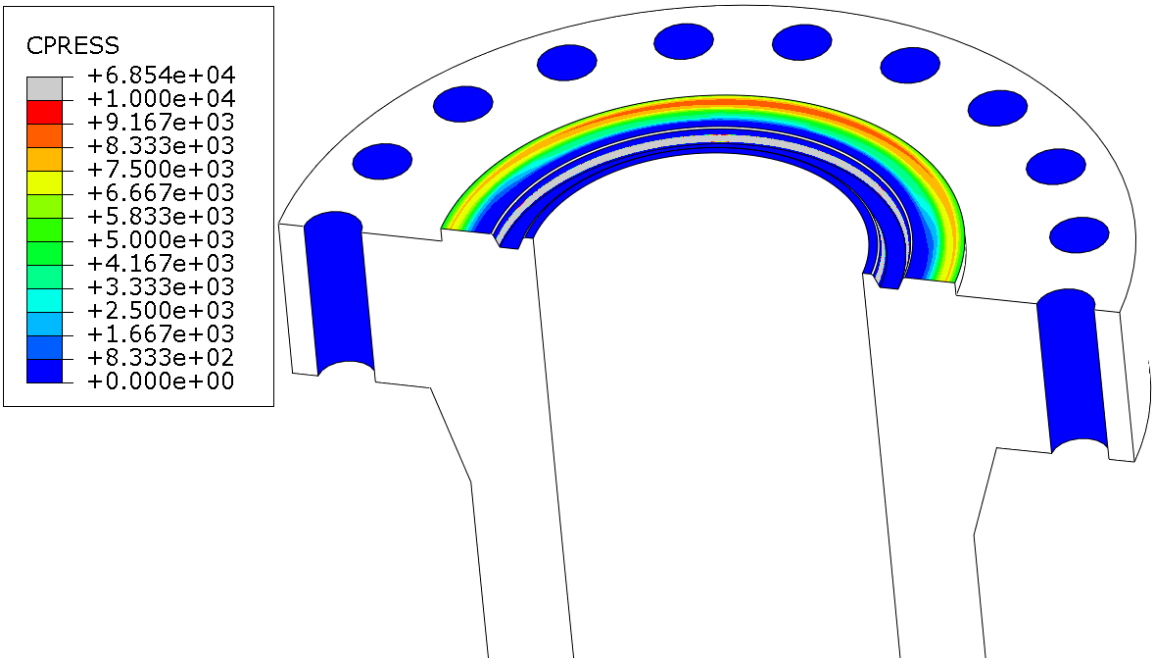

Figure 71: Hub face contact pressure with 176.67 ˚C (350 ˚F) working fluid in bore.

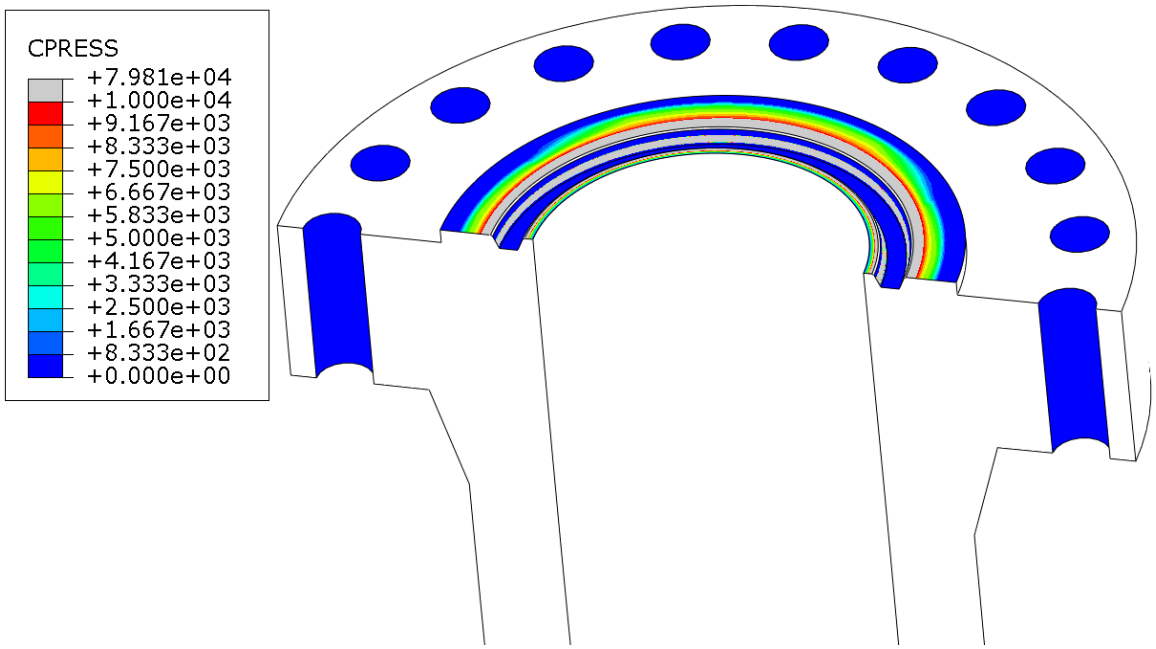

Figure 72: Hub face contact pressure with 343.33 ˚C (650 ˚F) working fluid in bore.

5. Conclusions

In taking the alternative nonlinear approach to determining flange capacities as presented in this study, the limitations of the linear methodology used by API 6AF and originally by Katsousnas is demonstrated. For the selected flange size, the stress limitation to load capacity is in the bolts, which is in agreement with 6AF. However, the original methodology takes into account the effects of loading due to the thermal gradient, and additionally derates the bolt strength to calculate load capacity. It has been demonstrated in this work that a conservative thermal gradient can produce additional thermal loading, while leaving the bolts in a cold temperature region. A uniform temperature distribution would not produce additional loading due to free expansion of the material, assuming the materials are not dissimilar. Therefore

including the bolt loading effects associated with the thermal gradient, and derating the bolt material, introduces unnecessary conservatism, and applying only the thermal gradient without derating the bolt strength is a realistic and accurate scenario.

Predicting leak in the hub connection is less direct, but greatly differs from API 6AF. A critical point is therefore predicted in the flange gasket sealing performance based on internal pressure, which is influenced by hub stiffness from the internal pressure. Additionally beyond the critical point the slope of the curve changes in comparing the 176.67 ˚C (350 ˚F) or 343.33 ˚C (650 ˚F) leak curves. This is likely due to thermal expansion and the change in hub contact pressure as bore temperature is increased, and this model was able to account for this nonlinear change in hub contact due to thermal expansion, which linear methods could not. By including material, geometric and contact nonlinearities into the solution, it has been shown that a more accurate and efficient solution can be obtained as a result. This work has demonstrated that linear numerical methods can fail to detect relative extrema that may exist within certain trends, and can even modify the slope of certain important trends.

Appendix B

Description of the Model Setup and Conditions Considered in the LIB Computational Model

1. Finite element strain model

As described in Chapter VI, Equations 85 and 105 were solved using numerical methods. The equations were solved using strain inputs taken from a finite element model to calculate strains that result from bending of the electrolyte. The nodal values of normal strain and shear strain were plotted and output for use in the numerical solution. The finite element structural models assumed a simply supported beam, with a uniformly distributed load applied to bend the electrolyte to various bending curvatures. The finite element model allowed for the calculation of strain using small deformations, and the inclusion of nonlinear geometry. Figures 73-78 show the values of normal and shear strain output from the nonlinear geometry model.

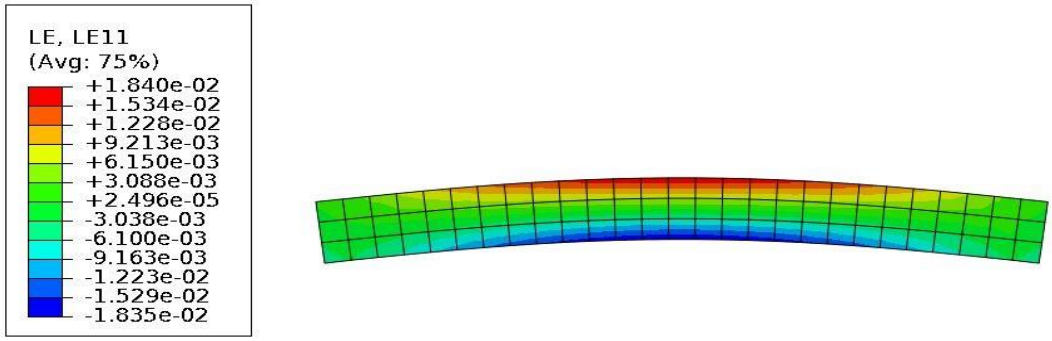

Figure 73: Finite element model strain, normal strain in horizontal direction (bending curvature radius of 10 mm).

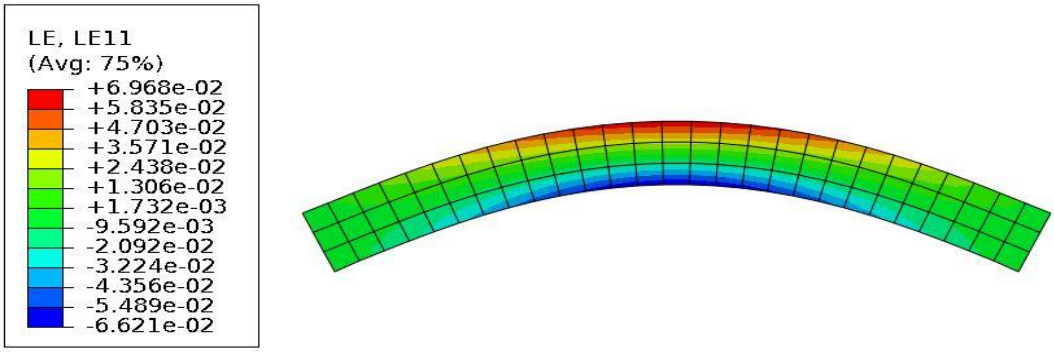

Figure 74: Finite element model strain, normal strain in horizontal direction (bending curvature radius of 2 mm).

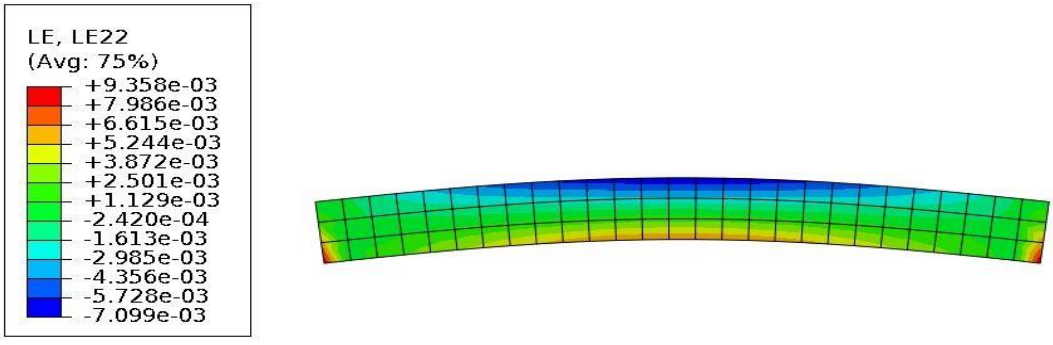

Figure 75: Finite element model strain, normal strain in vertical direction (bending curvature radius of 10 mm).

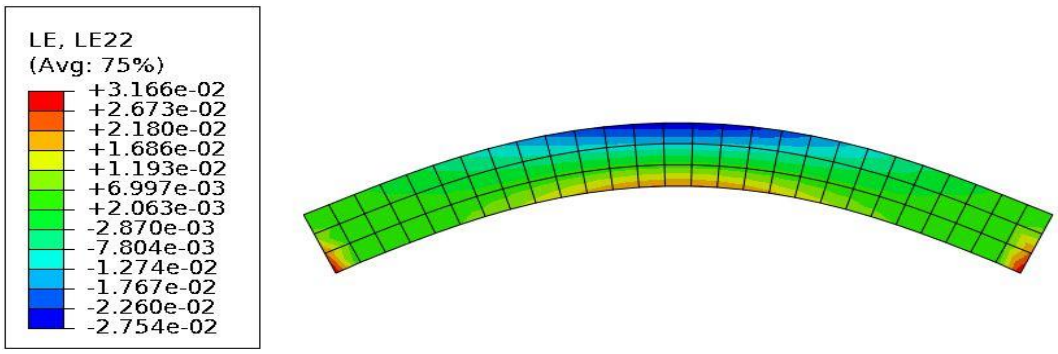

Figure 76: Finite element model strain, normal strain in vertical direction (bending curvature radius of 2 mm).

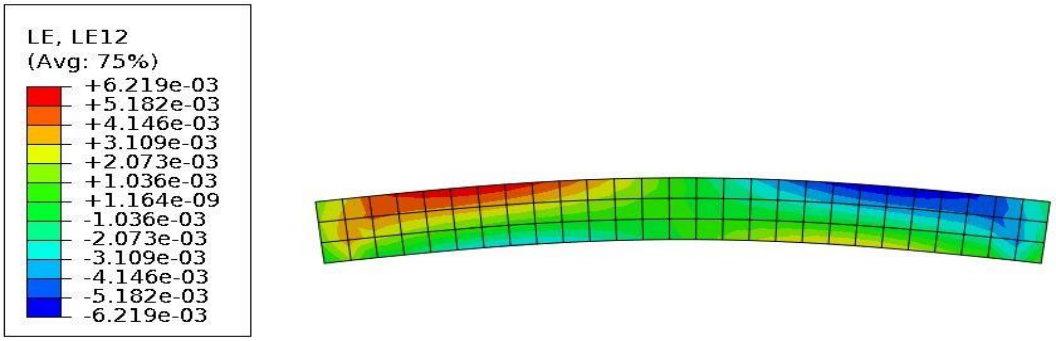

Figure 77: Finite element model strain, shear strain (bending curvature radius of 10 mm).

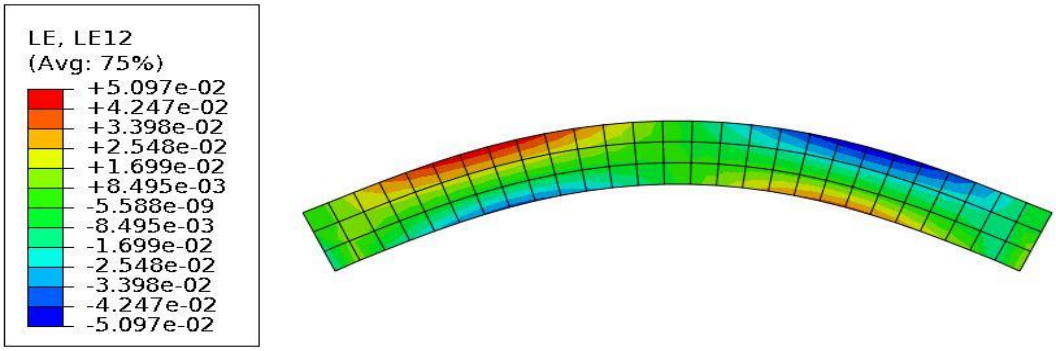

Figure 78: Finite element model strain, shear strain (bending curvature radius of 10 mm).

2. Numerical approach

The nodal strain data was extracted from the finite element model for the small and large deformation models. The concentration equations were discretized using the same nodal locations as that of the finite element model, as shown in Figure 79. The nodal locations were defined as (i,j) coordinates and enumerated and defined according to $0 \leq i \leq n$ and $0 \leq j \leq m$, where n=28 and m=4, given the size of the mesh. Each differential term for each node was calculated using a finite difference expression. The gradient was used to further transform Equations 85 and 105 for the numerical analysis, creating second order terms, which were accounted for in the finite difference solution. Boundary conditions for flux were defined at the electrolyte boundaries, as defined in Equations 129-132. A Gauss-Seidel scheme was used to iteratively solve for the equations, since the resulting discretization of Equations 85-105 resulted in an equation of the form

$$C_{i,j} = \left[\frac{C_{i+1,j}+C_{i-1,j}+C_{i,j+1}+C_{i,j-1}}{h^2} + \cdots\right]. \qquad (135)$$

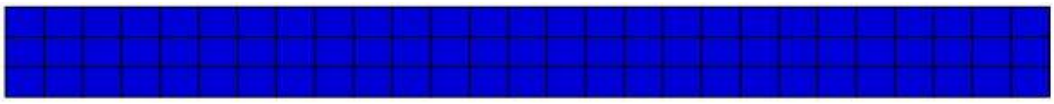

Figure 79: Nodal locations representing the electrolyte for the numerical analysis.